FACULDADE DE ENGENHARIA DA UNIVERSIDADE DO PORTO

Optimization of process parameters in the manufacturing of supports in L-PBF

Joana Xavier Viterbo

Dissertation submitted to Faculty of Engineering of the University of Porto for the degree of Masters in Mechanical Engineering

Supervisors: Prof. Dr. Abílio de Jesus, FEUP; Dr. Gonçalo Rodrigues, ADIRA

July 25, 2022

Optimization of process parameters in the manufacturing of supports in L-PBF

Joana Xavier Viterbo

Dissertation submitted to Faculty of Engineering of the University of Porto for the degree of Masters in Mechanical Engineering

Approved in oral examination by the committee:

Chair: Prof. Dr. Teresa Duarte
External Examiner: Prof. Dr. Hélder Puga
Supervisor: Prof. Dr. Abílio de Jesus

July 25, 2022

Abstract

Additive Manufacturing (AM) has been rapidly gaining relevance and popularity in various fields due to the new opportunities that these new processes entail. Some of the key strengths of these processes are more design freedom, material savings, cost reductions and smaller lead times. After the development of the concept of AM with polymeric materials, this potential has been expanded to metallic materials, which pose significantly different challenges to the control of the processes, which is achieved through a rigorous optimization of parameters.

A leading technology in metallic AM is laser powder bed fusion, due to its dimensional accuracy and achievable quality. As in all other AM processes, the parts are built layer after layer, which represents challenges when any volume of the geometry is not supported by previously solidified layers. There is a necessity to transfer heat and anchor parts uniformly to prevent undesired distortion and defects in the final product, that would compromise geometric accuracy and mechanical properties. However, this function cannot be assured by un-melted powder, resulting in the need for support structures in this manufacturing process.

The focus of this work is the optimization of process parameters to achieve efficient support structures. Firstly, a state of the art of the AM metallic processes is presented, as well as the positioning of laser powder bed fusion in the industry today and of the solutions that have been researched in an effort to improve support structures.

In the experimental part of this study, a new specimen concept was designed to evaluate the response variable, as a measurement of the performance of support structures with different scanning parameters and different geometric features. The specimens were manufactured in stainless steel 316 L and were studied in terms of strength, through tensile tests of the specimens, and relative density, with microscopic observations. Then, numeric simulations were conducted in order to quantitatively characterize the supports' performance.

Finally, it was concluded that the width of support teeth and the scanning speed were the most determining parameters and that the best support connectivity were achieved at the maximum energy density input. The numeric simulations provided a reference for comparison of the supports' performance and it was verified that the supports that fully anchored the parts and prevented distortion had a higher efficiency of connection

Keywords: Laser Powder Bed Fusion, Support structures, Process parameters, Mechanical Testing, Numerical Simulations

Resumo

O Fabrico Aditivo tem vindo a ganhar relevância e popularidade nas mais diversas áreas devido às novas oportunidades que possibilitam. Alguns dos pontos fortes deste tipo de fabrico incluem a liberdade geométrica, redução de custos, poupança de matéria prima, e redução de *lead time*. Após o desenvolvimento inicial do conceito de fabrico aditivo com materiais poliméricos, o potencial destas tecnologias foi expandido aos materiais metálicos, que acarretam desafios significativamente diferentes no controlo do processo, que se ultrapassam com uma rigorosa otimização dos parâmetros de processo.

Uma das tecnologias líder no Fabrico Aditivo de metais é o *Powder Bed Fusion* por laser, devido à precisão dimensional e qualidade possibilitadas. Tal como em todos os outros processos aditivos, as peças são construídas camada sobre camada, o que representa um desafio quando algum volume da geometria não é suportado por uma camada previamente solidificada. Existe a necessidade da transferência de calor uniforme de forma a evitar empenos e defeito no produto final que comprometeriam a precisão geométrica e propriedades mecânicas. No entanto, esta função não pode ser assegurada por pó metálico por fundir, levando à necessidade do fabrico de estruturas de suporte durante este processo.

O foco deste trabalho é a otimização dos parâmetros de processo para o fabrico de estruturas de suporte eficientes. Inicialmente, é apresentada uma revisão do estado da arte do fabrico metálico, bem como do posicionamente do *Powder Bed Fusion* no panorama industrial atual e da investigação desenvolvida na melhoria de suportes.

Na parte experimental deste estudo, foi desenhado um novo conceito de provete para avaliar a variável de resposta indicadora do desemprenho das estruturas de supporte fabricadas com diferentes parâmetros de processamento e diferentes geometrias. Estas foram estudadas relativamente à sua resistência, através de ensaios de tração e densidade relativa, a partir de observações microscópicas. Finalmente, foram desenvolvidas simulações numéricas de forma a caracterizar quantitativamente a eficácia dos suportes.

Finalmente, concluiu-se que os parâmetros mais determinantes são a largura dos dentes do suporte e a velocidade de processamento do laser, sendo que os melhores resultados de ligação entre o suporte e a peça foram alcançados através da máxima densidade energética. As simulações numéricas estabeleceram uma referência para avaliação do desempenho dos suportes e foi verificado que aqueles que conseguiram assegurar a fixação total da peça, evitando empenos, mostraram uma maior eficiência de ligação.

Keywords: *Laser Powder Bed Fusion*, Estruturas de suporte, Parâmetros do processo, Ensaios Mecânicos, Simulação Numérica

Acknowledgements

I would like to show my appreciation to all the people that supported me during this dissertation:

To everyone at ADIRA who welcomed me and trusted me with this project. Especially to Gonçalo for his continued guidance and trust. To João and Sérgio for all the support and encouragement over these four months.

To Professor Abílio de Jesus, for the tireless feedback and for the constant readiness to assist and guide the execution of this project in all the recurring meetings that I requested.

To Prof. Marco Parente for the help with the CAD process and numerical simulations. To Emilía Soares, Rui Silva, Domingos Carvalho and Miguel Figueiredo, for providing assistance in the design and testing of the specimens in such an expedite manner, making it possible for me to meet all my deadlines.

To Teresa for sharing the Mechanical Engineering journey with me since the very first day, five years ago. For being the most supportive and kind friend that anyone could ask for.

To my family for helping me through the moments of doubt and uncertainty throughout my academic life.

To my friends, whose support and positivity never wavered even when they felt the same doubt and uncertainty themselves.

To Ernesto, for everything.

Joana

Institutional Acknowledgements

I gratefully acknowledge the financial support from Portuguese Foundation for Science and Technology (FCT) under the projects ADDing (POCI-01-0145-FEDER-030490), Add.Strength (POCI-01-0145-FEDER-031307) and MAMTool (POCI-01-0145-FEDER-031895) by UE/FEDER through the programs COMPETE 2020.

Contents

1 Introduction **1**
- 1.1 Scope and motivation . . . 1
- 1.2 Objectives . . . 2
- 1.3 Layout . . . 2

2 Literature review **3**
- 2.1 Additive Manufacturing technologies . . . 3
- 2.2 Future Market Trends in Additive Manufacturing . . . 4
- 2.3 Metal Additive Manufacturing . . . 6
  - 2.3.1 Sinter-based Processes . . . 6
  - 2.3.2 Melting Processes . . . 11
  - 2.3.3 Processes Comparison . . . 14
- 2.4 State of the art of the LB-PBF process . . . 16
  - 2.4.1 Process Parameters . . . 18
  - 2.4.2 Materials and Powder Characteristics . . . 21
  - 2.4.3 Post Processing . . . 22
- 2.5 Support Structures in LPBF . . . 23
  - 2.5.1 Types of supports . . . 25
  - 2.5.2 Processing strategies . . . 29
  - 2.5.3 Numerical Simulation . . . 30

3 Experimental and Numerical details **33**
- 3.1 Machine characteristics and setup . . . 33
- 3.2 Materials . . . 35
- 3.3 Description of methods and experimental approach . . . 35
  - 3.3.1 Development of a new methodology and design of the test specimen . . . 35
  - 3.3.2 Design of Experiments - definition of factors and levels . . . 39
  - 3.3.3 Sample preparation and testing equipment . . . 49
  - 3.3.4 Numerical Simulation methodology . . . 52

4 Results and Discussion **55**
- 4.1 Results of supports' strength . . . 55
- 4.2 Results of relative density . . . 61
- 4.3 Discussion . . . 69
  - 4.3.1 Supports' strength . . . 69
  - 4.3.2 Connection efficiency . . . 76
  - 4.3.3 Relative density and its influence on support strength . . . 81
- 4.4 Final remarks and guidelines on the proposed method . . . 84

5 Conclusions and Future Work **85**
5.1 Conclusions 85
5.2 Further Work 86

References **89**

A SS316L technical data sheet **95**

B Parameters of the failed build job **97**

C Microscopic images of the 9 areas of the section of each density specimen **99**

D Stress-Strain curves obtained for each specimen, from the tensile tests **109**

E Microscopic pictures of the interface of the specimens before and after the tensile test **115**

List of Figures

Figure 2.1 AM trend indication of European Business by category (adapted from [3]) 4
Figure 2.2 AM trend indication of European Business, by category (adapted from [6]) 5
Figure 2.3 AM trend indication of European Business, by material (adapted from [6]) 5
Figure 2.4 CAGR in metal AM until 2026 6
Figure 2.5 Sinter-based and Melt-based technologies (adapted from [5]) 7
Figure 2.6 Schematics of some sinter-based technologies (adapted from [5]) 10
Figure 2.7 Powder Bed Fusion [17] 11
Figure 2.8 Direct Energy Deposition [19] 12
Figure 2.9 Resistance welding - Joule Printing (adapted from [21]) 13
Figure 2.10 Friction Deposition (adapted from [23]) 14
Figure 2.11 Liquid Metal Printing (adapted from [25]) 14
Figure 2.12 Maturity Index in 2020 for AM technologies (adapted from [5]) 15
Figure 2.13 Share of lasers per PBF Machine in 2021 and 2026 Forecast (adapted from [29]) 17
Figure 2.14 Schematics of AddCreator-AC210's Tiled Laser Melting solution 18
Figure 2.15 Real AddCreator-AC210 system 18
Figure 2.16 Schematic of main LPBF parameters (adapted from [40]) 20
Figure 2.17 Types of porosity found in LPBF parts (adapted from [34]) 21
Figure 2.18 Stresses induced by thermal gradients during PBF (adapted from [50]) . . 24
Figure 2.19 Examples of failed build jobs due to separation from supports and delamination 24
Figure 2.20 Typical support structures (adapted from [57, 58]) 26
Figure 2.21 Parameters of support teeth (adapted from [57, 59]) 27
Figure 2.22 Lattice support structure on cantilever beam (adapted from [52]) 27
Figure 2.23 Examples of Y, Inverted-Y and Tree supports (adapted from [52, 54]) . . . 28
Figure 2.24 Examples of contact-free heat supports (adapted from [63]) 29

Figure 3.1 Description of steps in the experimental procedure 36
Figure 3.2 Technical drawing of studs 38
Figure 3.3 Technical drawing of selected test specimen 39
Figure 3.4 Technical drawing of density specimens 45
Figure 3.7 Lifted edge of specimen 10 46
Figure 3.5 Damaged powder bed 46
Figure 3.6 Damaged recoater 46
Figure 3.8 Difference between lifted edges of the support specimens and the defect free density samples 47
Figure 3.9 Difference between density samples - worst quality achieved with 700 mm/s. 48
Figure 3.10 Final result of the successful build job 49

Figure 3.11 Specimen set-up and tensile testing machine 50
Figure 3.12 Optical microscope ZEISS Axiophot 51
Figure 3.13 Schematic of the density measurement procedure 51
Figure 3.14 Procedure to obtain FEM results 53

Figure 4.1 Residual plots for F_{rupt} considering the experimental value of Specimen 15 57
Figure 4.2 Visible detachment of specimen 15 57
Figure 4.3 Measured detachment of some of teeth in specimen 15 57
Figure 4.4 Pareto Chart for Maximum load, F_{rupt} 59
Figure 4.5 Main effects plots for maximum load, F_{rupt} 59
Figure 4.6 Factorial plot of interactions for F_{rupt} 60
Figure 4.7 Interaction plot for F_{rupt} 61
Figure 4.8 Best fraction of sample 37 (d_{rel}=92.47%) 62
Figure 4.9 Worst fraction of sample 37 (d_{rel}=85.13%) 62
Figure 4.10 Best fraction of sample 38 (d_{rel}=99.11%) 62
Figure 4.11 Worst fraction of sample 38 (d_{rel}=91.59%) 62
Figure 4.12 Best fraction of sample 39 (d_{rel}=99.59%) 63
Figure 4.13 Worst fraction of sample 39 (d_{rel}=91.62%) 63
Figure 4.14 Best fraction of sample 40 (d_{rel}=93.94%) 63
Figure 4.15 Worst fraction of sample 40 (d_{rel}=84.15%) 63
Figure 4.22 Best fraction of sample 45 (d_{rel}=99.97%) 63
Figure 4.23 Worst fraction of sample 45 (d_{rel}=95.45%) 63
Figure 4.16 Best fraction of sample 41 (d_{rel}=95.89%) 64
Figure 4.17 Worst fraction of sample 41 (d_{rel}=78.36%) 64
Figure 4.18 Best fraction of sample 42 (d_{rel}=99.97%) 64
Figure 4.19 Worst fraction of sample 42 (d_{rel}=95.56%) 64
Figure 4.20 Best fraction of sample 43 (d_{rel}=99.51%) 64
Figure 4.21 Worst fraction of sample 43 (d_{rel}=94.52%) 64
Figure 4.24 Pareto chart for relative density 66
Figure 4.25 Residuals chart for relative density 67
Figure 4.26 Main effects chart for relative density (v_S and P_L) 68
Figure 4.27 Interaction plot for density (with scan speed) 68
Figure 4.28 Interaction plot for density (with laser power) 68
Figure 4.29 Effect of energy density on maximum Load for all combinations of v_s and P_L, for the 4 types of supports 69
Figure 4.30 Stress strain curves of the 4 specimens manufactured at $v_s = 1150mm/s$ and $P_L = 300W$ 71
Figure 4.31 Representative example of support separation 71
Figure 4.32 Only two specimens in which fragments of the teeth (1-2mm) remained attached to the upper body - IDs 25 and 33 71
Figure 4.33 Interface of specimen 11 72
Figure 4.34 Darkest overhanging surfaces out of all the specimens 72
Figure 4.35 Layout of the specimens in the build platform, process head movement and powder distribution 73
Figure 4.36 Oxygen evolution leading up to the interface layer 74
Figure 4.37 Influence of scanning parameters on the resilience of support structures . . 76
Figure 4.38 Comparison between experimental, estimated and simulation values of rupture force of specimens with teeth top length of 150 μm (A and D) 77

Figure 4.39 Comparison between experimental, estimated and simulation values of rupture force of specimens with teeth top length of 400 μm (B and C) 77
Figure 4.40 Sensitivity analysis of specimen B 78
Figure 4.41 Ideal section of support grid (layer between the start teeth and the interface) 79
Figure 4.42 Imperfections of the real supports (Specimen 28) 79
Figure 4.43 Connection efficiency for each combination of scan speed and laser power (energy density) 80
Figure 4.44 Influence of scanning parameters on the connection efficiency 81
Figure 4.45 Examples of defects found on density specimens 82
Figure 4.46 Relative density resulting from each level of energy density 82
Figure 4.47 Experimental error in rupture force according to estimated relative density of the supports (for ttl=150 μm) 83
Figure 4.48 Summary of relative density with laser power and scan speed 84

List of Tables

Table 2.1 Support Performance (Adapted from [56]) 26

Table 3.1 AddCreator-AC210 characteristics 34
Table 3.2 Power curve of laser of AddCreator-AC210 machine 34
Table 3.3 Particle size distribution 35
Table 3.4 Physical data 35
Table 3.5 Trade-off of different probes for supports testing 37
Table 3.6 Main geometric parameters available for Block Supports (adapted from [73, 74]) 40
Table 3.7 Final DoE of the support region of the specimens - factors and levels (full factorial) 43
Table 3.8 Final DoE combinations of support specimens' parameters 43
Table 3.9 Classification of specimens according to the support geometry 44
Table 3.10 Final scanning parameters used in the solid parts of the support specimens . 44
Table 3.11 Definitive DoE combinations of density specimens 46
Table 3.12 Work hardening curve introduced in Ansys [76] 52

Table 4.1 Rupture force results 55
Table 4.2 Analysis of Variance for F_{rupt} 56
Table 4.3 Model Summary 56
Table 4.4 Analysis of Variance for F_{rupt}, considering an adjusted response for specimen 15 58
Table 4.5 Model Summary 58
Table 4.6 Average density results 62
Table 4.7 Analysis of variance of relative density results 65
Table 4.8 Relative density Model Summary 66
Table 4.9 Resilience moduli of specimens 75
Table 4.10 Comparison of resilience of detached and attached supports (before testing) 76
Table 4.11 Efficiency of the supports according to teeth width and penetration 80

Table B.1 Full DoE combinations of support specimens' parameters 97
Table B.2 Full DoE combinations of density specimens 98

Table D.1 Classification of specimens according to the support geometry and chart labeling 109

Nomenclature

Abbreviations

AM	Additive Manufacturing
AR	Aspect Ratio
BJT	Binder Jetting
C	Circularity
CAGR	Compound Annual Growth Rate
DED	Direct Energy Deposition
DF	Degrees of freedom
DoE	Design of Experiments
EB	Electron Beam
FDM	Fused Deposition Modeling
LB	Laser Beam
ME	Material Extrusion
MIM	Metal Injection Moulding
MS	Mean Square
O_2	Oxygen
PBF	Powder Bed Fusion
SLS	Selective Laser Sintering
TLM	Tiled Laser Melting
TPMS	Triply-Periodic Minimal Surface

Symbols

δy	Displacement
ε	Strain
σ	Stress

σ_{uts}	Ultimate tensile strength
A_d	Defect area
A_s	Thread surface area
$A_{contact}$	Contact area of the supports at interface
d_L	Laser beam diameter
d_{rel}	Relative density
E_d	Energy density
$F_{allowable}$	Allowable tensile force
F_{rupt}	Rupture force
h	Hatch distance
l_0	Initial specimen length
l_z	Layer thickness
P_L	Laser Power
R_m	Stud tensile strength
r_{major}	Largest defect ratio
r_{minor}	Smallest defect ratio
$R_{p_{0.2}}$	0.2% proof stress
U_R	Modulus of resilience
v_S	Scan speed
d	Thread nominal diameter
n	Safety factor
P	Defect perimeter
p	Thread pitch
ttl	Tooth Top length

Chapter 1

Introduction

1.1 Scope and motivation

With the growing interest in additive manufacturing by different sectors of the current industry, Adira has recently launched an innovative equipment - AddCreator-AC210. Equipped with Tiled Laser Melting (TLM) ® technology, it has been possible to manufacture large parts with the laser powder bed fusion process.

This machine is equipped with a 5 lasers-process head and a large build volume of 1x1x0.5 m^3. The Tiled Laser Melting (TLM) ® concept's uniqueness comes from a movable process head assembled on a gantry system and a build platform that is divided into stripes, which are, then, divided into tiles. The process head moves along over the powder bed, keeping a small gap from it. The ideal conditions are kept and controlled inside the process head chamber, making it possible to manufacture parts with bigger dimensions than this chamber. The equipment is able to function with synchronous and simultaneous movements of the process head and the powder application systems, thus increasing productivity.

The necessity to add supports to geometries with overhangs larger than 45 degrees is still a limitation of this technology. The manufacturing of this support structures requires the rigorous adjustment of the process parameters because on the one hand, the supports must display enough strength to prevent warpage in the parts. On the other hand, if the supports are too bulky they become difficult to remove without machining or other types of subtractive processes during post-processing stage, resulting in costly and even impossible tasks.

Larger parts highlight the difficulty of finding this balance and its importance. They are susceptible to more severe and critical warping endangering not only the final product's quality but also the surrounding equipment. However, they are also harder to handle, making it a bigger challenge to perform the post-processing operations.

This dissertation will focus on the optimization of process parameters in LPBF, to ensure adequate support and to facilitate the supports' removal. The main steps will be literature review and AM training, definition of a design of experiments (DoE), manufacturing of the samples according to the DoE and, finally, the testing and analysis of the results and the final conclusions.

1.2 Objectives

The main objectives of this dissertation are the following:

- Evaluation of different types of supports and optimization of process parameters for their function - ease of removal and efficiency in heat transfer.
- Creation of a methodology for optimization of supports' parameters.
- Analysis of solutions and suggestion of improvements in Adira's solution.

1.3 Layout

This dissertation is divided into five main chapters, as follows:

- Introduction: motivation, expected steps and objectives.
- Literature Review: containing an overview of the state of the art of the market trends of additive manufacturing, as well as the metallic AM emerging technologies. Laser Powder Bed Fusion is explored in more detail and current solutions for supports structures are summarized.
- Experimental and numerical details: includes a description of the equipment, and experimental methods. Contains a brief report on a failed attempt at building the samples and the modifications that lead to a successful build job.
- Results and Discussion: where the results are presented and discussed.
- Conclusion and Future Work: summary the most relevant know-how obtained from the experiments and propositions of future investigations, methods or studies that would be interesting to continue.

Chapter 2

Literature review

2.1 Additive Manufacturing technologies

Additive manufacturing differs from traditional subtractive manufacturing and forming processes because three-dimensional parts are created by successively adding layers of material. Advances in these technologies have brought freedom of design, the possibility of weight reduction, agile manufacture and lead time reduction, elimination of tooling [1] and in-situ manufacturing, reducing inventory. These attributes are especially interesting for prototyping, manufacturing small batches, customization [2] and topology optimization and are used in industries like aerospace, medical, dental and automotive.

Generally, an AM process has three main phases: Pre-processing, AM Production phase and Post-processing. The first stage includes CAD design, CAE simulation, topology optimization (optional) and finally, creation of data transfer files such as ".STL", which prepares the geometry to be sliced into the layers for manufacturing. In the production phase, the files are loaded to the AM machine, which builds the part accordingly. The component is, then, extracted and submitted to the post-processing operations like cleaning, heat treatment, support removal, machining and quality assurance [2].

Due to the wide variety of AM processes that have been created in recent years, the standard ASTM F2792-12a, classifies Additive Manufacturing technologies into the following seven categories [1, 3]:

- Material Extrusion: material in a semi-solid state is deposited selectively through a nozzle;
- Material Jetting: droplets of build material are selectively deposited;
- Binder Jetting: droplets of a bonding agent are selectively deposited on a powder bed to join powders of the build material;
- Sheet Lamination: sheets of the build material are bonded and cut into cross-sections of the desired geometry;

- Vat Photopolymerization: A liquid photopolymer or resin is selectively solidified by a reaction with light;
- Powder Bed Fusion: thermal energy is used to selectively fuse regions of a powder bed;
- Direct Energy Deposition: focused thermal energy is used to fuse materials by melting them as they are deposited.

This is the general classification for AM processes regardless of the material used. Considering the metallic application, out of these processes, represented in Figure 2.1, Material Extrusion and Binder Jetting are suitable for metallic-based filaments and metallic powders, respectively, and require sintering operations to obtain the final part. Sheet Lamination can be used to manufacture metallic parts by bonding metal sheets either by welding or adhesive bonding. Finally, Powder Bed Fusion is used with metallic powders and Direct Energy Deposition can be used with metallic powders or wires and both fuse the layers by melting.

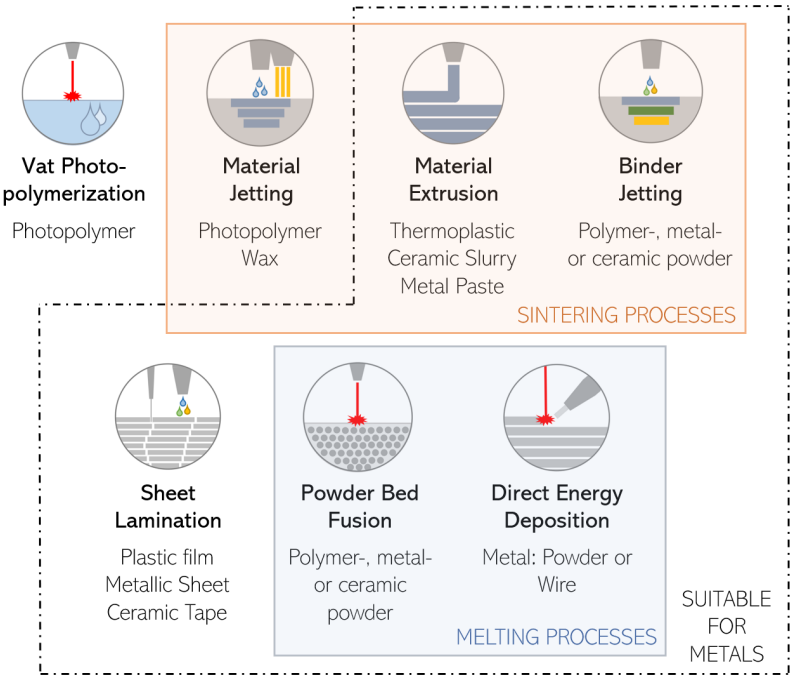

Figure 2.1: AM trend indication of European Business by category (adapted from [3])

2.2 Future Market Trends in Additive Manufacturing

The first steps in Additive Manufacturing started with polymeric materials in the end of the 1980s, with the first Electron Beam PBF patent being filed in 1993, followed, in 1997, by a patent describing Laser Beam PBF - "basic ILT SLM patent". Although AM processes are still a niche in the global metal processing market, currently, series production readiness has been achieved, automation concepts are available [4] and the future market trends seem clearly positive for these

type of technologies. To fulfill the increasing needs and requirements of the industry with high productivity and low cost, there is a trend of automation in industrialization. The introduction of new principles and materials allied with reduction of waste and appropriate energy balance over a part's life-time have the potential to positively impact sustainability [5]. As of May of 2021, according to CECIMO (European Association of the Machine Tool Industries and related Manufacturing Technologies), the balance of Growth - Decrease in all categories of AM is positive. The maximum growth was found in AM products, produced parts and AM materials, at 39% and the lowest for AM services, at 31% [6], as it is shown in Figure 2.2. Another important indicator is an expected growth balance of 40% on the use of metal in AM [6], the second highest trend among the materials represented in Figure 2.3. The most important clients for AM technologies and products are the Medical and Machinery sectors and due to the positive trend indications, the AM Confidence Index is high and the fast-growing path is expected to continue both in Europe and internationally.

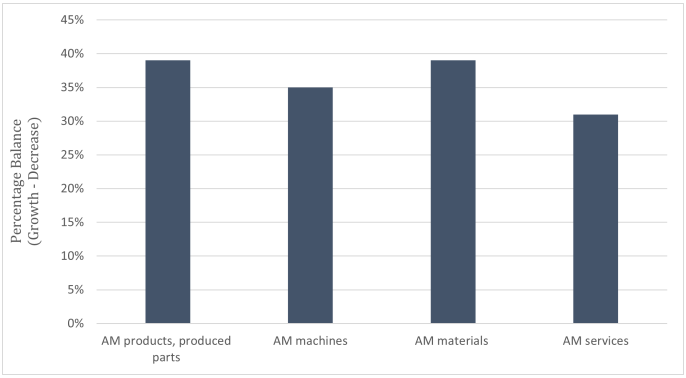

Figure 2.2: AM trend indication of European Business, by category (adapted from [6])

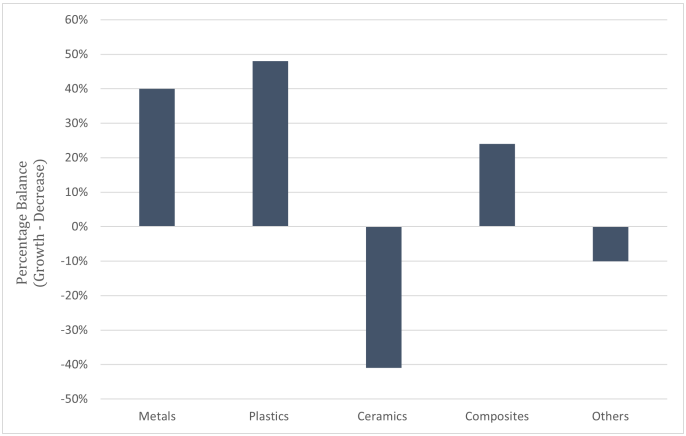

Figure 2.3: AM trend indication of European Business, by material (adapted from [6])

The aforementioned growth in additive manufacturing technologies and in the use of metal in them is estimated to result in a Compound Annual Growth Rate (CAGR) of 25.5 % in metal AM

until 2026, from an initial market size of 2.50 billion EUR in 2021 (see Figure 2.4). The leading industries for AM are Medical and Space, followed by Industry and Automotive with 16%, 16%, 11% and 8% of share of system sales revenue in 2021, respectively [7].

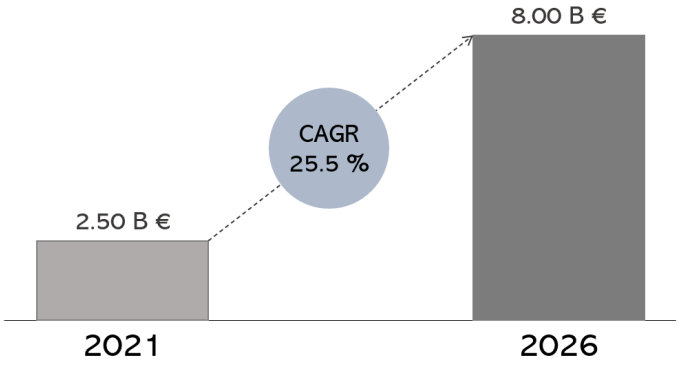

Figure 2.4: CAGR in metal AM until 2026

More specifically, Powder Bed Fusion also shows encouraging indicator, having been the leading AM technology in 2020, with 40% of share of metal system sales revenue [7]. Before PBF (the main focus of this work) is more deeply analysed, other processes and innovations in the field of metallic AM are presented in the following sections.

2.3 Metal Additive Manufacturing

Metal Additive Manufacturing can be broadly categorized into two main groups, sintering-based and melting- or fusion-based processes. Sintering-based processes may be considered indirect technologies since they usually require at least three operations to be manufactured: additive creation of a green part, debinding of the green part to obtain a brown part and a sintering operation to obtain the densified final part. This is not the case for all sintering technologies. Selective Laser Sintering (SLS), for example, isn't used for green part production. However, in recent years, novel sintering technologies have been developed with this three-part process in mind and they have gained interest, due to their potential to achieve higher through-put and overall lower cost per part, compared to direct technologies. However, the supplier landscape for sinter-based processes is far less developed for industrial applications [5]. In melting-based AM technologies, the metal powders are melted as the part is built, fusing the layers together. These are more widely used in the industry today and have been the subject of Research and Development projects over the years [5]. In Figure 2.5, a summarized overview of these technologies is presented and they are each explored in more detail in the following subsections.

2.3.1 Sinter-based Processes

Sinter-based metal Additive Manufacturing technologies are an evolution of AM processes originally created for polymers. They have combined some processing steps from Metal Injection

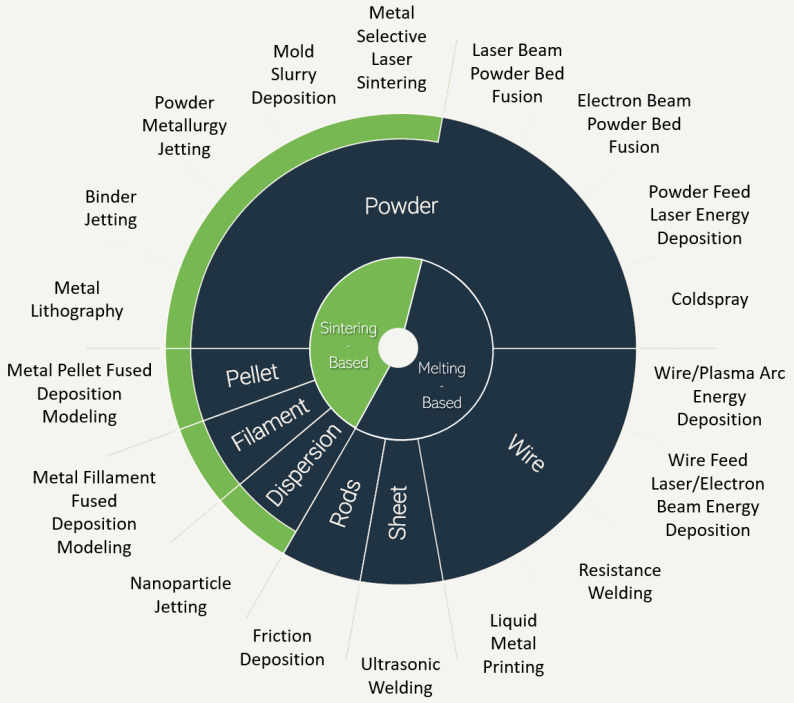

Figure 2.5: Sinter-based and Melt-based technologies (adapted from [5])

Molding, such as, required specific post-printing operations, namely debinding and sintering are necessary to achieve the required mechanical properties [8].

- **Printing** is the first step of the manufacturing process and it produces a green part, whose geometry is maintained by a polymer wax or binder that is mixed in the feedstock mix. This part is fragile and its strength depends on the amount and strength of the binder [8].
- **Debinding** produces a brown part by removing most of the binder (first stage) from the part and it becomes even more fragile. The second stage binder is only removed during sintering. Three types of debinding were adapted from the Metal Injection Molding industry: solvent, thermal and thermal catalytic debinding [8].
- **Sintering** creates the final geometry of the part and provides structural integrity and density of a metal part through heating at a temperature close to but under the melting point. The powder particles are bonded through a mass transport at the atomic scale. At first, powder particles are only bonded by Van-der-Walls forces. When the sintering temperature is reached, the particles are bonded but channels between them are still present. Next there is an increase of packing density and isolated pore structures are created. Finally, the pores decrease in size until almost full density is achieved. During this process, volume shrinkage from 16% to 21 % occurs [8].

Int the next sections, the main sinter-based technologies are described as well as some new emerging technologies:

2.3.1.1 Binder Jetting

This technology is based on the original MIT patent for "3D Printing". A green part is formed when metallic powders in a powder bed are joined by ink-jet nozzles that selectively deposit a fluid binder, which hardens when temperature of approximately 70ºC is applied [9]. The parts are separated from the powder cake in a manual depowdering process with compressed air or brushes, which can be challenging, especially in small cavities and thin walls since green strength is low. For bulkier parts, semi-automated solutions are possible [8]. The binder is then removed either by thermal debinding, leading to a brown part. Finally, the part is placed in a sintering oven, at a temperature close to the metal's melting point, to obtain the required mechanical properties [1, 10], as shown in Figure 2.6 a).

2.3.1.2 Metal FDM (Material Extrusion)

The company Stratasys introduced the first Material Extrusion (ME) system in 1991 and coined the term Fused Deposition Modeling (FDM). This process is commonly used with thermoplastic materials, however, it is possible to apply to metal wires or to filaments made of metal powder mixed in a polymer binder [10]. The metal-based filaments needs suitable viscosity to be processed, heated and dispensed through a nozzle as the building table or the extrusion head moves in x-y direction to build each layer [1, 9]. Due to higher thermal conductivity of the metal-filled filament compared to typical thermoplastics, the nozzle has specific requirements to ensure the transportation of the softening material, which makes the printing head the key difference between metal and polymer FDM [10, 9], the nozzle has specific requirements. The typical nozzle diameter ranges from 0.1 to 0.5 mm. After all the layers are printed and the green part is obtained, the parts goes through thermal catalytic debinding at about 120ºC [8] and sintering operations are required (Figure 2.6 b)). In metallic ME, volume shrinkage is anisotropic and higher in the z-direction due to gravitational forces [8] and a uniform temperature distribution during the shaping process is important to prevent distortion and warpage due to thermal stresses. Some advantages of metal ME include lowe machine costs and ease of operation and filament change [9].

2.3.1.3 Powder Metallurgy Jetting

Stratasys has been developing a new technology called Layered Powder Metallurgy, which consists of three steps: dispensing and rolling, compaction and, finally, printing. In a non-inert environment, a layer of powder is made by rolling the dispensed powder. Secondly, this layer undergoes a compaction phase, in which it becomes thin and dense. Finally, a wax-based material is jetted at the part's contours and this process is repeated as sheets of powder are stacked to form the final geometry. Once built, the tray is subjected to cold isostatic pressing to increase density up to 99%, the de-waxing process evaporates the printed boundaries and finally, the part is sintered to obtain the necessary mechanical properties, as shown in Figure 2.6 c) [11]. This technology has the potential to provide faster printing times and lower costs, since it enables the use low-cost Metal Injection Molding (MIM) powder.

2.3.1.4 Metal Lithography

In 2019, INCUS and METSHAPE developed Lithography-based Metal Manufacturing (LMM), a new technology based on the well-established Stereolithography to build green metal. The feedstock is a photopolymer resin filled with metal powder (approximately 50vol.%), which is spread out in a thin layer (typically $20-50$ μm) and later cured selectively by a ultraviolet light, like it is seen in Figure 2.6 d). Like all the other sinter-based technologies, after the build, the green part undergoes debinding and sintering [5, 12]. Metal lithography shares several advantages with stereolithography, such as excellent accuracy and low cost [5]. Besides, Vat Photopolymerization is nearly 100% material effective, which makes it suitable for processing precious metals and supply-critical materials [9].

2.3.1.5 Metal Selective Laser Sintering

The SLS process is mature and widely used in the industry, usually in polyamide for judging kinematic functionally due to its adequate mechanical properties and surface finish. The startup HEADMADE MATERIALS invented Metal SLS, in which, instead of polymer feedstock, a powder compound made of polymer and metal powder is used. The build chamber is heated yo a temperature close to the glass temperature of the polymer (Figure 2.6 e)). The laser melts the metallic powders, however, full melting does not occur, meaning that the core of the metal powders remains solid and the molten portion acts as a binder to form the green part, which is then debinded and sintered, similar to what happens in Metal FDM and BJT [5, 13].

2.3.1.6 Mold Slurry Deposition

For making ceramic parts in AM, the Mold Slurry Deposition procedure is well-known. Tritone has developed MoldJet ^{TM} and presented a machine for this process in 2019. It contains a horizontal carousel that rotates the working platform to the different stations. In the first, a polymer wax is printed to form a mould, which is filled with a slurry made of metal powder and binder in the following station. Next, the working platform moves the newly-formed layer into the thermal phase for hardening. This process is repeated throughout the layers at an industrial speed. Then, the mold is chemically dissolved, resulting in the separated green parts, which are then debinded and sintered [14]. This machine was presented with a built-in quality control system and may process a variety of materials including steels, titanium alloys, and copper- and nickel-based alloys [5].

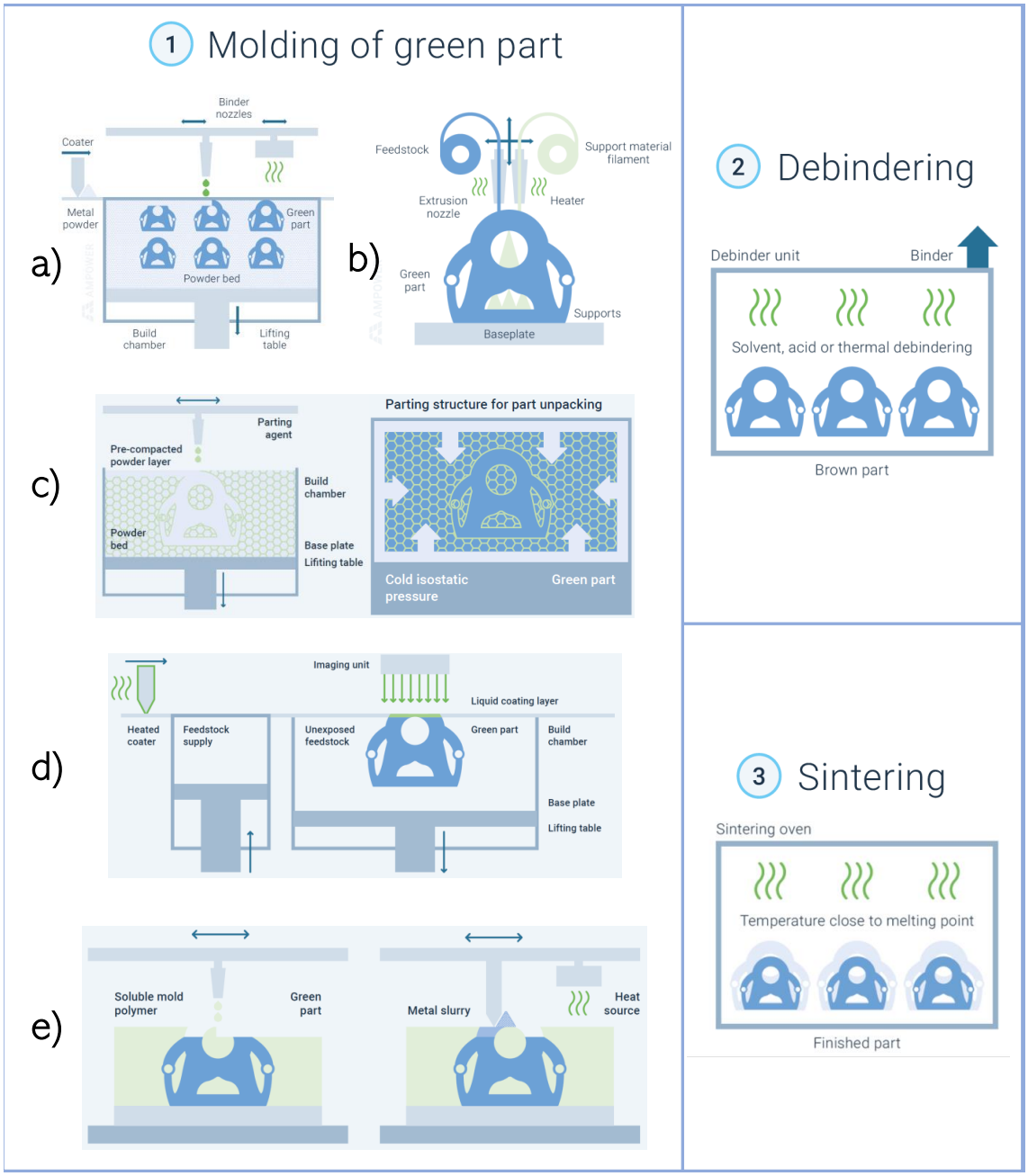

Figure 2.6: Schematics of some sinter-based technologies (adapted from [5])

2.3.2 Melting Processes

2.3.2.1 Powder Bed Fusion

Powder Bed Fusion (PBF) is a process that uses thermal energy to melt metallic powders. A levelling system (roller or brush) spreads a thin layer of powder, with the predefined layer thickness, onto a substrate that is fixed to the building platform. A thermal energy source selectively fuses regions of a powder bed, which solidify according to the desired cross section geometry as it cools down (Figure 2.7). After this step, the building platform is lowered in the vertical direction in a distance corresponding to the layer thickness. This process is repeated until all the layers are manufactured and the full part is obtained. The process takes place at a controlled environment, purged with nitrogen or argon until the oxygen content is less than 0.1%.

According to the thermal energy source, most PBF processes can be characterized either as Laser-Beam PBF or as Electron- Beam PBF [15]. The focus of this work is Laser-Beam Powder Bed Fusion. Laser-Beam PBF creates solid parts of high density, over 99,5%, usually runs at room temperature and provides layer thickness of 30 μm to 60 μm [16]. Good surface finish and roughness and the capacity to reproduce fine details are strengths of LB-PBF. Electron-Beam PBF requires pre-heating of the powder bed to temperatures from 600ºC to 1100ºC, which results in a lower cooling rate of the layers, coarser microstructure and less distortion [16]. EB-PBF is somewhat more expensive, but also, faster than LB-PBF [1].

Powder Bed Fusion is considered an evolution of polymer selective laser sintering and is now the largest and most relevant AM technology for the near-to-medium-term future.It has been subject to the most research and efforts of industrialization out of all AM technologies and has now achieved a high level of standardization and automation. However, especially for processing metals, this technology also poses some challenges related to high complexity [1], high capital expenditure (facility requirements and operation costs), efficient process monitoring, cost of compatible powders and difficulties in support removal [15].

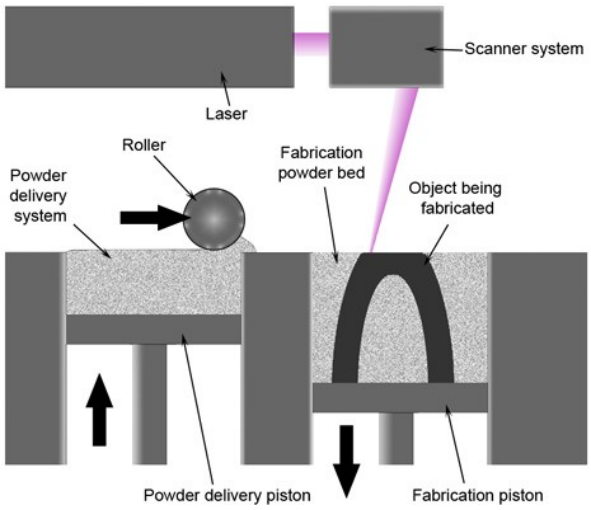

Figure 2.7: Powder Bed Fusion [17]

2.3.2.2 Direct Energy Deposition

Direct Energy Deposition (DED) uses thermal energy to fuse the metallic material at the same time as it is being deposited (Figure 2.8). The thermal source is typically a laser beam or an electron beam and the material feedstock can be metallic powders or metallic wire [1]. Other variants fuse the layers by contact welding (kinetic energy due to hyper-sonic speed) and another feedstock possibility is using, also metal wire fused with an arc, instead of powders [18]. This process has the capability to produce near-net-shape parts, which means they usually require machining or other subtractive processes to reach the required dimensional tolerances and surface finish [15]. Still, this process provides some unique capabilities - most systems use 4- or 5-axis motion to position the deposition head so the movement is not limited to horizontal layer and, therefore, this process become especially useful for repairing, cladding and adding features to existing parts. Another important advantage is the possibility to deposit more than one material simultaneously, making the manufacturing of functionally graded materials possible [1].

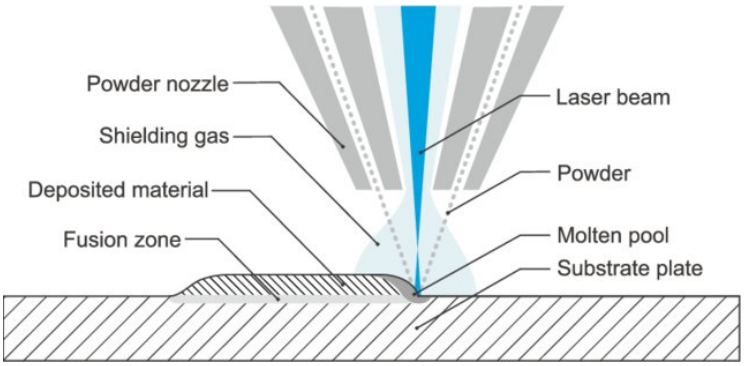

Figure 2.8: Direct Energy Deposition [19]

2.3.2.3 Resistance Welding

This is a relatively recent technology, invented by DIGITAL ALLOYS in 2019, under the name of Joule Printing ^{TM}. This system can be characterized as a variant of DED and is based on a thermo-electric process, as shown in Figure 2.9. The feedstock is a metal wire, which is pushed though a nozzle. At the interface of the base material and the wire feedstock, heat is generated so that they are joined by having electrical current passing through them for a precisely controlled time. This raises the temperature at the point of contact, and a combination of melting and material diffusion at the interface results in the bonding. [5]. Joule Printing ^{TM} has the advantage of being fast (depositing metal at over 5kg/h) and presenting better resolution and surface roughness than wire-DED [20].

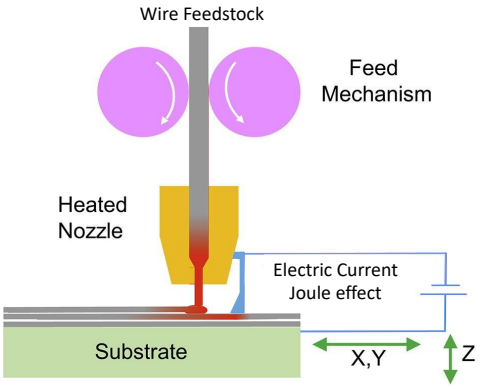

Figure 2.9: Resistance welding - Joule Printing (adapted from [21])

2.3.2.4 Friction Deposition

This method uses knowledge transfer in friction welding and is based on patents that go back to the 1950s, but the specific technology is in the testing phase of series production. Friction Deposition is a very simple technology, compared to DED and PBF [22]. A metal rod or powder is deposited in the substrate by friction created by high downward forces and rotation. This movement generates enough heat so that the material flows freely (Figure 2.10). This step is immediately followed by layer contour machining and plastic deformation, forming a layer [22]. A limitation of this technology is the strong restriction on design freedom. However, uniform material properties and high throughput make this technology interesting for producing blanks, which is particularly interesting for alloys that are difficult to weld and that are not available in the desired dimensions [5]. With Friction Deposition it is possible to obtain material combinations in both radial and normal directions [22].

2.3.2.5 Liquid Metal Printing

Liquid Metal Printing was presented in 2013 by a startup called VADER SYSTEMS, which has, since then, been acquired by XEROX. The system makes use of molten metal droplet to create the part directly, layer by layer. The feedstock is common welding wire, providing the advantage of low cost. The wire is fed into a melting pot that is inductively heated, and at its bottom, the material flows through a small nozzle that is surrounded by an electromagnetic field. This field generates pressure on molten metal, leading to the formation and jetting of the droplets through the nozzle [24]. The droplets fall on he substrate and solidify almost immediately (Figure 2.11). Currently, there is research being developed to use this technology to process high strength aluminium alloys, which is not feasible with any other metal AM process [5]. With this technology, it has been possible to obtain droplet diameter of 50 μm [24].

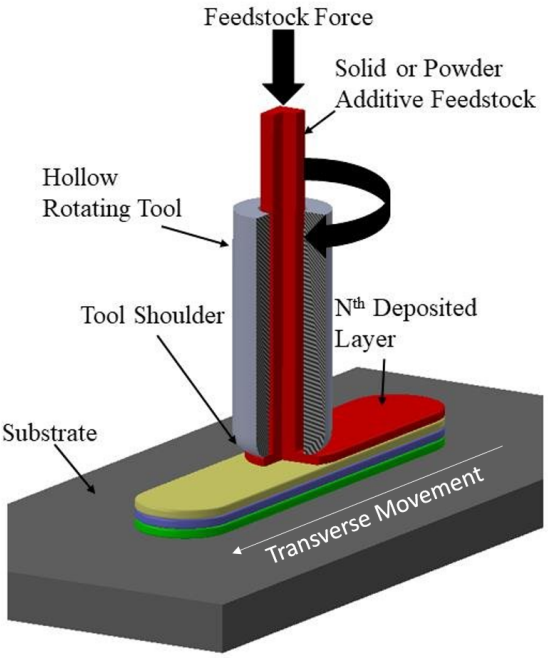

Figure 2.10: Friction Deposition (adapted from [23])

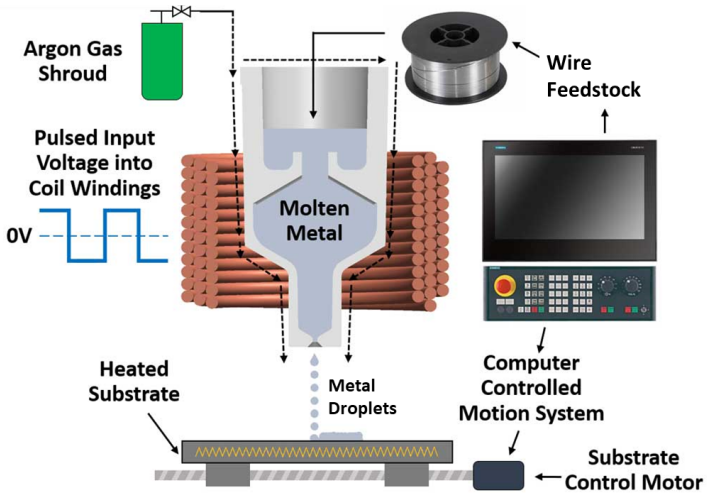

Figure 2.11: Liquid Metal Printing (adapted from [25])

2.3.3 Processes Comparison

Each technology has it strengths and limitations and it is necessary to consider the application before choosing the manufacturing process. For example, DED stands out due to the ability to use it for repairing parts. Binder Jetting has the unique advantage of not inducing delamination [26]. Powder Bed fusion processes are notable for high density achieved, while EBM and Binder Jetting induce low levels of residual stress. For complex geometries such as fine meshes, PBF and

Binder Jetting are the most appropriate techniques, but they add the process of sieving, handling and cleaning of the powder [26].

In Figure 2.12, AM technologies are compared on the basis of industrialization maturity and technology maturity, which describes the adoption rate of different processes in the industry, as of 2020.

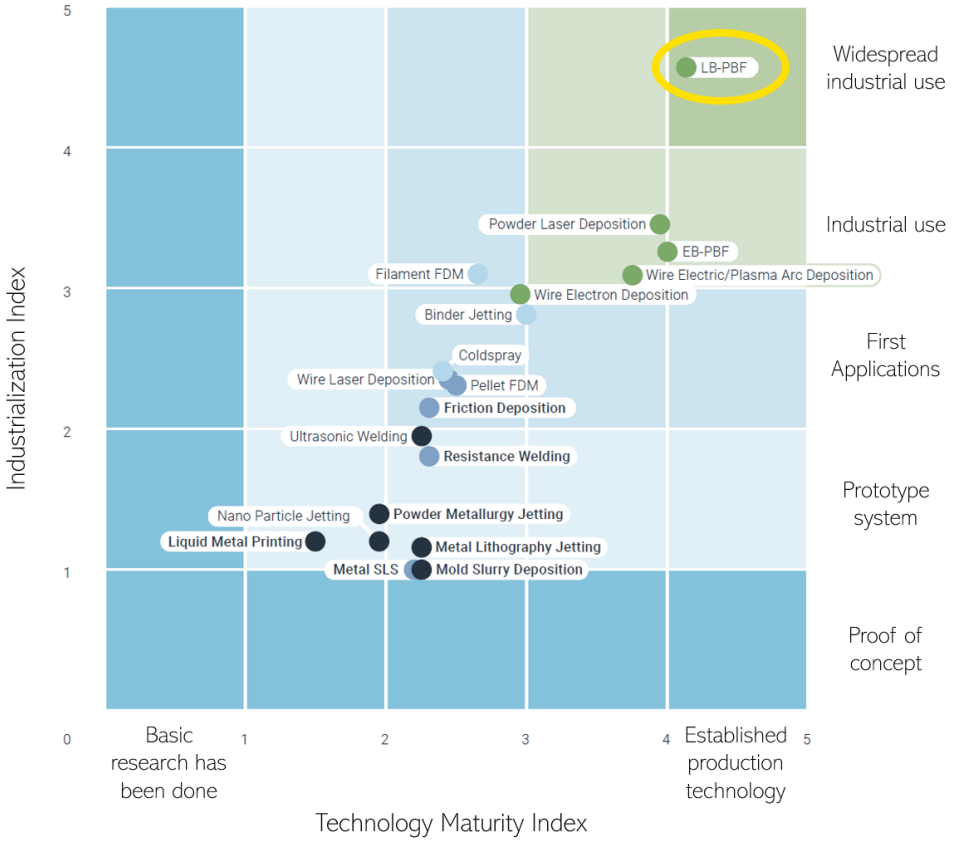

Figure 2.12: Maturity Index in 2020 for AM technologies (adapted from [5])

Only Powder Bed Fusion and some Direct Energy deposition processes have reached enough basic R&D to establish full-scale series production with integrated periphery and high repeatability [5]. LB-PBF has the highest penetration in industry [5] and provides higher printing resolution but slower building rates. When using Electron Beam Powder Bed Fusion, the resolution is lower but the process is faster. Finally with DED, the resolution reduces significantly, but it has the advantage of being faster than LB-PBF [4] and providing more degrees of freedom.

Laser Beam PBF is especially well established for production since this technology enables the production of parts with maximum density, hardness, yield strength and ultimate tensile strength after heat treatment [10]. With LB-PBF it is possible to obtain lower surface roughness, both Ra and Rz [10] compared to metal FDM and DED, for example. Only Binder Jetting produces smoother surfaces in AM processing of metals [10]. When it comes to the cost structure, the data preparation is similar in LB-PBF and in EB-PBF [27]. The Laser Beam technology is more

expensive than Electron Beam Melting when it comes to machine setup, machine runtime, support removal and heat treatment [27]. Machine runtime is the main portion of the total cost [27], therefore it is possible to reduce the build time (and costs) by increasing the layer thickness, as long as the part doesn't require a density higher than 99.6%. In Binder Jetting, the cost of the machine and of the material are comparable for 10% packing density, with the sintering cost being negligible. For higher packing densities, the material cost becomes the main factor, which is also the case in metal FDM [10].

From Figure 2.12 it is possible to understand that LB-PBF is currently widespread and used across multiple industrial applications, which means it is approaching series production capacity [28]. There is a high knowledge base and dedicated research programs, material availability, and a competitive market is forming, with more than 40 suppliers of LB-PBF technology suppliers known worldwide [28]. This technology will be the focus of the next sections and chapters.

2.4 State of the art of the LB-PBF process

PBF is the leading AM technology (40% of the metal market and 16% of polymer market) [29]. Out of a total of 2108 metal AM systems sold in 2021, 1533 units were PBF machines. This represents 6% increase in units but a 11% increase in supplier revenue due to the higher complexity and costs in new systems [29]. Laser PBF grew as well, passing 1500 sold machines in 2021 and the focus has been on improvements in robustness and productivity. As laser PBF becomes more mainstream as a production tool, there are already some efforts to mitigate some of the setbacks of this technology. One of them is the size limitation. In 2020, SLM launched a LB-PBF machine with 12 lasers and 600 mm platform size, kicking off the race towards bigger PBF systems. Today, 74% of sold LB-PBF machines have a platform size smaller than 350 mm and only 2% offer sizes larger than 600 mm. The first customers for machines with bigger build platforms were Space, Automotive and Energy sectors [29]. Another setback is, as was discussed in previous section, reducing lead times (increase productivity) and gaining the capability to produce larger parts (useful for automotive and aerospace applications). One of the possible solutions for these concerns is the use of multiple-laser technology, which is a popular solution to increase productivity. In 2021, 46% of machines had 2 or more lasers and the buyer forecast for 2026 shows only 12% of machines having a single laser, as it is shown in Figure 2.13. This shows that buyers are interested in the higher throughput made available by multi-laser to reduce the costs of their parts [29].

Having more lasers doesn't necessarily provide higher productivity. Still, this strategy can be a solution for components that couldn't be printed in a cost-effective way on single-laser machines. An important aspect of multilaser machines is the concept of overlap, which is the area of the powder bed that can be processes by two lasers. Generally, having more overlap tend to increase productivity, while less overlap results in the coverage of a larger area on the powder bed. This is especially useful to produce large parts and also allows the usage of a larger building space, providing a solution for printing more parts at once [30].

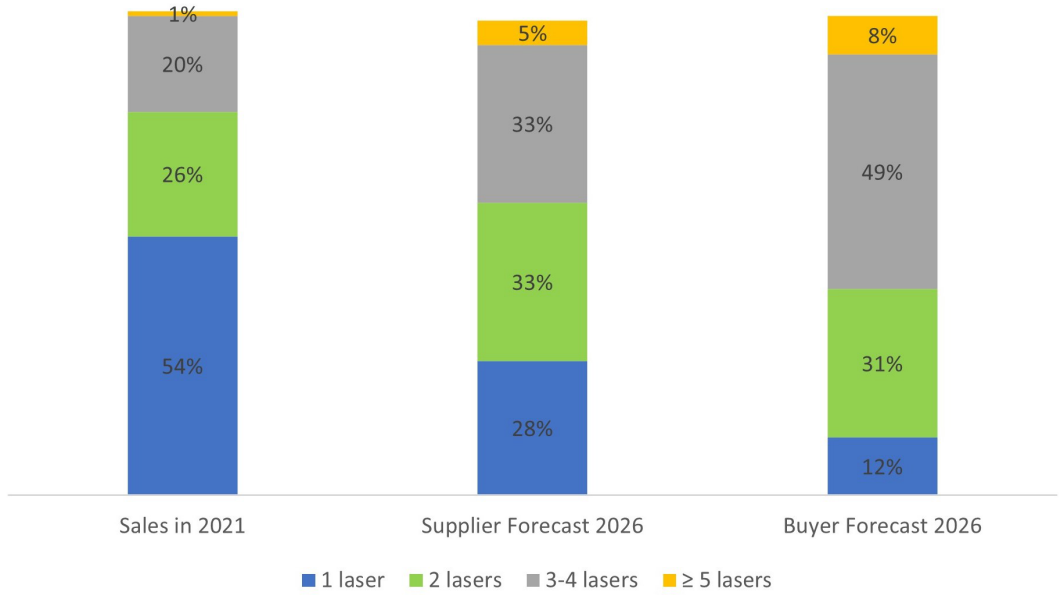

Figure 2.13: Share of lasers per PBF Machine in 2021 and 2026 Forecast (adapted from [29])

Although multilaser systems enable these advantages, it is important to account for possible issues during this type of process, as it can induce specific defects in parts that are not found in single laser fusion. When producing large parts, two lasers interact on a region of the powder bed, which can lead to alignment issues. If the lasers' work zones are not properly aligned, defects like surface marks, unmelted powder may be found. Currently strategies to fix alignment have been developed and this issue is not as critical [30, 31, 32].

Another relevant aspect is the control of gas flow. In all types of LB-PBD, gas flow's function is to evacuate the condensate and particulate from the melting of the laser. Since the production of these particulates happens at a much higher rate in multi-laser systems, the control of gas flow gains additional importance.

Overall, the most crucial aspect is to guarantee uniform properties along the lasers, so the thermal load on each laser has to be the same. Therefore, it is important to develop strategies to find the best balance between productivity and part quality. For example, it has been verified that by adding a second laser to the build, it was possible to decrease production time by 47%, while maintaining comparable or better density, hardness, tensile strength and high cycle fatigue cycle, after heat treatment, than the nominal material properties [33].

It is possible to see that multi-laser machines bring higher level of complexity, but most importantly, more flexibility. To achieve this, software also plays a major role, as well as the investigation on the usability of new alloys in metal AM.

Adira's AddCreator-AC210 is based on the PBF concept presented earlier. It is equipped with 5 lasers of 400 W each, that can work simultaneously on the powder bed. The main innovation in the Tiled Laser Melting ® solution is the movable process head that allows the production of larger

parts or the production of more quantity, by enabling larger batch size, in its building envelope of 1x1x0.5 m^3 (Figures 2.14 and 2.15). The powder bed is divided into 3 stripes which are divided into tiles, which are smaller rectangular areas processed by each laser at a given position.

Assuring appropriate atmosphere conditions (oxygen concentration under 2000 ppm) in the entirety of the machine volume's atmospheres would increase complexity of the equipment and costs of the utilization, making it impossible to have such a large building platform. This capability is possible due to the ability to control the atmosphere locally inside the process head chamber with the shielding gas system.

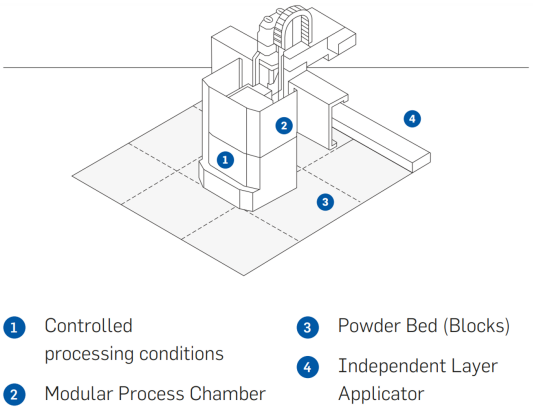

Figure 2.14: Schematics of AddCreator-AC210's Tiled Laser Melting solution

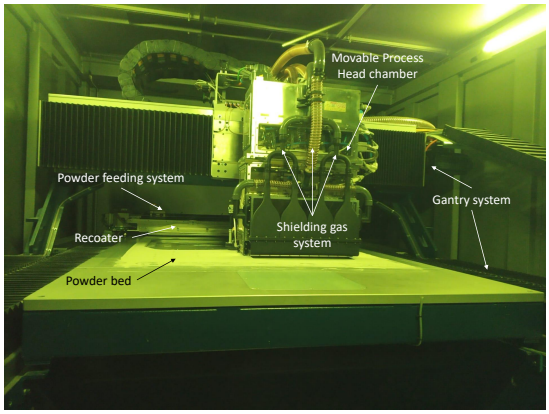

Figure 2.15: Real AddCreator-AC210 system

2.4.1 Process Parameters

One of the reason behind the complexity of laser PBF is the large amount of parameters involved in the process, that can be over one hundred in modern machines [34]. The processing conditions depend on the material and comprise two main types of variables: machine settings (which are usually provided by the machine manufacturers and not usually modified) and process parameters, which may be altered from one build job to another. The most commonly considered manufacturing parameters are [35]:

- Laser-related
  - laser source: in powder bed fusion, CO_2 lasers are used for thermoplastics, while fibre lasers are implemented in metallic systems [36].
  - laser power: quantifies the total energy output. In PBF, the nominal power of lasers is usually under 1000W, with the most common values ranging from 200 to 800W
  - laser beam diameter: influences the dimensional accuracy, thereby this parameter should be as reduced as possible. It is usually under 100 μm [37].

  - beam quality: characterizes the intensity profile and is used to predict the focus of the beam. Determines the minimum theoretical spot size, which is equal to 1 for a Gaussian distribution [38].

- Scan-related
  - scan speed: is a crucial parameter and affects not only part properties but also productivity.
  - hatch distance: distance between successive laser passes vectors,
  - scanning strategy: refers to the combination scan vectors' length, orientation and pattern along a layer. It can influence heat transfer and the distribution of residual stress formation in a part. Some common patterns are: unidirectional, bi-directional, zig-zag and spirals [38].

- Powder-related
  - layer thickness: height of a single powder layer. Strongly impacts part quality (resolution), production time and costs. Typically, thicknesses under 70 μm are used [27].
  - powder size: the nominal distribution of powder size used in PBF is 16 μm to 45 μ [39].
  - particle distribution: should be fine and uniform [39].
  - powder morphology: measures the shape of individual powder particles in terms of aspect ration, circularity and elongation [38]. Sphericity is an important requirement to ensure adequate flowability.
  - powder density: some intrinsic porosity may be induced in the powder particles during the atomization manufacturing process; to avoid this, the production must be tightly controlled.

- Environment-related
  - oxygen concentration: should be controlled to prevent the formation of metal oxides during the scanning. It is typically kept under 2000 ppm.
  - gas flow: inert gas such as argon or nitrogen are injected into the build volume to lower oxygen concentration.
  - environment temperature: may impact the heat balance and residual stresses.

The most important process parameters are schematized in Figure 2.16.

Controlling the main process parameters is key to achieving adequate part quality because the inherent characteristics of the process induce different complex aspects derived from the interaction of the laser with the metal. Thermal gradients may lead to residual stress and uneven cooling rates, unexpected phases may occur and chemical composition may be affected [34].

One of the most relevant and highly investigated quality indicators of metallic AM is the relative density because it strongly influences mechanical properties [41]. One type of porosity is

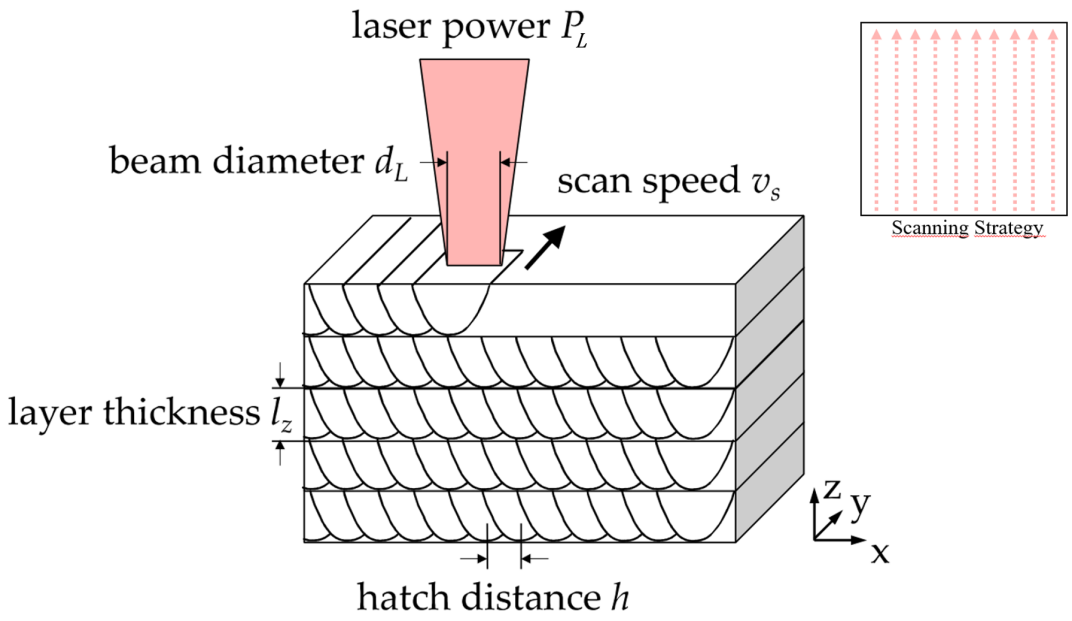

Figure 2.16: Schematic of main LPBF parameters (adapted from [40])

cause by lack of fusion, which may due to insufficient energy input (low laser power and high scan speed), overly thick layers and hatch distance being too large causing insufficient overlap. The small melt pool causes incomplete melting of the material. Another type of porosity is keyhole porosity, caused, on the other hand, when energy density is too high (high laser power and low velocity), causing the material to be vaporized leaving entrapped gas inside the part [34]. This type of defect is controlled by melt pool dynamics [34] and tends to result and smaller and more regular-shaped pores than lack of fusion.

Another defect called "balling" happens at high levels of both power and scan speed, causing high instability and high convection in the melt pool due to the complex physical and chemical interaction of the laser with the melt pool [42]. This defect happens when the metal solidifies in the shape of small balls. Irregular, ellipsoidal ball formation is known as the first type of balling and this defect is characterised by a dimension of 500 μm. The second type of balling is caused by melt pool splashing due to high velocity and is represented in small spheres of approximately 10 μm [42].

This behaviour is summed up in Figure 2.17, which indicates the need for a balanced energy input. The exact optimal values, however, are dependent on each type of system and material. This amount of energy is often quantified by the volumetric energy density, given by Equation 2.1, where P_L is the laser power, v_s is the scanning velocity, h is the hatch distance and l_z is the layer thickness [40].

$$E_d = \frac{P_L}{v_s * h * l_z} \tag{2.1}$$

This can also be defined as surface energy density by eliminating the hatch distance variable from the equation or defined as linear energy density by eliminating the hatch distance and layer thickness.

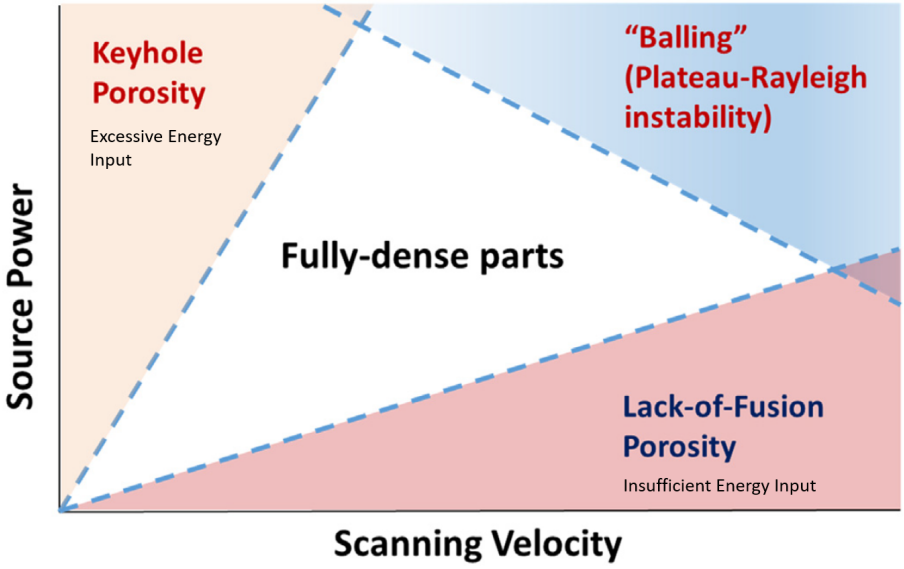

Figure 2.17: Types of porosity found in LPBF parts (adapted from [34])

2.4.2 Materials and Powder Characteristics

Like in all manufacturing processes, the material is a critical aspect of the outcome. As was already mentioned, the material feedstock in PBF is composed of layers of powder, which should have some basic characteristics to ensure the success of the process, namely: high sphericity, uniform size (tight particle-size distribution), good flowability, low water adsorption, chemical stability and high packing density. Flow and spread are critical to achieve the desired layer density and part quality [1] and that is why the sphericity is so important in AM. It is also important that the powder is free of fine powders and has a low oxygen content. These requirements lead to the necessity of having a careful control in the atomization process [15]. Usually, the water atomization is reliable in powder metallurgy, however it causes the metal droplets to solidify rapidly, resulting in irregular shapes. Therefore, plasma and gas atomization are preferred [1]. As for the raw metal used to manufacture the powders, the metallic applications in L-PBF revolve around three main elements: iron, titanium and nickel.

Steel and iron based alloys have been discussed in many publications - Stainless Steels accounted for 18% of the share of metallic powders used in AM in 2021 and Tool steel alloys represented 10% [29]. With the first paper on 316L stainless steel being published in 2005 and 99,9% density being reported on processing this material in 2010. Other steel materials have been used as well, such as H2 high speed tool steel, H13 tool steel, 314S and 904L stainless steel and Maraging 300 [43]. It has been concluded that high power combined with low scanning speed

optimizes the density of the parts manufactured by PBF with these materials. Steels have high strength, ductility and biocompatibility, which make them useful in applications in the injection moulding field for conformal cooling, in the medical field and in the manufacture of lightweight structures[43].

Titanium and its alloys have also been extensively researched, especially Ti6Al4V [16] (other alloys like Ti6Al7Nb and Ti24Nb4Zr8Sn have also been used). These alloys show good biocompatibility, high specific strength and elastic modulus similar to the one of human bones, making this especially interesting for application in the medical and dental field. They have also been used to produce lightweight scaffold structures, which are important in the aerospace industry [43]. They pose, however, inherent challenges related to their high reactivity and sensibility to oxygen, hydrogen and carbon, in the liquid state which has limited their use in casting. In AM, these alloys are processed using an inert gas protecting atmosphere (argon, for example) and due to the localized and rapid heating and cooling, there is less tendency to obtain interstitial elements. Titanium alloys represented 25% of metallic powders used in AM in 2021 [29].

Nickel based super-alloys comprise another commonly used group of materials in L-PBF, especially INCONEL 625 and 718, Chromel, Hastelloy X (19% share of metallic powders for AM in 2021 [29]). They have excellent corrosion resistance and are especially useful in high temperature applications like swirlers in combustion chambers, turbine blades and turbocharger rotors, which potentializes their use in the aeronautical industry. INCONEL 718 and Hastelloy have the benefit of reaching nearly 100% density and having a higher ultimate tensile strength compared to their casting counterparts [43]. INCONEL 718 has the benefit of good weldability and low tendency to form cracks, due to the slow precipitation strengthening [41].

Other materials include aluminium, copper, magnesium, cobalt-chromium and tungsten alloys. For example, AlSi10Mg, a common casting alloy, is the most used Al alloy in PBF and has potential applications in the aerospace industry. Copper is difficult to process due to its high reflectivity, causing the energy consumption to increase and also due to its reactivity to atmospheric oxygen, even at low concentrations. Tungsten is costly and difficult to process do to high melting point and low wetability [43].

2.4.3 Post Processing

After the build job is complete the unpacking process begins, which involves the removal of the powder from the chamber and from the part cavities. This powder is then recycled but to do that, the close monitoring of the powder condition is important [44].

After unpacking, the parts are subjected to heat treatment. Parts built by Powder Bed Fusion show high tensile residual stresses after the build, as Mishurova et al. [45] confirmed for INCONEL 718 samples. Therefore, it is usual to perform heat treatments for stress relief (and also to alter material properties) to parts before their removal from the substrate plate because when the part is removed the residual stresses are redistributed in parts on support structure and relaxed in bulk parts, leading to distortions [45].

Once the part is removed from the substrate, usually by sawing or Electric Discharge Machining, the supports are removed, usully with manual tools or by machining if necessary. Mireles et al. [46] investigated the electrochemical dissolution of supports manufactured with INCONEL 718 and this process has been shown feasible. This technique consist on etching the solidified part and supports after the build and before the stress relief heat treatment is applied. To do this, a sensitizing agent (for example, sodium hexacyanoferrate in the case of nickel super-alloys) is applied by immersion. During the heat treatment, the sensitizing agent decomposes and leaves a carbon layer that diffuses into the part (100 to 200 micron thickness) and decreases corrosion resistance of the surface. This "sensitized" region is susceptible to dissolution and is then selectively etched, leaving the component support free and moderately improving surface finish of both interior and exterior surfaces. This technology has been found to have a minimal impact on microstructure and mechanical properties. This process is only worth considering when it is impossible to mechanically remove the supports, in geometries like aerodynamic surfaces (fins and blades) or in internal channels with low accessibility [45].

After the supports are removed, the part may be subjected to Hot Isostatic Pressing to ensure that porosity is eliminated and, finally, operations to improve surface finish like vibration grinding and polishing [44].

2.4.3.1 Evaluation of Part Quality

The final stage of the AM Process is often the quality assessment by analysis of specimens after the build, for example, by performing tensile testing and fatigue testing. As was already mentioned, one main concern in PBF operations is the density of the parts, which can be evaluated by different methods. The Arquimedes method compares the measured global density of the specimen with a reference value for each material. It is a non-destructive and relatively simple and inexpressive process however it does not provide information on morphology and distribution of the pores [47, 48, 49]. Another option is to perform a microscopic analysis of a section of the part. This process provides more information regarding morphology and distribution of the pores, however it is destructive, may not be representative of the full sample and may be influenced by image processing operations and is more expensive [47, 48, 49]. X-ray CT scans are the most sophisticated method to evaluate density and provide the full three dimensional analysis of the pores without destroying the part, nevertheless, this process has size limitations and is, by far, the slowest and most expensive [47, 48, 49].

2.5 Support Structures in LPBF

When processing metals, support structures are needed both to anchor features to the build plate as well as to allow the powder to dissipate heat and prevent distortion caused by thermal stress. These stresses are induced in a body when its volume is not free to expand or contract in response to a thermal gradient, so they appear during the building of a part in PBF in the solidified material and are also found after cool down [50]. Due to the high melting points of

metallic powders, high build-up of focused energy input [51] is necessary. The rapid heating of the metal is followed by a rapid solidification (cooling rates ranging from 10^5 to 10^6 K.s^{-1} [34]) leading to the generation of high thermal gradients in the build chamber [52]. Besides, the thermal conductivity of a metallic powder bed is much lower (approximately 100 times [53]) than that of the solidified metal, thus hindering the conduction of heat along the build direction. This factor induces two types of stresses - during heating and melting, the laser creates tensile stress leading to an expansion and when the part cools down, compressive stresses take place, creating a shrinkage as shown in Figure 2.18.

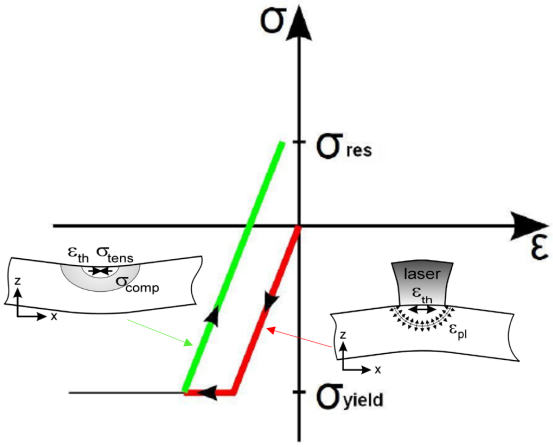

Figure 2.18: Stresses induced by thermal gradients during PBF (adapted from [50])

This phenomenon leads to thermal stresses, buckling and distortion if the appropriate support structures are not used [1, 52]. In some cases, these defects can even cause the whole build job to fail as a consequence of collision of the recoater device with the buckled or de-laminated layers [54]. Examples of delamination of layers and of warping and separation form the supports can be seen in Figure 2.19.

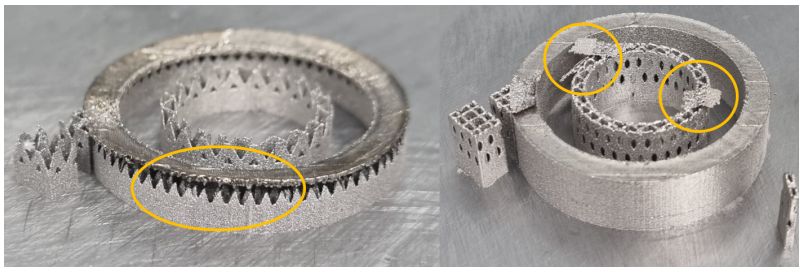

Figure 2.19: Examples of failed build jobs due to separation from supports and delamination

Support structures in LB-PBF have the following critical functions:

- provide regular thermal conduction conditions in the solidification zone, by evacuating heat through the support structure to avoid intense local energy input, which may cause burning

and distortions [55, 52]

- avoid the collapse (anchor) of overhanging structures [55, 52]
- avoid the spreading (distortion) of parts, and avoiding collisions with re-coating system [55]
- facilitate the removal from the substrate plate [52]
- strengthen slender geometries and prevent them from buckling [52]

It is clear that support structures have a vital role in this manufacturing process. However they also bring many complications, firstly, the time-consuming pre-processing tasks such as adaptation to complex geometries during the CAD design. Secondly, material required to build them represent waste and additional costs [56], since they do not belong on the final part. Finally, the post-processing stage requires these structures to be removed, either by hand or by traditional subtractive processes, which leads to increases in lead times and poor surface quality [55].

Strategies in the design of parts and carefully choosing the right build orientation may reduce the need for supports. Although some research has been made in this field, for more complex shapes not completely designed for support elimination, support structures are necessary [56].

So, at least for now, an important aspect of LB-PBF is support structure's optimization, which is the focus of this study. To achieve this, some basic targets and requirements should be met. The most fundamental of all is that these structures shouldn't need supports themselves, which means their geometry should be self-supporting [52]. Their strength should be optimal, because on the one hand too much support material increases their performance but also results in higher material usage, longer build and post processing times. On the other hand, weak supports are easier and quicker to remove, waste less material and make it easier to save unfused powder, but their strength may not be enough to anchor the part and prevent it from distort [52].

Currently, there is a lack of standardized procedures, guidelines and rules of thumb to design supports [56, 54], which means that the pre-processing design options available in commercial software not always provide the desired results and require many iterations and manual alterations based on experience. Since the supports influence the results of the builds so strongly it is crucial to consider their optimization in Design for AM [54]. Some recent research efforts in the optimization of supports related to their geometry and build strategies are documented in the following sections.

2.5.1 Types of supports

The most common types of supports are shown in Figure 2.20. Block support (a) is non-solid and consist of a grid made of thin, usually perforated walls [56]. They have the advantage of being easier to remove but may also lead to entrapped powder. Contour supports (b) are also used for large areas. Point supports (e) are used for very small features, web supports (c) are ideal for circular areas and line supports (f) are suitable for very thin, downward-facing features. Pin supports (d) consist of bulk columns that are not connected to each other and they have higher tensile strength but lower shear strength than block supports [56].

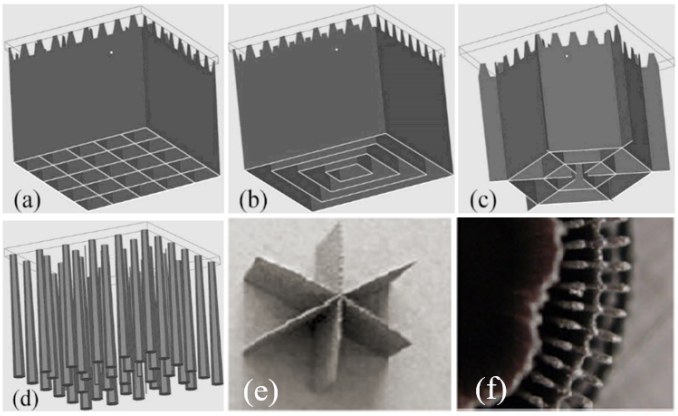

Figure 2.20: Typical support structures (adapted from [57, 58])

In Table 2.1 the importance of the support functions is highlighted and the most suitable supports for each situation are summarized.

Table 2.1: Support Performance (Adapted from [56])

Function	**Consequence of failure**	**Suitable support**
Supporting Overhangs	Overhangs do not build, dross formation (poor surface finish), distortion, delamination	Block supports for surfaces and pin supports for edges
Dissipating heat	Distortion, scorched layer	Pin supports dissipate more heat compared to single scan block supports with perforated walls
Counteracting residual stresses	Distortion, cracks, support detachment, part detachment from substrate	Pin supports (higher strength)

Most supports have two main areas: the main support structure and the teeth, connecting the main support to the part [57]. The teeth are used to facilitate the removal of these structures from the part, however, some challenges may arise if they do not provide enough interface area or if they are too fragile to allow heat dissipation. The main geometric characteristics of the support's teeth are tooth height, tooth base interval, tooth top length and tooth base length, as shown in Figure 2.21. Another important parameter is Z-offset, which is the overlapping between the supports structure and the part and is useful in lower interfaces [59]. An increase in top length and in Z-offset increases strength. In the core, decreasing separation of the grid walls or contours also leads to higher strength. Perforation slightly reduces strength but is useful to save material and retrieve entrapped powders [59].

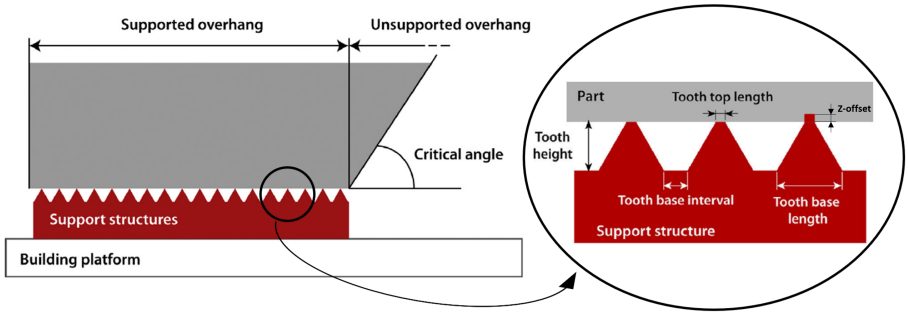

Figure 2.21: Parameters of support teeth (adapted from [57, 59])

The typical specimens that are manufactured to test supports in LB-PBF are cantilever beams like the one shown in Figure 2.22. These represent a critical overhang situation and test the support structure's ability to withstand stress concentration induced by the right angle and warping at the furthest points from the base of the beam. Symmetrical cantilever beams may also be used, with the base pillar at the center and overhanging areas to both sides (T-shaped). Recently, other geometries for support structures have been developed and tested in an effort to obtain optimized structures, when compared to the most common solutions, available in commercial software (Figure 2.20).

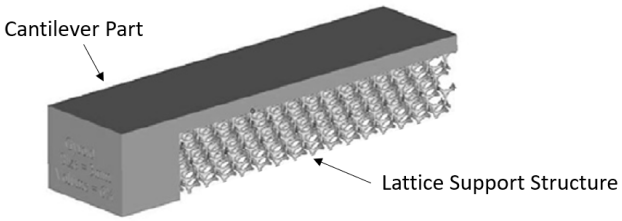

Figure 2.22: Lattice support structure on cantilever beam (adapted from [52])

Lattice Structures and unit cells have been investigated in the last decade. Calignano [57] investigated support optimization in a non-assembly mechanism in aluminium and titanium alloys, considering the influence of the part orientation on the building platform. Different parameters were varied in the geometry of the support such as fragmentation, perforation, Z offset, teeth height, teeth base interval and hatching. It was found that teeth height and hatching had the most influence. Hussein et al. [52] tested the influence of cell size and volume fraction of unit cells in a lattice structure serving as support for a cantilever beam, using gyroid and diamond cell types. It was found that cells with low volume fraction are faster to build and allow saving in material, however they can be too fragile to be used consistently in the manufacturing process. Increased cell sizes lead to the distance between supported points being too large which result in too much of the overhanging area being unsupported. Catchpole-Smith et al. [60] studied the conductivity of triply-periodic minimal surface (TPMS) lattice structures, including gyroid, diamond and Schwartz Primitive and concluded that the thermal conductivity is mainly a function

of the volume fraction - the ratio of solid material to the space inside the lattice, which is filled with unfused metallic powder. Support structures may influence the microstructure development during the LB-PBF process, as Nadammal et al. [61] have concluded for INCONEL 718. Columnar grains of samples built on lattice structure are larger than those of samples built on bulk block supports, due to the lower cooling rates observed on the first configuration.

Tree, Y, inverted-Y supports have been studied and Gan et al. [62] used Finite Element Analysis and experimental data (produced with stainless steel 316L) to evaluate the levelness in thin plates, achieved by three different types of support structures: Y, inverted-Y (Figure 2.23) and uniformly spaced vertical struts (pins). "Y" supports created different cooling rates, which lead to non-uniform heat dissipation between the centre and outer regions of the plate and differential shrinkage on the same layer. Inverted-Y supports showed potential and outperformed Y and pin supports, producing levelled surfaces with only 2.2% contact area. This study also showed other possibilities for support design, like not having to maintain a uniform horizontal cross section and not requiring repeating patterns, like latices. Weber et al. [54] studied tree-like supports (Figure 2.23) and the influence of support characteristics and processing parameters on printability. It was found that scanning speed and laser power were the most influencing machine parameters, while stem and branch diameter and number of branches of the three supports affected the build properties the most out of the design parameters.

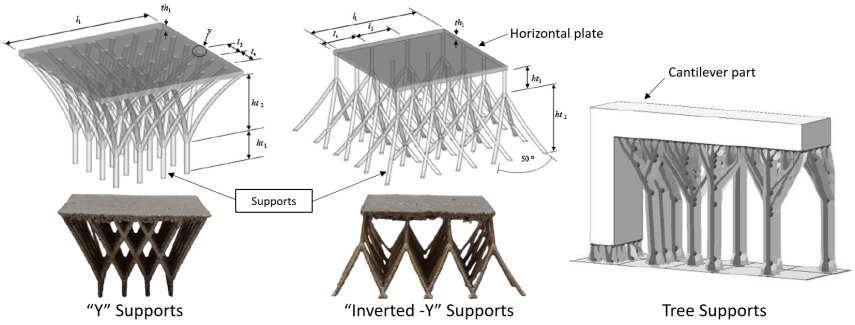

Figure 2.23: Examples of Y, Inverted-Y and Tree supports (adapted from [52, 54])

Non-contact supports are a different type of support structure that was investigated by Cooper et al. [63] using EB-PBF. These are described as "Contact-Free" supports and the main target is to reduce or eliminate post-processing operation, while maintaining their function of improving heat transfer. They are referred to as "heat supports" and consist of an additional part, like an independent block that is built up to a certain gap (corresponding to a few layers, less than 1 mm) to the overhanging feature (Figure 2.24). This novel concept may represent a possible alternative to conventional supports in powder-based metal AM although their effectiveness is dependent on the heat support thickness and the gap between the support and the part. Another limitation may occur in the manufacturing of long overhangs, which may still require anchors to reduce warping.

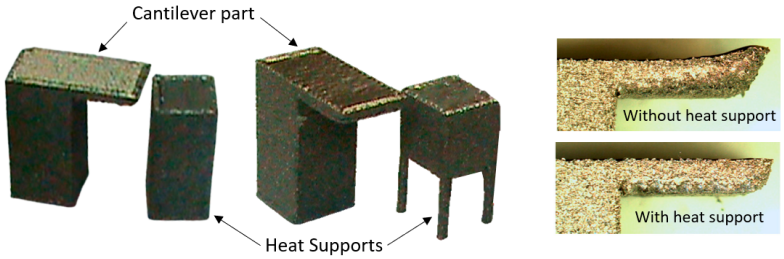

Figure 2.24: Examples of contact-free heat supports (adapted from [63])

2.5.2 Processing strategies

Besides optimizing the geometry of supports structures, some investigation has also been done toward the development of more accurate and complete models for numeric simulation. The quality and effectiveness of the supports and, consequently, the build job, can be highly influenced by the processing parameters of the machine during the process. It is common to use different sets of parameters to build the supports from the ones used to build the main part [64].

Kruth et al. [50] developed the Bridge Curvature Method (BCM) and studied the influence of machine and scanning parameters on the reduction of thermal stresses and it was concluded that changes that reduce the thermal gradients also lead to reduction of stresses and consequent strain. Tests on Ti-6Al-4V showed that a reduction of the length of the scan vectors reduced the angle of warping by 13% after the overhang parts were removed from the substrate. Shorter scan vectors are subjected to a smaller temperature gradient due to the higher remaining heat of the previous vector. The orientation of the scan vectors also influences thermal stresses, which are lower in the direction perpendicular to the vectors than in the parallel one. Therefore, to minimize distortions, the scan vectors should be oriented in the direction of higher stiffness of the part so that it has the capacity to withstand the larger thermal load [50].

Another strategy that proved effective for Ti-6Al-4V was the preheating of the base plate to 180ºC, reducing warping by 10% [50]. This behaviour was also confirmed by Buchbinder et al. [51] in the production of twin cantilever parts in AlSi10Mg after pre-heating the base plate up to 200ºC and 250ºC. Although this strategy reduced hardness due to microstructure coarsening, this property still registered acceptable values. Pre-heating initiates the creeping process and reduces distortions after separation from the substrate. It also prevents cracks induced by thermal stresses, has the potential to reduce the amount of supports required and the stress relieving annealing heat treatment operations, making PBF more repeatable with fewer post-processing operations [51].

Jhabvala et al. [55] proposed a more productive method for building parts, which combines pulsed and continuous laser modes of radiation. The continuous one is used to build the actual part and ensure the requirements of good mechanical properties, while pulsed radiations are used to produce the supports. The support structures originated show sufficient strength to hold the part and dissipate the heat but they become easier to remove. Furthermore, this strategy is a lot more productive because the pulsed radiation allows very high scanning speeds [55].

2.5.3 Numerical Simulation

To better understand and predict the complex evolution that materials undergo during the PBF process, there has been effort in numerical simulation solutions. Research has been developed to evaluate the effective conductivity of supports in PBF by using numerical simulation. Zebg et al. [64] studied a Representative Volume Element of a block support, with solid walls and entrapped powder. The theories of homogenization and periodic boundary conditions were applied to the thermal behaviour of the support in a temperature independent and in a dependent (non-linear) scenario. The effective thermal properties of the block supports structure were found to be a function of geometry, anisotropy and independent thermal properties of constituents [64].

Huang et al. [53] used topology optimization in a design space equivalent to the volume under the overhang, to achieve improved support structures. The objective function was to maximize thermal conduction with a periodic lattice constrain and assuming equal temperature in all contact points between the support and the overhanging horizontal feature. The heat transfer mechanism was considered to be only conduction, neglecting radiation and convection, and the supports were treated as a isotropic conductive material. The simulations resulted in a lattice structure that was then manufactured and its performance compared to other supports, namely pins, walls and inverted-Y. Two directions relative to the scraper moving direction were evaluated. The optimized lattice structure showed the highest performance (lowest distortions) due to its enhanced heat conduction and overall stiffness.

Andreotta et al. [65] modeled the problem by incorporating a set of Navier-Stokes equations in addition to the energy balance to simulate both fluid flow (considering temperature dependent dynamic viscosity) and thermal transport. Their simulation of the Marangoni convection effect within the melt pool mitigates the need to theoretically derive the effective thermal properties, as was done in other studies [64]. The results were experimentally validated on INCONEL 718.

Currently there are also simulation modules embedded in commercial software for AM. These type of simulations are usually conducted after the creation of a voxel mesh, which can be defined as a stack of small cubes (ideally, as small as possible) encapsulating the outer surface of the parts. Some of the most widely used solutions are described next:

Materialise Magics offers a simulation package that facilitates the prediction of risks of recoater contact, risk of support failure or warping, distortion compensation and overheating. MSC Simufact uses hexahedral elements for a voxel mesh and has been developed to simulate the PBF process, considering the type of machine as an input. Other necessary inputs are element size, hatch spacing, scan speed, laser power, preheat temperature, layer thickness and scan strategy [66, 67].

Both of these tools require an initial calibration, which must be performed for a specific scanning strategy, material and set of parameters. The main steps of the calibration are:

1. Designing of 3 cantilever beams in 3 different directions, to define inherent strains

2. Printing without heat treatment

3. Support removal

4. Measuring the deformation by the software.

This calibration is based on reverse engineering and in the Inherent Strain Theory, since it uses the measured deformation to compute the inherent strain. This method reduces model complexity because it avoids the thermal time-dependent analysis - considers the problem as mechanical, with a thermal load instead of tracking the entire thermal-mechanical history [68, 69]. A voxel size of 1mm is recommended for calibration and the simulation should be performed for a voxel size of the same order of magnitude as the respective calibration. MSC Simufact optimizes calibration through the Least Squares Method.

Important concerns while using these type of software include using an appropriate voxel length in order to obtain accurate result. Additionally, when a simulation considers the phase of removing the part from the substrate, shape comparison should be performed, instead of the total displacement which would be influenced by rigid body movement and lead to incorrect interpretation.

Ansys has released Ansys Additive Suite, where voxel and tethraedal meshes can be applied. This software requires more inputs than Simufact, however, it has presented more precise results in comparison to experimental values [70].

Even though a lot of research has been done in the field of support optimization, it is still important to define design guidelines so that they are easily and quickly added to different geometries in an industrial environment with high demand. Ready-to-use options are becoming increasingly available, nevertheless, larger build plates and budget limitations still pose a challenge to a more systematic utilization.

Chapter 3

Experimental and Numerical details

This chapter reports the experimental methods developed and implemented during this dissertation. First the definition of the problem is clarified as the evaluation of a support's strength, with the goal of optimizing these structures to withstand the stresses caused by the manufacture of a part over them. An experimental method was created and it consisted in the design of a tensile specimen, so that the response variable of the design of experiments is the rupture force of the support structures. These tensile specimens were manufactured using the AddCreator-AC210 LB-PFB available in Adira's facilities. There was a first build job attempt that failed due to a recoater contact with a part. Therefore, the final parameters were adjusted to prevent similar situations in the second build job. The specimens were tested in terms of strength using a quasi-static tensile test and in terms of density, by microscopic analysis. Finite Element Simulations were obtained as a comparison method in order to obtain a reference value for the experimental tensile strength.

3.1 Machine characteristics and setup

During the experimental work proposed in this research, the machine used was the LPBF equipment introduced in Section 2.4. The main machine characteristics are presented in Table 3.1 and the power curve of the lasers is given by a linear relation, presented in tabular form in Table 3.2. Other vital peripheral systems of the machine are the Volkmann® powder systems and the inert gas input systems. The powder systems are responsible for powder distribution and re-circulation of the excess of each layer (sieving). The gas systems enable the control of the atmosphere properties inside the process head chamber. This is usually achieved by two gas fluxes - a main flow and a secondary bypass flow.

It is important to point out that, although the build envelope is 1020 x 1020 x 500 mm, it is also possible to build on smaller substrate plates, in order to reduce powder consumption and operating time for smaller parts. For the build job executed in the scope of this experimental process, a substrate equivalent to one third of the machine's build envelope capacity was used, therefore the

Table 3.1: AddCreator-AC210 characteristics

Dimensions	
Build Envelope	1020 x 1020 x 500 mm
Overall Dimensions	8000 x 8500 x 4000 mm
Chamber Scan field Size	430 x 100 mm
Process	
Max. Scan Speed	9 m/s
Average Gas Consumption	50 l/min
Layer Thickness	$20-100\ \mu$m
Geometric Tolerances	$100\ \mu$m
Positioning Tolerance (X,Y,W)	$50\ \mu$m
Alloys	Stainless steel, Maraging steel, Nickel based alloys
Laser	
Laser Type	Fibre
Focus Diameter	$95+/-10\ \mu$m
Power	5x 400 W
Configuration	5 laser sources and 5 scanners

available build area was 1010 x 333 mm. The available height was not changed, however, there is an interest in having this dimension as reduced as possible, for the aforementioned reasons.

The parts were designed using SOLIDWORKS 2021® and the pre-processing and build preparation of the samples was performed using Materialise Magics® version 24.0 1 and the integrated build processor AdiraMultiscan. As was already discussed in Chapter 2, the supports play a vital role in the LPBF process and their failure may cause the whole build job to fail. Therefore it is extremely important to understand the influence that process parameters have on their performance.

Table 3.2: Power curve of laser of AddCreator-AC210 machine

Power [%]	Theorical Power [W]
0	0
10	40
20	80
30	120
40	160
50	200
60	240
70	280
80	320
90	360
100	400

3.2 Materials

The material used in this study was the austenitic stainless steel SS316L powder, due to the lack of know-how on specific processing parameters for building supports on this material. The powder morphology was spherical with a volume fraction of 20-53 μm. The particle size distribution and the physical data are included in Tables 3.3 and 3.4. The technical specifications of the powder used for the specimens are presented in Appendix A. For this build job, no sieving was used, and the initial powder quantity in the reservoir was 230 kg of new powder.

Table 3.3: Particle size distribution

Particle size	$< 15\ \mu$m	$> 15\ \mu$m and $< 45\ \mu$m	$> 45\ \mu$m
Particle percentage	1.32 %	96.49 %	2.19 %

Table 3.4: Physical data

Filling density	Flow time (ϕ 5 mm)
4,30 g/cm^3	3,1 s/50 g

During the production, the protection gas used was nitrogen and with its input into the process head, there was a target of keeping oxygen content bellow 2000 ppm (only using the main gas flow, bypass flow was inactive). To achieve this, the total flux of gas was kept at the approximately constant value of 50 l/min.

3.3 Description of methods and experimental approach

In order to conduct the experiments to optimize support structures, the main goal would be to optimize the strength of the supports. It was possible to verify, in previous parts made with AddCreator-AC210, that if the supports are too fragile the part may detach from them, causing warpage and distortion (visible in the toothed support in Figure 2.19 left). On the other hand, stronger supports are harder to remove and may cause the necessity for machining operations, hindering lead time and increasing cost of the part (visible in the solid bulk in Figure 2.19 right). Therefore, an experimental programme was designed aiming at understanding the influence of different factors on the supports' strength and find the combination of the parameters that lead to the most balanced support structure.

The steps to develop the experimental procedure are organized in figure 3.1 and are discussed in a fully detailed manner in the following subsections.

3.3.1 Development of a new methodology and design of the test specimen

To study the strength of support structures in LPBF, firstly there was a need to develop an experimental methodology, due to the lack of a standardized procedure and guidelines in the literature. Initially, using a cantilever specimen was considered, however two challenges soon arose

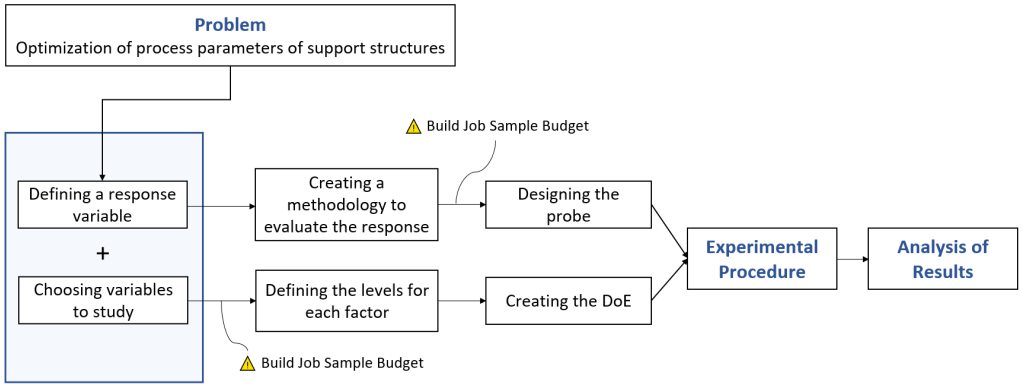

Figure 3.1: Description of steps in the experimental procedure

when developing a strategy for a part such as the one represented in Figure 2.22. Firstly, it was very likely that some of the samples would fail and that would be critical for the machine if large distortion would occur at the end of the overhanging feature. Due to the technology of a movable process head, a small gap of approximately 1 mm is maintained between the powder bed and the process head. If some sample were to show large deflection it could collide with the recoater and with the process head, which would not only cause the build job to stop but could also damage the main component of the machine. Another challenge arose when the design of experiments began. The first step was to set the response variable of this experimental analysis, and to evaluate this type of part there seemed to be room only for a qualitative analysis, which fell short of the initial goal. These reasons lead to the necessity of creating a quantitative methodology to evaluate the support as well as to the design of an appropriate specimen.

With the goal to find supports that were removable using only simple tools such as pliers, but also strong enough to anchor the parts down, it was decided to create a methodology where the response variable in analysis is the tensile rupture force, F_{rupt}, of the interface between a support and a solid body. Hence, in a first iteration, a cylindrical tensile specimen was designed, containing one support structure in its mid plane. However, since this was not not a standardized specimen, different types of fixture to the tensile test machine were studied. Some important concerns when designing specimens in this LPBF process are: reducing height as much as possible, simplifying removal from substrate, avoiding overhangs and facilitating powder removal.

In Table 3.5 the main options are presented, as well as some strengths and limitations of each design. The first option was to build the part with two horizontal through holes, one below and another on top of the support. These would be used for gripping to the testing machine trough pins, which would entail the manufacturing of adaptor parts to connect these pins to the threaded connections on the machine. It would also be necessary to perform some simple finishing operations on the holes because in AM it would be better to make them drop-shaped to avoid overhangs. However, it was not practical to create a new set up and a new type of fixture for the available machine.

To overcome this difficulty, another design option was to use a threaded connection between

Table 3.5: Trade-off of different probes for supports testing

Criteria	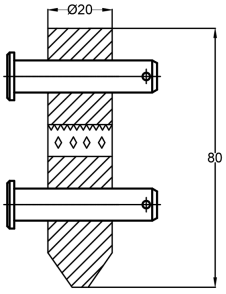	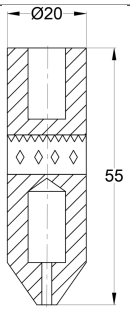	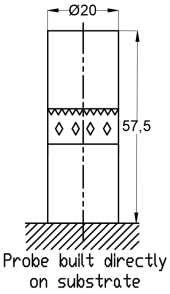
Description	Two horizontal through holes and fixation with pins	Two blind holes for threaded connection	Either of the previous scenarios without the cone-shaped base: 2 horizontal holes for pin connection or two threaded holes
Height	80 mm	65 mm	57.5 mm
Post-process operations	1-Cleaning; 2-Cutting cone-shaped base; 3-Finishing the horizontal holes	1-Cleaning; 2-Cutting cone-shaped based; 3-Making threads on the blind holes	1-Cleaning; 2-Shipment of large substrate and removal from the substrate Wire-EDM by third-party entities; 3-Performing either of previous nr 3 operations.
Extra parts	2 x pins and 2 x adaptor for pin connection with the specimen and threaded connection with the machine	2 x studs	Either of the previous options: 2 x pins and 2 x adaptors or 2 x studs

the specimen and the machine, because that is the compatible with the current machine testing setup and would require less adaptation. However, to make external threads on the specimen itself would require turning of all the specimens in both ends and this operation would be time consuming and made more difficult by the limitation that the part could not be clamped on a lathe in the support zone. Therefore, instead of machining external thread on the specimens, it was decided to make blind holes in AM, which are later threaded manually, avoiding stresses on the support before the tensile test.

Then, 2 studs were designed and manufactured in PM300 steel to make the connection between the threaded hole of the specimen and the threaded hole of the machine fixture set-up. The design was created for specimens with a nominal diameter of 20 mm. The verification of the 12 mm stud was done through Equations 3.2-3.3. The most critical load on the stud would be reached for case the larger teeth top length, which was defined as 400 μm (more information on this is found in Subsection 3.3.2). In this case, the contact area between the teeth and the solid body is approximately 33 mm^2. The ultimate tensile strength of the specimens was considered 574 MPa, which is the reference value pointed by the manufacturer, according to Appendix A, and

was verified to be a conservative value in comparison to the values found in other studies [39]. As for the characteristics of PM300, a minimum hardness value of 292 HV and carbon content under 0.55% were considered, according to the technical specifications [71]. This lead to the classification of the material in class 6.8 and the values R_m and $R_{p0.2}$ were computed accordingly [72]:

$$\begin{aligned} A_{contact} &\approx 34 \quad mm^2 \\ \sigma_{uts} &= 574 \quad MPa \\ F_{rupt} = \sigma_{uts} * A_{contact} \Rightarrow F_{rupt} &\approx 20 \quad kN \end{aligned} \tag{3.1}$$

$$\begin{aligned} \text{Thread pitch} : p &= 1.25 \quad mm \\ \text{Thread nominal diameter} : d &= 12 \quad mm \\ A_s = \frac{1}{4} * \pi * (d - 0.935 * p)^2 \Rightarrow A_s &= 92.14 \quad mm^2 \end{aligned} \tag{3.2}$$

$$\begin{aligned} R_m = 6 * 100 \Rightarrow R_m &= 600 \quad MPa \\ R_{p0.2} = \frac{8}{10} * R_m \Rightarrow R_{p0.2} &= 480 \quad MPa \\ F_{allowable} = R_{p0.2} * A_s \Rightarrow F_{allowable} &= 44.2 \quad kN \\ \text{Safety factor} : n = \frac{F_{allowable}}{F_{rupt}} \Rightarrow n &= 2.3 \end{aligned} \tag{3.3}$$

The technical drawing of the studs is shown in Figure 3.2. This design was chosen due to a better compromise between the number of post processing operations and the need for new extra parts.

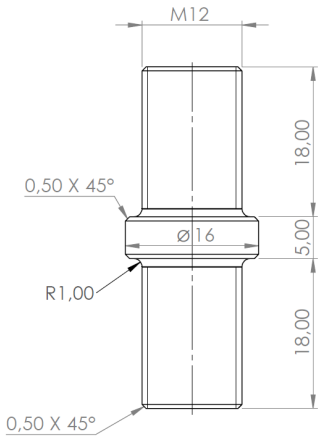

Figure 3.2: Technical drawing of studs

Finally, one important feature of the part is the cone-shaped base, which could have been incorporated on either one of the designs, and allows for the manual removal (aided by simple tools) from the substrate plate. This detail is designed in a 55º angle (features are expected to be self-supporting at angles higher than 45º). Although this detail adds approximately 10 mm in

height, it also provides time savings in post processing because otherwise it would be necessary to ship the whole substrate with all the parts to some external entity that could perform wire-EDM to remove all the specimens. Thus, cost and lead time are reduced by opting for the cone-shaped base. The drawing of the selected probe part is shown in Figure 3.3 and the 10 mm gap between the two solid bodies is where the support structure is built. A vertical through hole with a diameter of 2.5 mm was included to allow for the powder removal from the hole on the lower half of the specimen. Otherwise, the powder would be entrapped here and would be released when cutting the conical end, which could represent a health hazard as well as damage some systems of the testing machines.

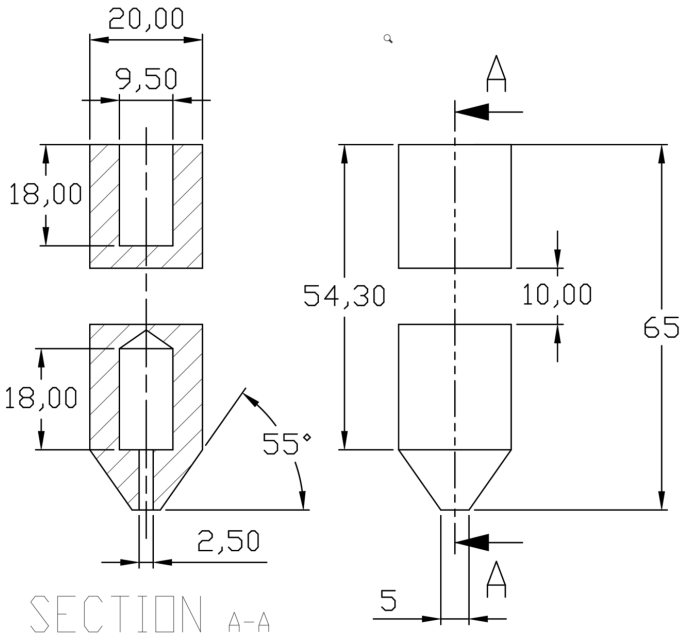

Figure 3.3: Technical drawing of selected test specimen

3.3.2 Design of Experiments - definition of factors and levels

After creating a methodology for support evaluation, the next step was the selection of parameters to study. It was decided that different types of parameters should be evaluated - geometrical, laser-related and scan-related parameters. The last two were quickly chosen - *laser power* and *scan speed*, which are the most fundamental factors of the process. These parameters were varied only in the supports structure while the rest of the specimens' parameters were the same for all samples. Within the support structure, the contour ad hatch parameters are the same.

Of all the possible types of supports shown in Figure 2.20, a very commonly used type is the block support due to its versatility and customization. Therefore, it was chosen as the target of the optimization. Its main geometrical parameters are given in Table 3.6.

Table 3.6: Main geometric parameters available for Block Supports (adapted from [73, 74])

Parameter	**Information and Guidelines**	**Used Values**
Type	Block type uniformly distributes load, ideal for large areas. Most versatile type.	Block
X-Y offset	"Define the distance between the edge of the part and the border of the support."	0.1 mm
Z-offset	"Define the distance between the top and/or the bottom of the support and their respective surfaces. Positive values ensure the support penetrates the part." Recommended to properly connect the support to the part, due to an increase in the strength of the connection.	variable in DoE
No support offset	"A (more or less vertical) wall gives support to another surface ; in this case, no support needs to be generated for very small overhangs. Define the distance up till a overhang is self-supporting and the minimum height for a wall to be considered a supporting wall." 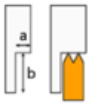	a=2; b=0.5
Vertical wall offset	"In case support is generated beside a vertical wall, ensure a distance is kept between the vertical wall and the support being attached to the vertical wall and, consequently, unnecessary difficulties and marks on the part when removing the support."	0 mm
Lowest line	"Automatically generate an extra line of support to ensure the lowest line of the surface is supported."	OFF
Local minima	"Adjust hatching: Move the hatching intersection to support the local minima (the lowest point of the part). Add point support: Add a point support to support the local minima (the lowest point of the part). When needed, rotate the point to match the hatching rotation." The addition of a pin support within the block is useful to increase strength	Adjust hatching ON
Broaden support	"Create a step-like base at the support bottom to increase its size and create a stronger connection with the platform."	OFF
Reinforcement line	"A reinforcement line is a line support that is manually drawn to reinforce an existing support that may be too fragile to stand on its own. To sue this function, select 'Draw reinforcement line' found in 2D edit tools."	OFF
Solid border	"A border will connect supports that otherwise would be loosely connected. It is used mostly for small supports with large teeth in comparison to the rest of the support. "	ON
Teeth synchronization	"Synchronize upper and lower teeth according to each other."	OFF

Support length	"Connect to platform: Automatically adapt the length of the support to reach the platform. Fixed length: Manually customize the length of the support by defining a fixed length. This is particularly useful for EBM (Electron beam melting) technology." In LPBF, the "connected to platform" option should be used.	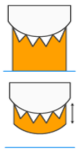	Connected to Platform
Thickness	Thickness of support walls. It influences their strength		0.4mm
Hatching	"Block supports are made of a grid of X and V lines, called hatching. Define the distance between these lines and the rotation angle around the Z axis." Reduction of a and b increases strength; these values should be larger than 0.5mm.		a=b= 2mm
Hatching/Border teeth	"To facilitate the removal of the support, support can be equipped with teeth profiles on the top and/or on the bottom." Higher b values increase strength; b should be larger than 0.1 mm. Lower teeth are not recommended to make the connection to the platform; when they are used, Their length (b) should be larger than 0.4mm, or approximately twice as large as the b value of upper teeth.		a=1.5; b=variable on DoE; c=1.5; d=0.2
Hatching/Border teeth breakpoint	"Create breakpoints on teeth to break the support on these points and easily remove it. Note: X value corresponds to the Top length parameter defined in Teeth page."		a=b=x=0mm
Teeth walls syncronization	"No synchronization: No synchronization method is defined when teeth of X and Y hatching intersect each other. Teeth intersection: Teeth of X and Y hatching intersect each other right in the middle. No intersection: Teeth of X and Y hatching never intersect each other. "		No synchronization
Fragmentation	"To facilitate the removal of the support, create gaps in the hatching by selecting fragmentation option."		OFF
Fragmentation at crossing	"To facilitate the removal of the support, create gaps at crossing points of X an Y hatching by selecting fragmentation at crossing."		OFF
Hatch removal	"In some cases it might happen that very small hatches are created close to the support border. Remove the hatches that are closer to the border than the defined minimum distance and have an angle with the border smaller than the defined minimum angle."		OFF
Borders	"Draw borders: The borders of the support will be reinforced with an additional contour wall. Fragmentate borders: To facilitate the removal of the support, create gaps in the support border."		Draw Borders ON

Border thickness	Thickness of border walls		0.4mm
Perforations	"Diamond: To simplify the removal of the not processed material and increase savings, perforate the support with the self-supporting diamond shape. Rectangular: To simplify the removal of the not processed 1 d material and increase savings, perforate the support with the rectangular shape." Diamond perforations are self-supporting, which is an advantage. They reduce strength slightly; a should be larger than 0.2 mm (a may be equal to the tooth top length).		Diamond. a=1.2 mm b=60º c=2.0 mm d=2.0 mm
Unperforated borders	"Do not perforate borders: To strengthen the support, the additional contour wall is not perforated. Do not perforate hatching: To strengthen the support, the outer side of the hatching is not perforated for the defined distance."		OFF
Gusset border	"Create a gusset border to decrease te size of the block support. The gusset support will be attached to the surface and the block support."		OFF

It was decided to only include upper teeth on the support, because the goal was to simulate the base supports that connects parts to the substrate and they do not normally present lower teeth. Perforation of supports was used to facilitate powder removal from inside the grid of the block support after manufacturing. It is important to highlight the large quantity of options to customize supports in Materialise Magics®, which would be impossible to fully explore due to the limitations in time, space and budget of the build job. Therefore, two main geometric parameters were chosen. The first was the *tooth top length*, which determines the length of the connecting lines in the interface of the support with the part, and had determined the failure of previous build jobs. The second was the *z-offset*, which is the height after the interface during which the laser will continue to scan the tooth's profile. This last parameter has been recommended as a solution to avoid failure of build jobs due to distortion, however, this recommendation had been based on experience, and the little know-how on the effect of this feature made it relevant to be investigated.

To define the design of experiments, it was decided to vary laser power and scan speed on three levels each, so that it would be possible to detect non-linear trends. The geometrical parameters of the support's teeth were only tested on two levels because their influence on the support's strength was predicted to be linear. Thus, in order to obtain the most complete information as possible, a full factorial design was created with 36 tests, as is shown in Table 3.7. This table shows the improved parameters that were used in the final specimens, in the successful build job. These parameters resulted already from the experience of a preliminary failed build job. The choice of these values is explained in Section 3.3.2.1.

Table 3.7: Final DoE of the support region of the specimens - factors and levels (full factorial)

Parameter	**Levels**
Scanning speed, v_S [mm/s]	900 1150 1400
Laser Power,P_L [W,%]	260, 65% 300, 75% 340, 85%
Tooth top length, ttl [mm/s]	150 μm 400 μm
z-offset, z [nr of layers]	0 7
Number of test specimens	3*3*2*2 = 36

All the combinations of the full factorial design of experiments are shown in Table 3.8.

Table 3.8: Final DoE combinations of support specimens' parameters

Specimen ID	ttl [μm]	z [nr of layers]	v_S [mm/s]	P_L[W]	P_L[%]	Volumetric energy density [J/mm^3]
1	150	0	900	300	75	66.67
2	150	0	1400	260	65	37.14
3	400	0	1150	300	75	52.17
4	400	7	1150	300	75	52.17
5	400	7	900	260	65	57.78
6	150	0	1400	340	85	48.57
7	150	0	900	260	65	57.78
8	150	7	1400	300	75	42.86
9	400	7	1500	260	65	34.67
10	400	7	1400	340	85	48.57
11	400	7	1400	300	75	42.86
12	150	7	1150	260	65	45.22
13	400	7	900	300	75	66.67
14	150	0	1150	340	85	59.13
15	400	0	900	300	75	66.67
16	150	7	900	300	75	66.67
17	150	7	1400	260	65	37.14
18	400	0	900	260	65	57.78
19	150	7	900	260	65	57.78
20	150	0	1150	260	65	45.22
21	400	0	1400	260	65	37.14
22	400	0	1400	340	85	48.57
23	150	7	900	340	85	75.56
24	150	0	1150	300	75	52.17
25	150	7	1150	300	75	52.17
26	400	0	1150	260	65	45.22

27	400	0	1150	340	85	59.13
28	150	0	1400	300	75	42.86
29	400	0	900	340	85	75.56
30	400	7	1150	260	65	45.22
31	150	0	900	340	85	75.56
32	400	0	1400	300	75	42.86
33	400	7	1150	340	85	59.13
34	150	7	1400	340	85	48.57
35	150	7	1150	340	85	59.13
36	400	7	900	340	85	75.56

To easily identify the types of specimens, in regard to their geometry, the following nomenclature of support's geometry is adopted (Table 3.9):

Table 3.9: Classification of specimens according to the support geometry

Support Geometry	ttl [μm]	z-offset [nr. layers]
A	150	0
B	400	0
C	400	7
D	150	7

As for the remaining process parameters, layer thickness was set at 50 μm and the hatch distance at 0.1 mm. While the laser power and scan speed used in the supports were already mentioned and included in the DoE, for the rest of the body, the values are summarized in Table 3.10. These values were adopted due to a previously successful part built accordingly, in 316L. The hatch and contour parameters being the same was one of the decisions made from the failed build job, as it will be further explained in section 3.3.2.1.

Table 3.10: Final scanning parameters used in the solid parts of the support specimens

Scanning Profile	P_L [W]	v_S [mm/s
Hatch	300	1300
Contour	300	1300

Additionally, aiming at evaluating relative density of the supports, 9 density specimens were also built varying only the scanning parameters. The goal of these parts was the correlation between the support density and its rupture strength. The geometry is shown in Figure 3.4 and the combination of parameters is detailed in Table 3.11. Both in the support specimens and in the density specimens, the contour processing profile adopted had the same scan speed and power as the hatch.

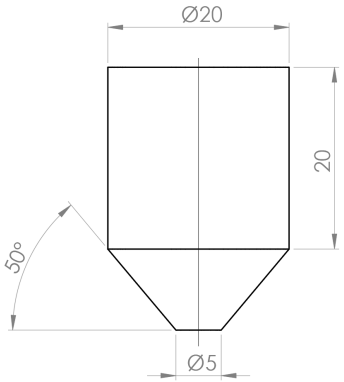

Figure 3.4: Technical drawing of density specimens

3.3.2.1 Failure report of the first build job

The parameters presented above were the ones used in the final iteration of the DoE, and they were used to produce the specimens. However, they resulted from the experience with a failed attempt of a a build job. This failure occurred when the parameter described in Appendix B were used. The build job was estimated to run for 1334 layers, lasting 22 hours and 10 minutes. The process was started and lasted for approximately 2 hours and 30 minutes. However, there was an unplanned stop after this time, at layer 157 (7.85 mm), caused by a damage on the recoater, which unlevelled the powder bed making it impossible to restart from this point. Next, this event is reported in more detail and the decision on the parameters presented in Tables 3.7, 3.8 and 3.10 is explained.

The recoater is made of a solid metallic body in which there is a groove. Here, a silicone band is assembled. This material can withstand very small and blunt edges on the powder bed by being slightly deformed. However, during the build job, in one specimen (ID: 6), a sharp edge began to rise and deform, which caused the silicone lip to detach from the recoater. This lead to an uneven recoater surface which damaged the powder bed that had been formed until that point (Figures 3.5 and 3.6) and the processed stopped automatically.

It was verified that other specimens started to show similar deformation and smaller defects like dents started to appear in other areas of the silicone lip. For example, in specimen 10 (Figure 3.7) there was an edge displacement of 860.35 μm which is quite large, considering the layer thickness of 50 μm.

Table 3.11: Definitive DoE combinations of density specimens

Specimen ID	v [mm/s]	P_L[W]	P_L[%]	Volumetric energy density [J/mm^3]
37	1150	260	65.00	45.22
38	1150	300	75.00	52.17
39	900	340	85.00	75.56
40	1400	340	85.00	48.57
41	1400	260	65.00	37.14
42	900	300	75.00	66.67
43	1150	340	85.00	59.13
44	1400	300	75.00	42.86
45	900	260	65.00	57.78

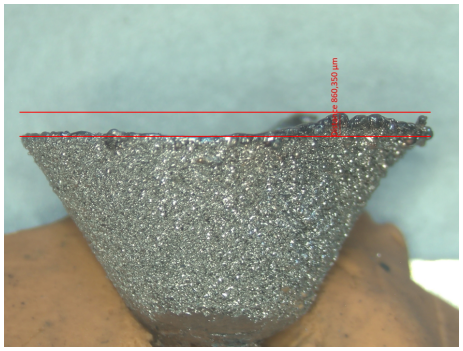

Figure 3.7: Lifted edge of specimen 10

Another important observation was that while many of the support specimens showed this type of behaviour, none of the density samples did, as can be seen in Figure 3.8. The main difference between the two types of parts is that the density specimens were built using the contour parameters equal to the hatch ones, while the support specimens were built using a set of parameters with higher energy at the contour (180 W; 300 mm/s). It was concluded that the energy may have been

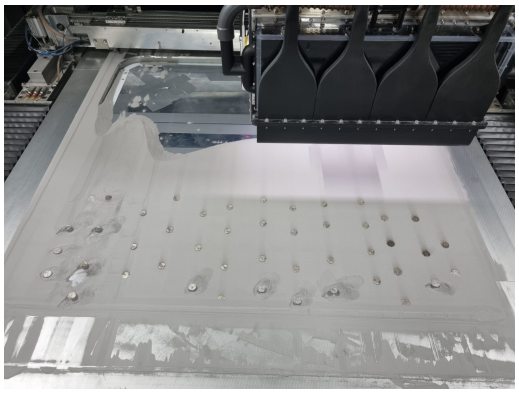

Figure 3.5: Damaged powder bed

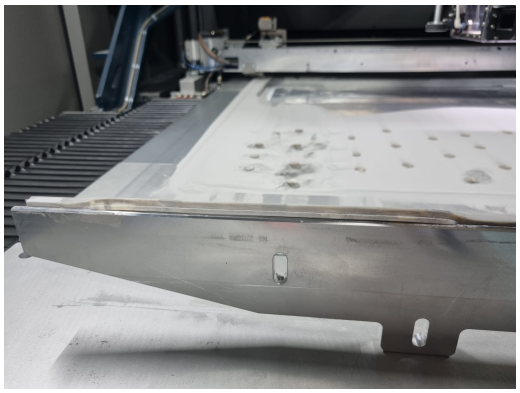

Figure 3.6: Damaged recoater

to high on the contour scanning profile (surface energy density of 12 J/mm^2) provided. Since this was suspected to be the main cause of the edge warping, the first mitigation decision was to use hatch parameters on the contour for all specimens instead of only the density ones.

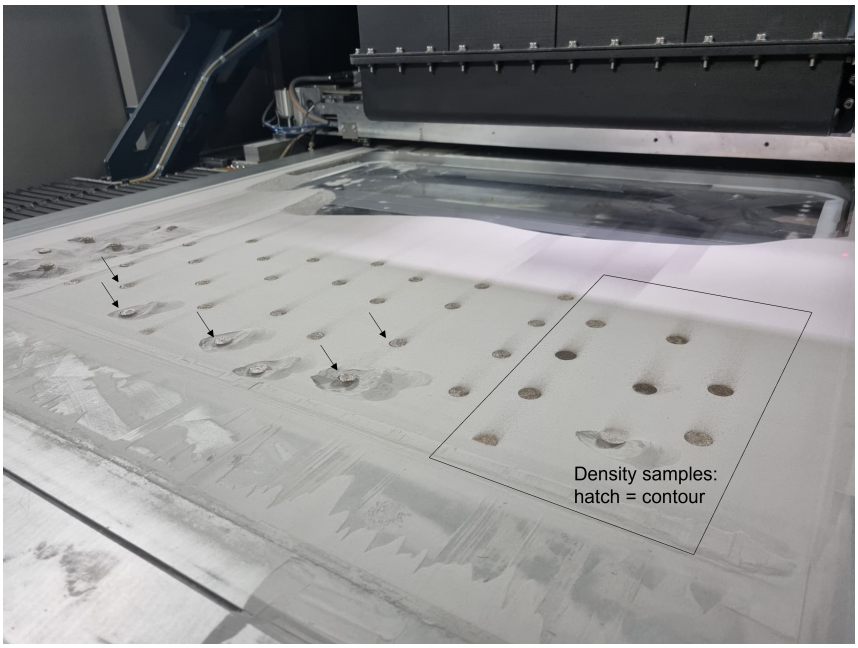

Figure 3.8: Difference between lifted edges of the support specimens and the defect free density samples

A second observation was the poor quality of some specimens, which were becoming very dark instead of showing the desired clear, bright and smooth surface. The laser seemed to leave longer trails of condensate fumes after processing these samples with worst quality. By observation of the density samples, which showed all the different scan speed-laser power combinations, it was possible to verify that the three specimens showing worst quality corresponded to the three combinations of parameters where the scanning speed was 700 mm/s, which lead to the highest volumetric energy density values. On the other hand, the two samples showing the best quality referred to the combination of parameters that lead to lowest energy density, as is explained in Figure 3.9. This lead to another alteration decision to implement in the second build job - increasing the scanning speeds of the DoE in all specimens in order to decrease the energy input (Equation 2.1). The maximum value of volumetric energy density was, thus, lowered from 97.14 J/mm^3 to 75.56 J/mm^3.

Finally, in an attempt to reduce the risk of failure in other parts of the second build job in later layers, the geometry of the density specimens was slightly changed. The internal angle of the end of the inferior hole was changed from 45º to 55º (the same as the inferior cone). This lead to an addition of 35 layers.

With all the observations and conclusions taken from the first attempt at the build job, mitigation actions were adopted and led to the final definition of the parameters that were presented

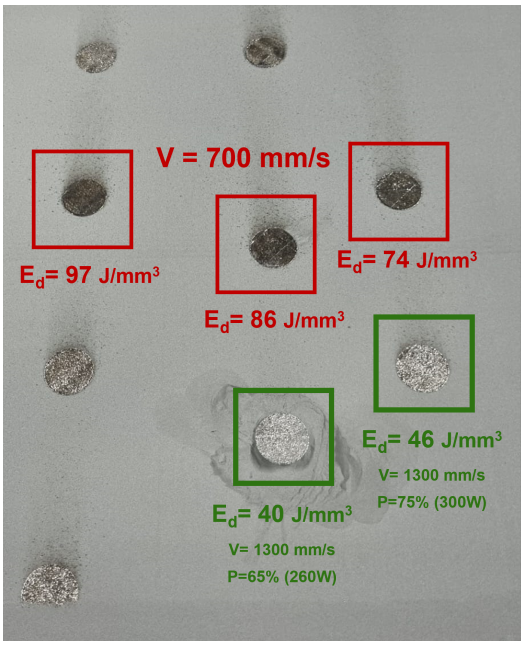

Figure 3.9: Difference between density samples - worst quality achieved with 700 mm/s.

in the previous section (Tables 3.7, 3.8, 3.11). The decisions for the choice of parameters are the following:

1. Using equal parameters on the contour and hatch parameters in all specimens;

2. Increasing velocity in all profiles to lower energy density and avoid the 700 mm/s, which seamed to be the most problematic (700; 1000 and 1300 replaced with 900; 1150 and 1400 [mm/s] respectively);

3. Changing the internal angle from 45º to 55º to prevent another failure later in the build.

After the failure of the first build job, and the previously mitigation actions were adopted, a new build job was started according to the parameters of Tables 3.8 and 3.11. The build job lasted for 28 hours, resulting in 1369 layers. The final substrate with all the parts after the removal from the powder bed is shown in Figure 3.10. During the build process, sample 44 was removed because there was a misalignment between the substrate plate and the first layers of the part, which cause it to tilt. Since this represented a danger to the recoater and the build job, the specimen was removed to avoid a failure such as in the first build job. Specimen 45 is not shown in the figure because due to a similar problem, its base separated from the substrate during the vacuuming operation. However it was built successfully, regardless of poor surface quality. Finally, after vacuuming the build space and removing the substrate from the machine, the samples were successfully removed, using only a locking pliers, as intended.

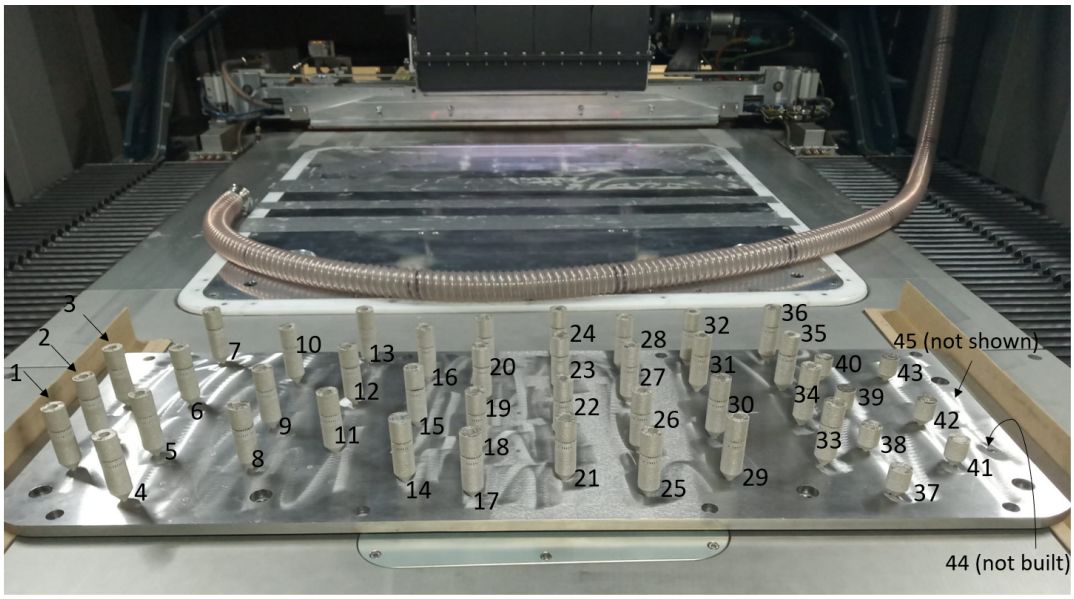

Figure 3.10: Final result of the successful build job

3.3.3 Sample preparation and testing equipment

After removing all the parts from the substrate the following preparation was conducted on the support specimens:

1. Cutting the conical end with a disc saw
2. Facing the cut surface on a lathe: manual feed; 900 rpm
3. Drilling on lathe: 10.25 mm diameter; manual feed; 315 rpm
4. Countersinking: manual feed; 315 rpm
5. Threading: M12, manually with threading tool
6. Repeat steps 3 - 6 on upper end of the specimen

The specimens tested using the Material Testing System MTS 810, which is a uniaxial servo-hydraulic universal testing machine equipped with a 100 kN load cell. The specimens were fixed using the studs as was previously explained (Figure 3.11). Due to the non-standard dimensions of the specimens, and the main focus on obtaining the maximum load, no strain gauges or clip gauge were used.

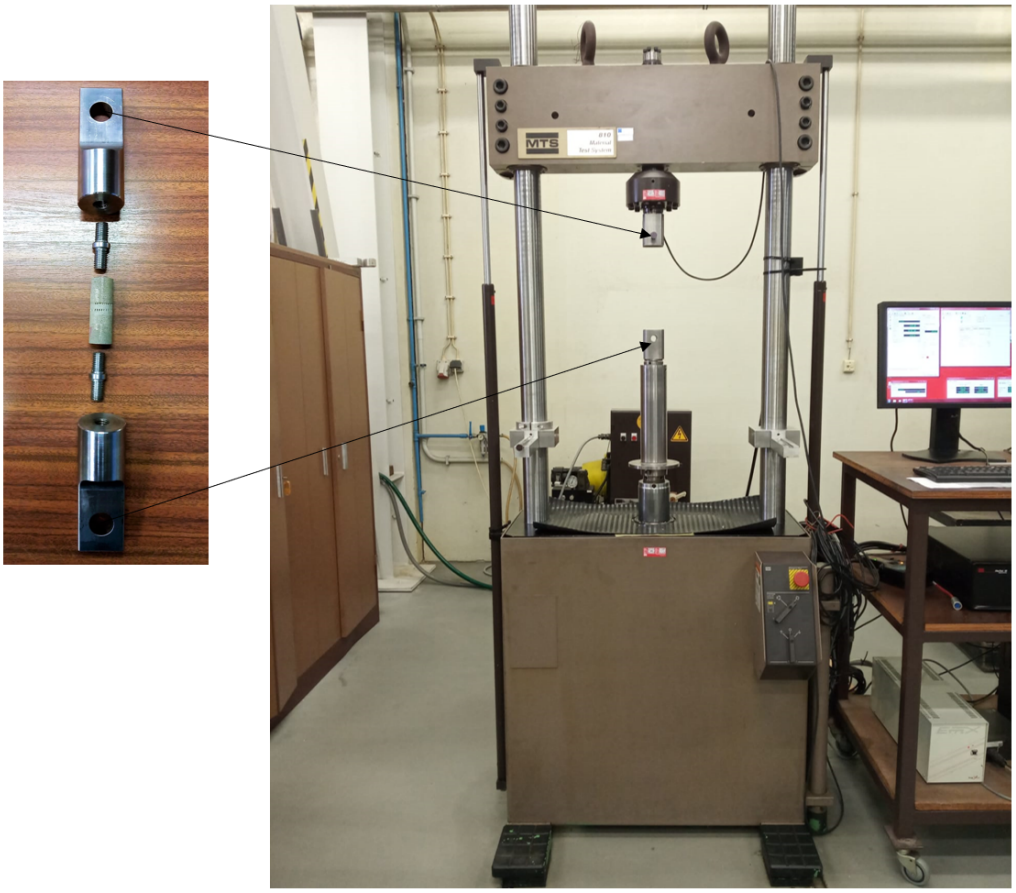

Figure 3.11: Specimen set-up and tensile testing machine

The density samples were analysed using the optical microscopy method instead of others such as the Arquimedes method due to the ability of evaluating the morphology and distribution of the pores. In order to obtain the microscopy pictures of the samples, they were prepared using the following procedure:

1. Cutting the conical end with a disc saw;
2. Abrasive Grinding: Silicon carbide, 80 to 800 grit size;
3. Abrasive Grinding: Water-based alumina suspension;
4. Polishing: Water-based, mono-crystalline diamond suspension 3 μm
5. Polishing: Water-based, mono-crystalline diamond suspension 1 μm

To evaluate the sections of the density specimens, optical microscopy was used. The equipment used was ZEISS Axiophot Fluorescent Microscope (Figure 3.12) connected to a 12 V , 100 W power supply. The microscope was equipped with cameras and the necessary image software (ZEN).

Figure 3.12: Optical microscope ZEISS Axiophot

In order to obtain representative measurements, 9 fractions of each sample section were analysed and the final result for each sample is considered the average of those 9 measurements. The analyses were conducted according to Figure 3.13. Each image was, then, binarized using the Otsu thresholding method, with the open source software ImageJ.

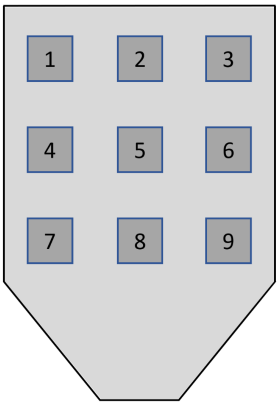

Figure 3.13: Schematic of the density measurement procedure

3.3.4 Numerical Simulation methodology

Parallel to the experimental procedure, it was decided to use numerical finite element analysis simulation to validate the results obtained with the new testing method proposed. The goal was not to simulate the melting of each layer and the thermal history of the build job, but only to verify the theoretical strength of the supports for the 2 levels of *tooth top length* and compare it to what would be obtained experimentally. To do this, the first step was to design the specimen on *SolidWorks 2021*. Then, this geometry was loaded into *Materialise Magics* ® where the supports are generated and these were exported as a .stl file. However, this type of file is a surface model, which means that the geometry is hollow and the body is represented by surfaces instead of a solid body. Besides, there could be very small holes in the mesh and the fine triangulation made it impossible to directly load this .stl file into the simulation, because it was very challenging to obtain a converging finite element mesh. Therefore, after exporting the .stl of the support structure, it was loaded into *Fusion 360*, where the mesh was stitched, and it was converted to solid bodies. This type of operation was tested in other CAD softwares but Fusion 360 proved to be the most efficient and user friendly for mesh correction and conversion. The supports for simulation were considered without the perforation to simplify these mesh correction operations, and since the critical section was the teeth's interface with the solid, this was expected to not have a significant impact on the results.

The simulations were created on *Ansys Workbench*, where the properties of the material were set according to the literature [75, 76]. An elasto-plastic constitutive model was considered. The work hardening curve was introduced by defining multilinear isotropic hardening, according to Table 3.12.

Table 3.12: Work hardening curve introduced in Ansys [76]

Plastic strain [mm/mm]	Stress [MPa]
0.0	276
0.2	645
0.4	905
1.0	1455
1.5	1940

Then, in the modeling environment of *Ansys Workbench*, *SpaceClaim*, the specimen was sectioned into one quarter of its geometry to reduce computational time. Partitions were also created in the teeth region to enable a smaller mesh in that area and provide more accurate results in due time. In the teeth region of the supports, the part was meshed with tetrahedral elements defined by their size in comparison to the teeth. Since it would not be possible to model the specimen taking the teeth penetration into account, assuming a continuous body, the specimens with a positive z-offset were not simulated. The boundary conditions were set as follows: displacement (x)=0 mm, displacement (y)=0 mm, displacement (z)=0 mm in the upper hole walls of the specimen and displacement (x)=0 mm, displacement (y)=0 mm, displacement (z)=1 mm (ramped) in the lower hole walls. The main result was the force reaction in the fixed surface of the test specimen.

This methodology is summarized in Figure 3.14.

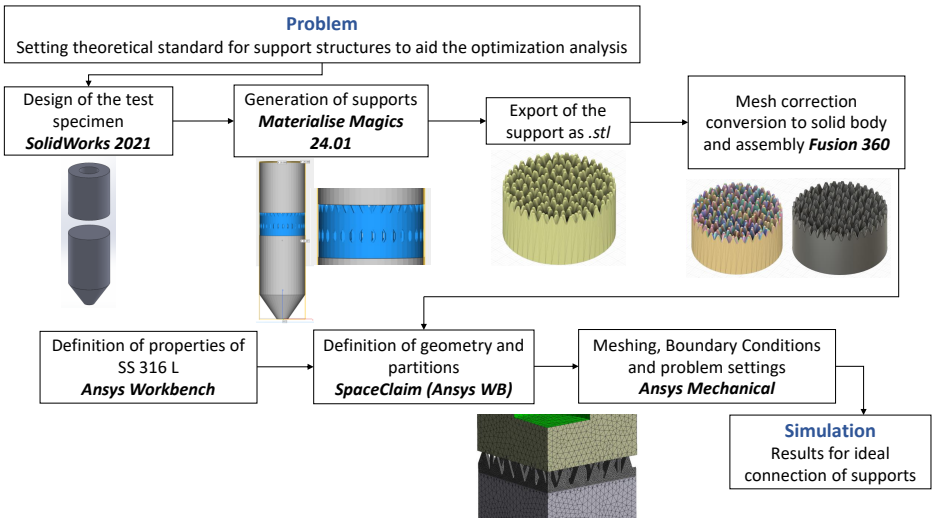

Figure 3.14: Procedure to obtain FEM results

Chapter 4

Results and Discussion

In this chapter all the experimental and numerical results are presented and analysed. The experimental results were subjected to a statistical analysis using Minitab Statistical Software in order to establish correlations with the processing parameters. The numerical simulation results were used as a reference for evaluation of the experimental tensile force and a short sensitivity analysis was performed. Density results were evaluated through optical microscopy and these results were correlated with the process parameters.

4.1 Results of supports' strength

After the sample preparation that was previously described, the support specimens were submitted to tensile testing. The goal was to perform a quasi-static test, so the actuator speed was adjusted accordingly. There was a first try at 1 mm/min, in which the specimen broke relatively fast, therefore, the adopted velocity of the hydraulic cylinder was then defined at 0.5 mm/min to ensure that no information or phenomenon passed unnoticed. One of the specimens (ID 17) was not evaluated because the solid body detached from the supports during handling in the sample preparation stage, when it was being threaded. The results of the maximum load obtained for each specimen during the tensile test can be found in Table 4.1, and the stress-strain curves are discussed in Section 4.3.1.

Table 4.1: Rupture force results

Specimen ID	F [N]	Specimen ID	F [N]
1	10523.97	19	8192.51
2	4545.61	20	6472.43
3	18377.51	21	10577.86
4	27144.34	22	16419.83
5	17927.15	23	11410.02

6	6823.37	24	7538.74
7	9410.00	25	6991.73
8	4824.84	26	12648.58
9	12283.65	27	13458.38
10	16384.33	28	7295.62
11	9763.79	29	18966.01
12	4772.32	30	17489.92
13	22397.61	31	11693.15
14	10410.30	32	15764.20
15	3610.41	33	14297.90
16	7233.98	34	4807.04
17	-	35	7181.67
18	14592.61	36	29185.48

The data was analysed with an balanced ANOVA in order to perform the analysis of means. For this, it was necessary to have the full matrix of results, which led to the necessity of estimating a value for specimen 17, according to the other observations (considered 4545.6 N). The results of the model are shown in Tables 4.2 and 4.3. According to these statistics, it is only possible to state, with a confidence interval of 95%, that the tooth top length (ttl) has an influence on the response. The scanning speed (v_S) would be the second most influential factor. It is also verified, by examining R-sq, that only 62,62% of the variance is explained by this model, and that the error, and consequently the amount of effects that are not explained by the model is quite large.

Table 4.2: Analysis of Variance for F_{rupt}

Source	DF	SS	MS	F	P_L
ttl	1	681354829	681354829	37.90	0.000
z	1	21321745	21321745	1.19	0.285
P_L	2	58875500	29437750	1.64	0.212
v	2	111706421	55853210	3.11	0.060
Error	29	521313436	17976325		
Total	35	1394571930			

Table 4.3: Model Summary

S	R-sq	R-sq(adj)
4239.85	62.62%	54.88%

Analysing the residual plots shown in Figure 4.1 there are three results outliers in the model. One of them is Specimen 15, with a very low load value. This specimen is shown in Figures 4.2 and 4.3 where it is possible to verify that it showed a clear defect, where the solid body had partially detached from support teeth during the build.

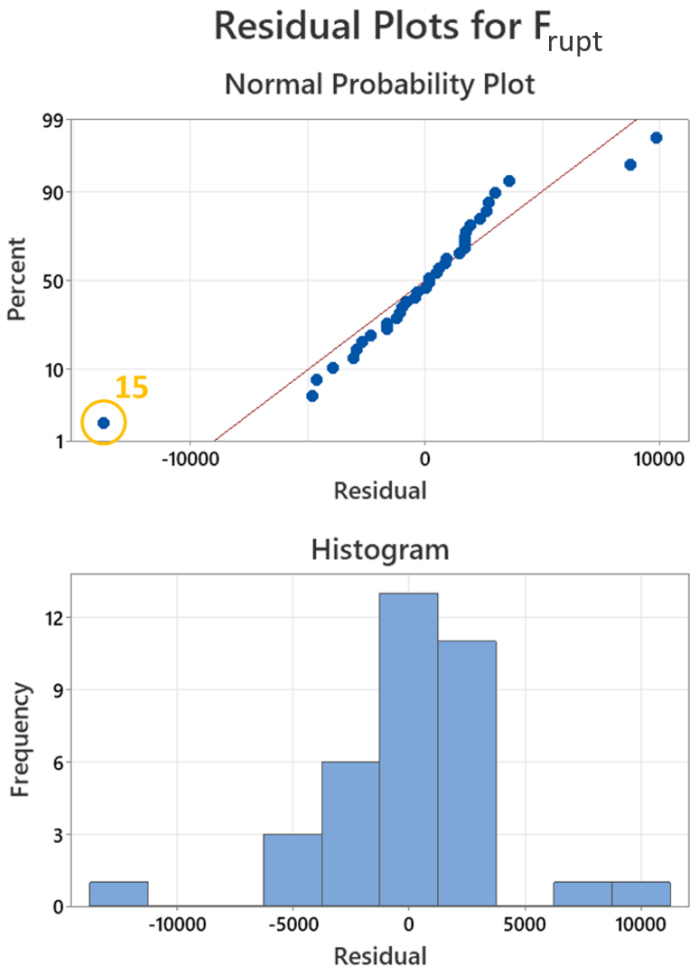

Figure 4.1: Residual plots for F_{rupt} considering the experimental value of Specimen 15

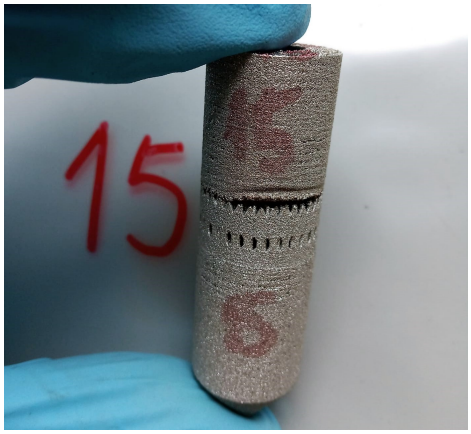

Figure 4.2: Visible detachment of specimen 15

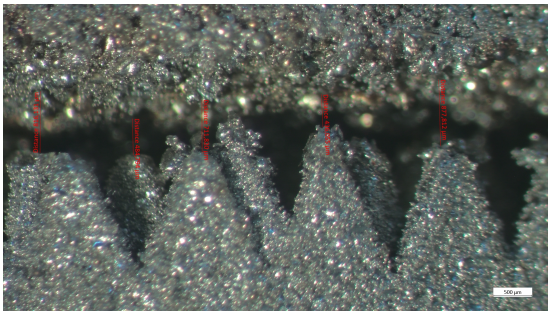

Figure 4.3: Measured detachment of some of teeth in specimen 15

This defect resulted in a detachment of over 800 μm in some teeth, which is problematic considering the 50 μm layer thickness. Hence, it was considered to be garbling the results and another analysis was conducted, where the value of the load for specimen 15 was also adjusted according to the most similar specimens. The z-offset had presented the highest p-value, indicating that this would be the least impactful factor. Therefore, adopting the same load as for specimen 13, which had all the same parameters instead z, the values of the new analysis of means are shown in Tables 4.4 and 4.5.

Table 4.4: Analysis of Variance for F_{rupt}, considering an adjusted response for specimen 15

Source	DF	SS	MS	F	P_L
ttl	1	854625256	854625256	85.09	0.0000
z	1	2209229	2209229	0.22	0.6426
P_L	2	76853808	38426904	3.83	0.0335
v	2	203819444	101909722	10.15	0.0005
Error	29	291286441	10044360		
Total	35	1428794178			

As expected, by adjusting the outlier the error has decreased and now almost 80% of the data is explained by the model. The main conclusions to draw from this means analysis is that the parameter with the biggest influence on the response is the tooth top length (teeth width), followed by scan speed, laser power and lastly by z-offset (teeth penetration).

Table 4.5: Model Summary

S	R-sq	R-sq(adj)
3169.28	79.61%	75.40%

After the analysis of means, a general factorial regression was created using Minitab, to understand main factors and second level interactions. The data was analysed without considering any response for specimens 15 and 17. An adjusted model was obtained, with an R-squared value of 89,56%. The Pareto chart showing the hierarchy of effects is shown in Figure 4.4. It is possible to confirm, with 95% confidence that the the following factors have an influence on the response: the tooth top length with the highest impact, followed by scan speed, the interaction between tooth top length and z-offset and, finally, z-offset and laser power, respectively. One conclusion that stands out is the low effect of the z-offset parameter when considered alone.

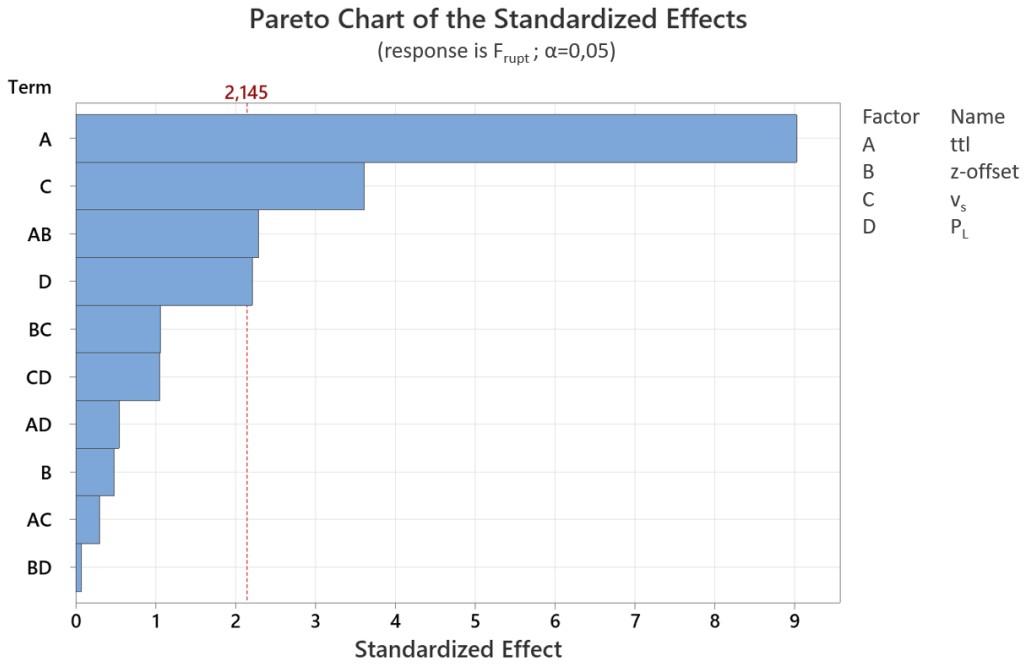

Figure 4.4: Pareto Chart for Maximum load, F_{rupt}

Figure 4.5 shows the effects of the 4 main factors. Again, the *ttl* chart shows the highest slope, corresponding to the strongest effect, while the z-offset slope is very low, confirming the low impact of this parameter, when the means of all samples is considered. The maximum load that the supports can withstand decreased linearly with an increase of the scan speed. On the other hand, increasing the value of laser power provided higher resistance of the support, although not in a linear way.

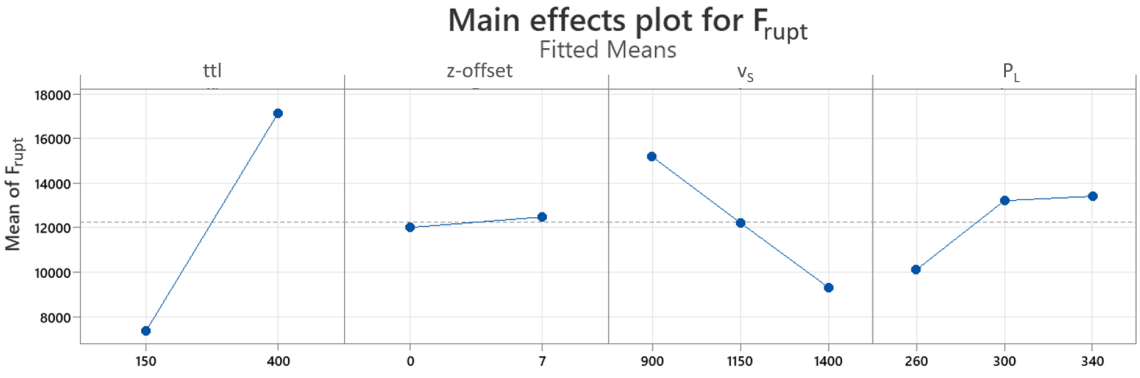

Figure 4.5: Main effects plots for maximum load, F_{rupt}

As for the interaction of the factors (Figures 4.6 and 4.7), it was found that an increase in teeth width (*ttl*) lead to a higher maximum load for all levels of z-offset, v_s and P_L. The teeth penetration, Z-offset, had the expected effect on F_{rupt} for the largest teeth (higher ttl), however it was found that for the smaller ttl values, the use of 7 layers of z-offset resulted in weaker supports. Considering all other parameters constant, increasing z-offset lead to higher support resistance, for all levels of laser power. The interaction of z-offset with scanning speed (Figure 4.6) showed that higher z resulted in higher F_{rupt} for the lowest values of v_s (900 and 1150 mm/s) however, there was an opposite behaviour for 1400 mm/s. Scan speed and ttl showed no combined relationship, which is indicated by the parallel lines in the interaction plot. The strength of the support decreased with the increase of scanning speed, for all ttl values (Figure 4.7). F_{rupt} also decreased for all z-offset values, but in this case there is a combined relationship - at lower speeds, the load was higher for the biggest z-offset and for higher speeds, the opposite occurred. Higher v_s also lead to lower F_{rupt} when the specimens were produced at 260 and 340 W (although not linearly) and, for 300 W it lead to a peak of force at 1150 mm/s. The rise of laser power strengthened the supports at all levels of z-offset and ttl (not linearly). This was also verified for the extreme levels of scanning speed, however, for 1150 mm/s the increase of power produces stronger supports from 260 W to 300 W, and a reduction in F_{rupt} from 300W to 340W.

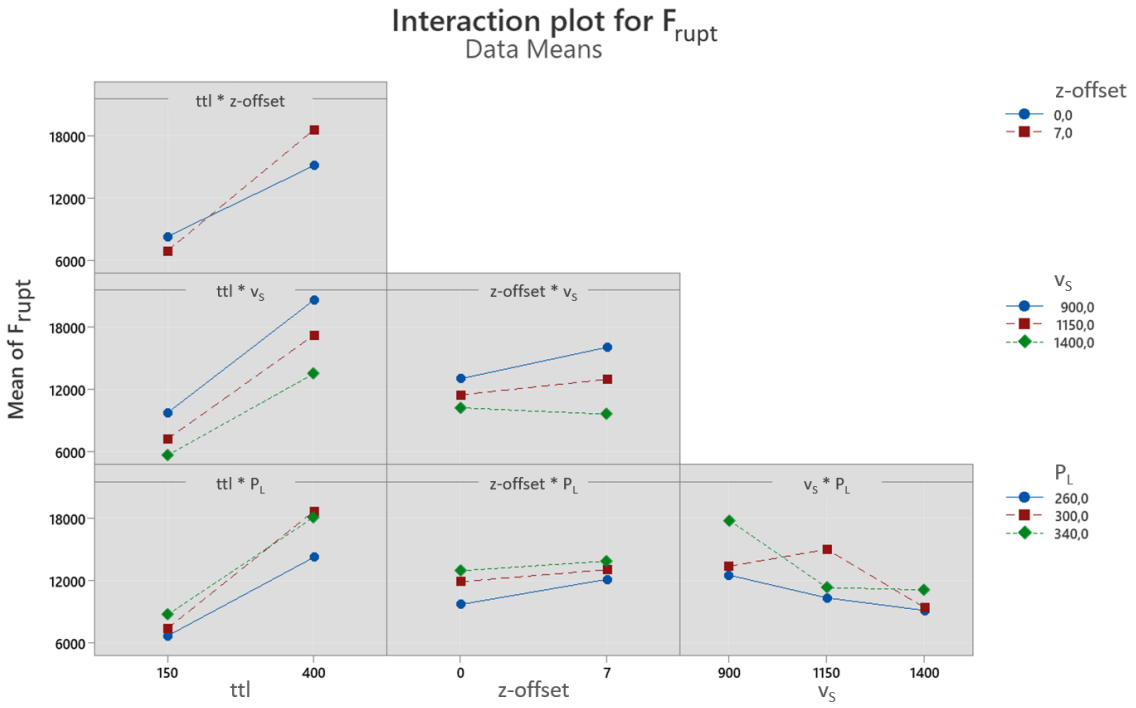

Figure 4.6: Factorial plot of interactions for F_{rupt}

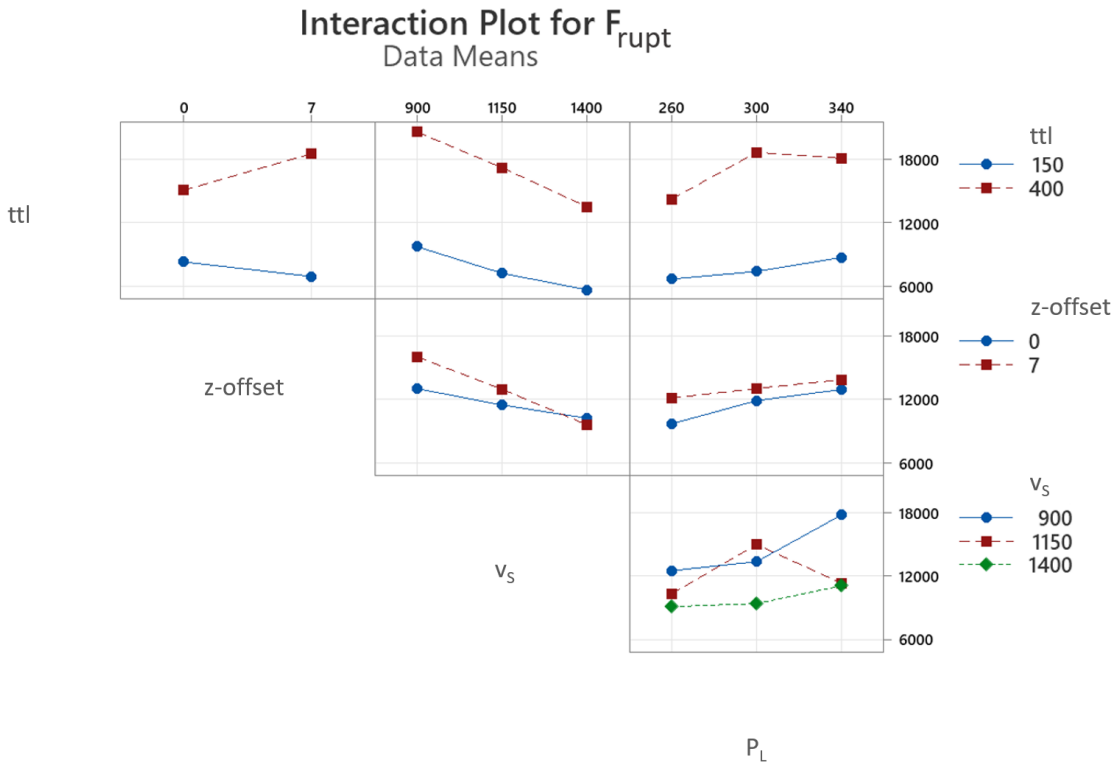

Figure 4.7: Interaction plot for F_{rupt}

4.2 Results of relative density

The relative density was evaluated using the aforementioned optical microscopy methods, considering 9 area fractions for each sample. Relative density of fraction was calculated according to Equation 4.1. The microscopy images of the samples were obtained, and the best (most dense) and worst (most porous) fraction of each sample are shown in Figures 4.8 - 4.23. The complety set of images is presented in Appendix C. It is important to highlight that some samples have a relatively low density, considering that values over 99.99% had been obtained with the same machine in other build jobs. The large amount and dimensions of pores leads to the entrapment of unfused material which is released during the polishing operations. This is the cause of the scratches on most images, even though the preparation procedures were executed correctly. The final average results of relative density of each sample are presented in Table 4.6.

$$d_{rel} = 1 - \frac{\text{total porous area}}{\text{total area}} \tag{4.1}$$

Table 4.6: Average density results

Specimen ID	E_d [J/mm^3]	Average relative density, d_{rel} [%]
37	45.22	87.48
38	52.17	95.03
39	75.56	95.46
40	48.57	90.84
41	37.14	88.34
42	66.67	98.65
43	59.13	97.87
44	42.86	-
45	57.78	98.53

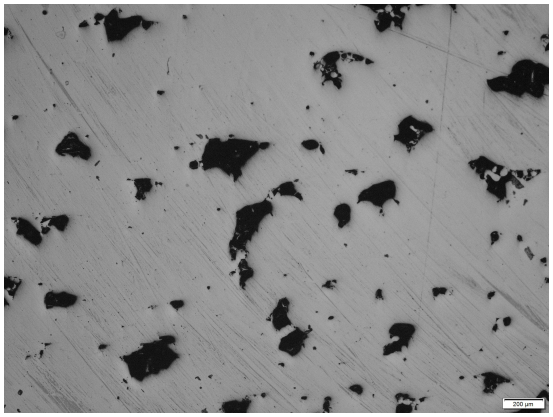

Figure 4.8: Best fraction of sample 37 (d_{rel}=92.47%)

Figure 4.9: Worst fraction of sample 37 (d_{rel}=85.13%)

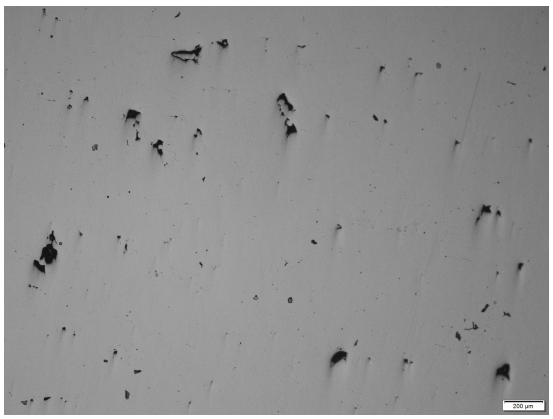

Figure 4.10: Best fraction of sample 38 (d_{rel}=99.11%)

Figure 4.11: Worst fraction of sample 38 (d_{rel}=91.59%)

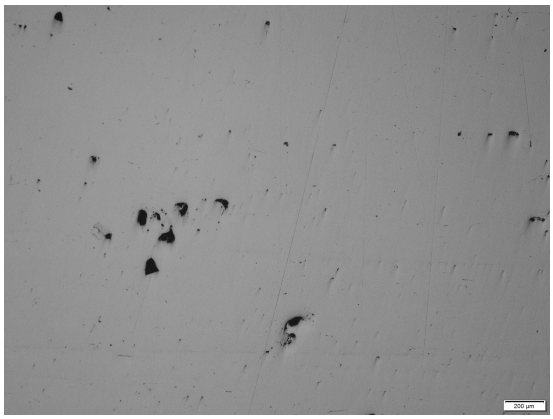

Figure 4.12: Best fraction of sample 39 (d_{rel}=99.59%)

Figure 4.13: Worst fraction of sample 39 (d_{rel}=91.62%)

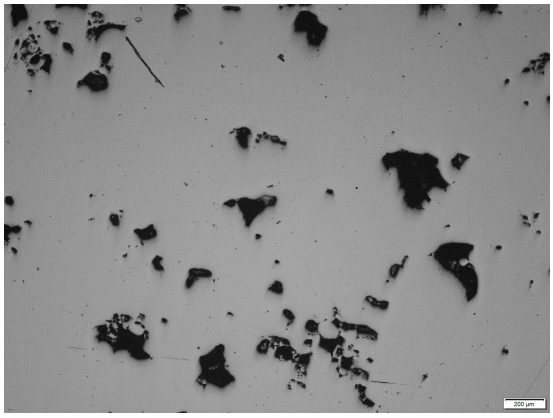

Figure 4.14: Best fraction of sample 40 (d_{rel}=93.94%)

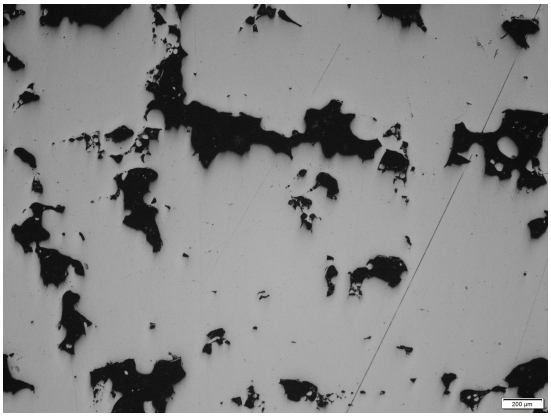

Figure 4.15: Worst fraction of sample 40 (d_{rel}=84.15%)

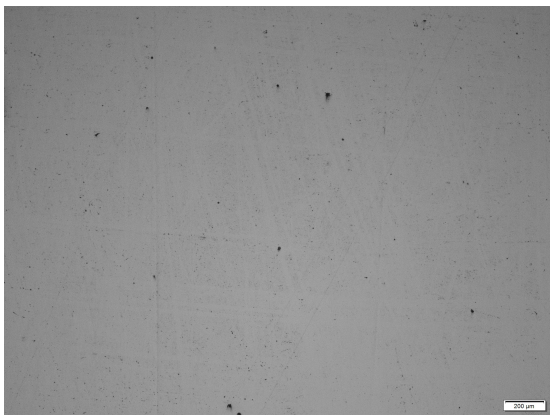

Figure 4.22: Best fraction of sample 45 (d_{rel}=99.97%)

Figure 4.23: Worst fraction of sample 45 (d_{rel}=95.45%)

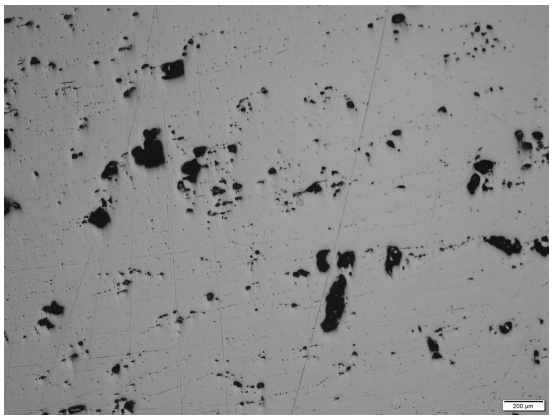

Figure 4.16: Best fraction of sample 41 (d_{rel}=95.89%)

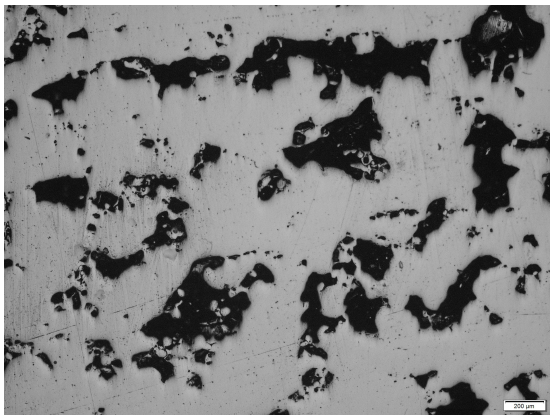

Figure 4.17: Worst fraction of sample 41 (d_{rel}=78.36%)

Figure 4.18: Best fraction of sample 42 (d_{rel}=99.97%)

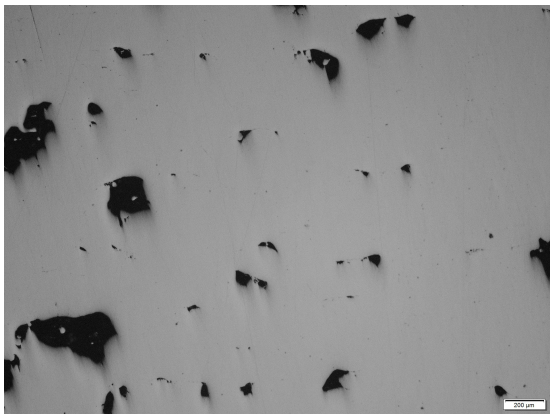

Figure 4.19: Worst fraction of sample 42 (d_{rel}=95.56%)

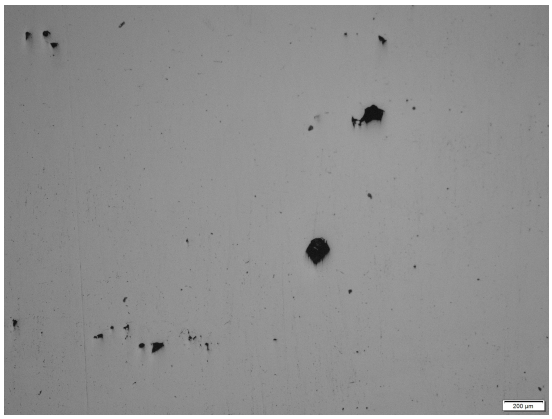

Figure 4.20: Best fraction of sample 43 (d_{rel}=99.51%)

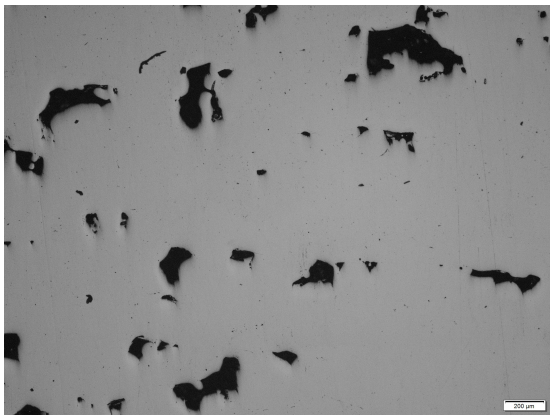

Figure 4.21: Worst fraction of sample 43 (d_{rel}=94.52%)

As an initial observation, it is possible to verify that overall the relative density values obtained are low. This may be related to two processing conditions. Although the lasers' lens had been cleaned before the build job, there may still have been some impurities, resulting from the machine's long continuous run time. When the lenses are not perfectly clean, it is possible that these particles cause loss of power, which could lead to deterioration of sample density and overall quality. Another aspect is that usually, there are two nitrogen flows being injected into the process chamber: a main gas flow and a secondary bypass flow. During this build job, this bypass flow was inactive which could have hindered the removal of the condensate fumes, causing the laser to be scanning over these condensate particles and worsening the full and homogeneous fusion of the powder. Nevertheless, the low relative density was not entirely surprising because support parameters were used and the goal was not to optimize parameters for part density.

In order to analyse the results and understand the influence of the scanning speed and laser power on the relative density of the samples, the average values of density (Table 4.6) were introduced into Minitab. Once again, the analysis of means was performed and both v_s and P_L presented a p-value larger that $\alpha = 0.05$, meaning that the variance of the means within each factor level is too large. Table 4.7 shows the degrees of freedom, adjusted sum of squares, adjusted mean of squares, f-value p-value of the variables in the model.

Table 4.7: Analysis of variance of relative density results

Source	DF	Adj SS	Adj MS	F-Value	P-Value
Model	4	0.009842	0.002460	1.61	0.363
Linear	4	0.009842	0.002460	1.61	0.363
v	2	0.006144	0.003072	2.01	0.280
P_L	2	0.002130	0.001065	0.70	0.565
Error	3	0.004593	0.001531		
Total	7	0.014435			

The values shows that for the typical confidence interval of 95% it is not possible to confirm, based on the model, either scan speed or laser power are significant in the density response. This is confirmed by the Pareto Chart shown in Figure 4.24.

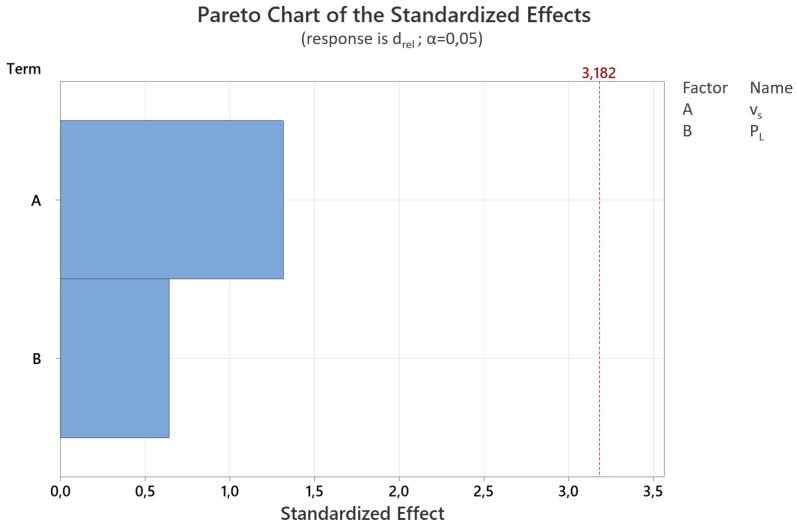

Figure 4.24: Pareto chart for relative density

Table 4.8 present the model summary statistics. It is possible to verify that the model shows a variance of 0.03913 (% of relative porosity). The R-sq value is 68.18%, which may be considered low because it means that only 68.18% of the variation in the response that is explained by the model. It is important to consider that small sample size decreases the precision of the estimation of the strength of the relationship between the variables and the response. Since the density was not the main focus point of this work and only 9 specimens were used (which were reduced to 8 due to production errors), this may be an indicator that the sample size was too small to create a statistical model with the most adequate fit. With this model it was not possible to perform the estimation of the combined influence of Scan Speed * Laser Power. There was an attempt to perform a Box Cox transformation on the data, in attempt to obtain a model with a better fit, however the results were similar, indicating that, in fact, the lack data for 1 specimen, the lack of repetitions in the design and the small sized sample are a likely explanation for this statistical results.

Table 4.8: Relative density Model Summary

S	R-sq	R-sq(adj)	R-sq(pred)
0.0391282	68.18%	25.76%	0.00%

It is also relevant to point out that the values within each specimen were quite dispersed, even though each of them is built with constant parameters. This is reflected in the pairs of images shown in Figure 4.8 - 4.23. The variance within each specimen was calculated, and sample 41 showed the largest disparity between the 9 measurements, reflecting on a variance of 0.2913% of relative density. In this specimen, the difference between the most and the less dense fractions is 17.5391% density. Other samples had a smaller difference between the maximum an minimum

value of density, ranging form 4% to 8%. Still, this may be an indicator that other factors are affecting the density of the parts and not just scanning speed and laser power.

In the Residual Plots in Figure 4.25, the histogram shows low skewness and instead, the bars show separations. The residuals versus fits fall randomly on both sides of zero without a recognizable pattern as they should. The fits vs order should also fall randomly around the zero line, however, there seams to be a trend. This indicates a correlation between the residuals (unexplained variance) and the dependent variable, meaning that there is a large amount of variance that is not being accounted for.

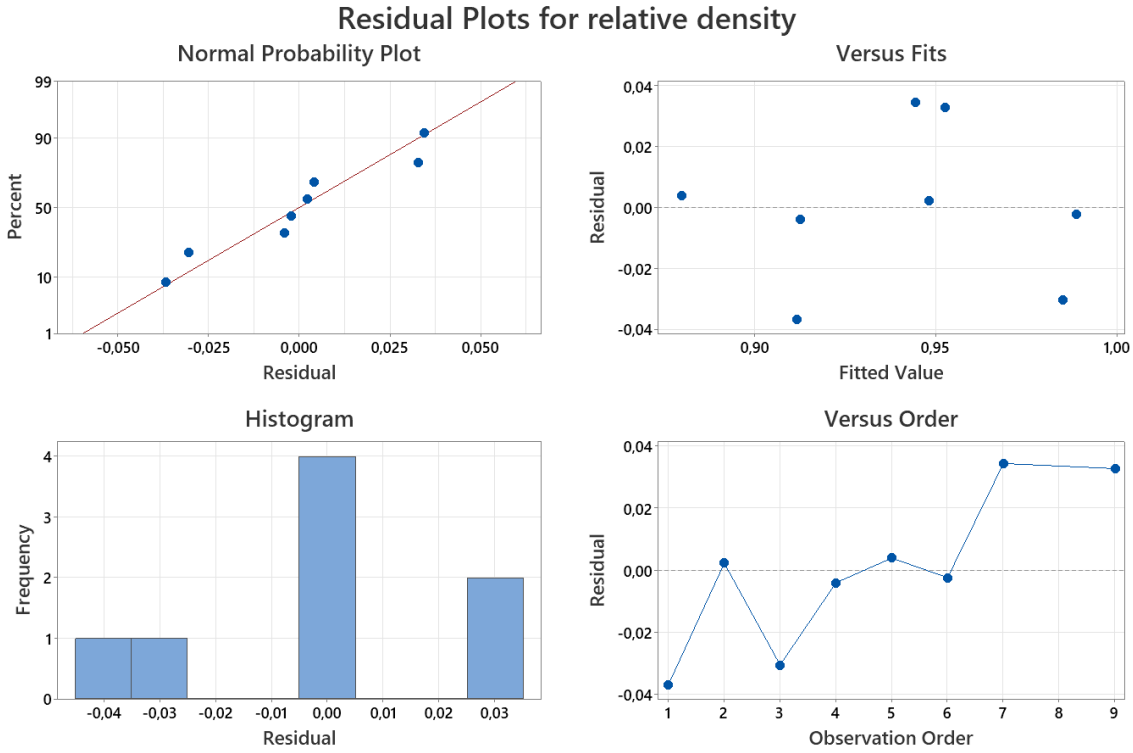

Figure 4.25: Residuals chart for relative density

Although the model is not perfectly adjusted and there is some missing information, it is still possible to make some observations. As the main effects (Figure 4.26), an approximately linear relationship between scan speed and relative density, where a higher speed led to lower porosity, on average. The effect of power alone, however, showed variation, leading to a peak in d_{rel} for 300W.

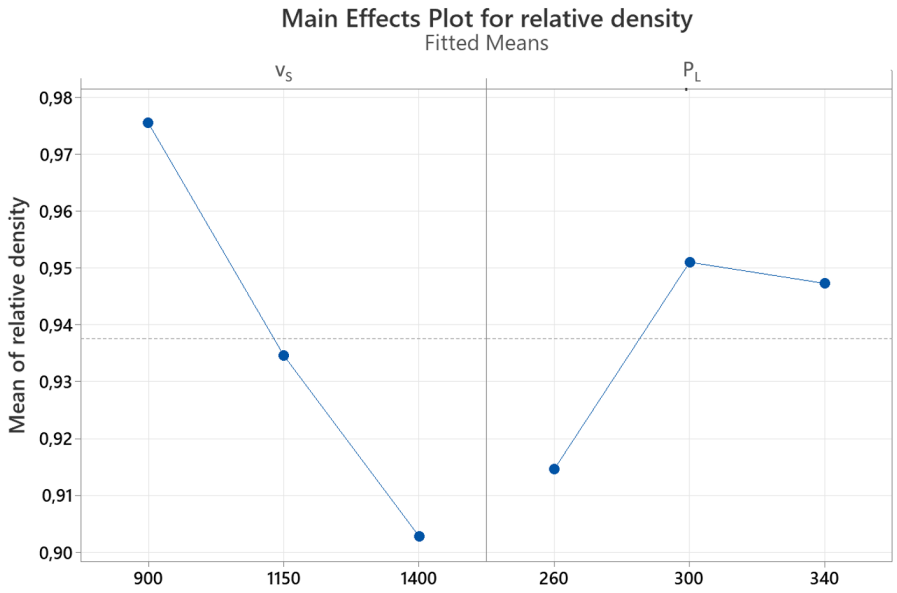

Figure 4.26: Main effects chart for relative density (v_S and P_L)

The interaction plots (Figures 4.27 and 4.28) show no parallel lines, meaning that there is an interaction between scanning speed, v_s, and laser power, P_L, which can affect the relationship between these factors and the response. The increase in v_s caused the decrease in d_{rel} at the lowest values of power. However, higher scan speed lead to a peak in density for the highest power value, at 1150 mm/s. With a further increase of scanning speed, although there is no data for 300 W (ID 44) it is possible to verify that, once again, the extreme levels of power (260 W and 340 W) lead to opposite behaviours. An increase in laser power tended to provide denser samples when these were produced at higher speeds.

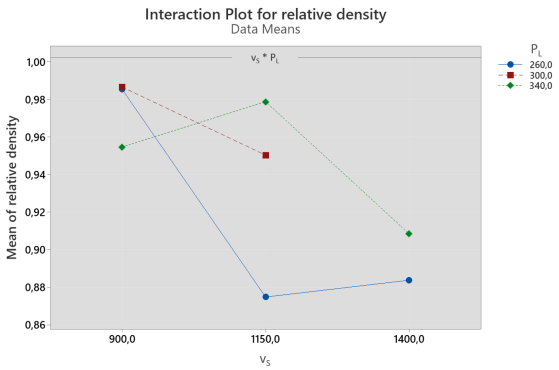

Figure 4.27: Interaction plot for density (with scan speed)

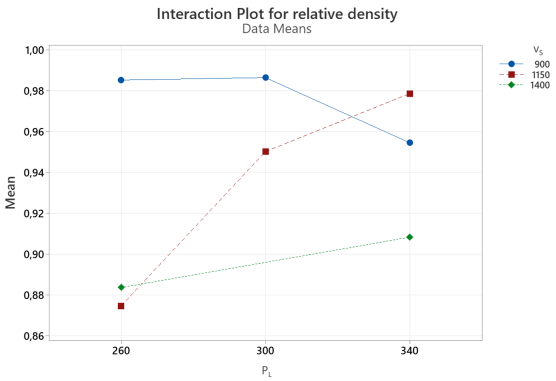

Figure 4.28: Interaction plot for density (with laser power)

4.3 Discussion

4.3.1 Supports' strength

From the analysis of means conducted in Section 4.1, it was found that the influence of $z-offset$ was the lowest out of the four parameters. However, the interaction plots provide more complete information on the different effect of this parameter for the 2 levels of ttl. This relationship is visible in Figure 4.29 (specimens 15 and 17 not represented), where it is possible to verify that for the lower level of teeth top length, 150 μm, having 7 layers of teeth penetration into the part actually weakened the connection, in all of the specimens. On average, D specimens showed a reduction of 22% of the maximum load supported, in comparison to their counterparts with no z-offset (A specimens). Considering the wider specimens, ttl=400 μm on average the penetration of the teeth for 7 layers strengthened the connection, increasing the maximum, as expected, by 19%. There was an exception to this trend between specimens 32 and 11, where, at 42.86 J/mm^3, the specimen with 0 z-offset (32) resisted at a higher maximum load. The effect of this parameter at smaller widths of teeth could suggest that they are more susceptible to internal defects like porosity and become less efficient at transferring the additional heat resultant from the second scanning in the same layer. In their final section (150 x 400 μm^2), the teeth are fully built using the contour because of their thin width in comparison to the beam diameter of 95 μm. There is also the possibility that the second contour scanning, in the middle of the main part hatching could induce some fragility in this thin support area. To fully understand the phenomenon, it would be interesting to study the microstructure in one of these 7 layers because the different heating and cooling cycles in the same layer could be harmful to these thinner supports. However, since in this experiment, this section was small (7 layers corresponds to 0.35 mm), making it difficult to perform the sample preparation, and due to constraints in resources and schedule, this investigation was not possible.

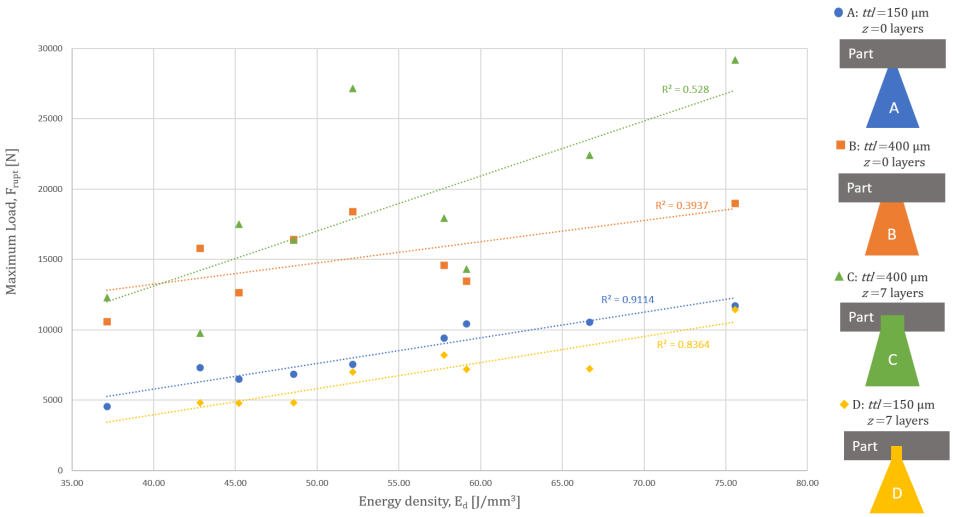

Figure 4.29: Effect of energy density on maximum Load for all combinations of v_s and P_L, for the 4 types of supports

The most essential requirement of the support is to prevent distortion of the parts by transferring heat. Therefore, microscopic pictures were taken at the interface of all specimens, which are documented in Appendix E. In total, 12 specimens showed some region that was detached from the supports, out of which 8 had ttl=150 μm and 4 of them ttl=400 μm (all of B type of support, with z-offset=0). these 12 detached specimens were equally distributed across all levels of power (4 cases for each P_L value). For ttl=150 μm - A and D types - the lowest scan speed, 900 mm/s, assured the connection of all specimens. On the other hand, 75% of the detached specimens corresponded to 7 layers of z-offset (D), explaining the lower values of force found for this type of specimen. As for ttl=400 μm none of the C type specimens showed any detached areas, corroborating the observation drawn form Figure 4.29, that for 400 μm wide teeth, the scanning of penetrating layers in the teeth onto the part improves interface connection.

The results directly obtained from the tensile test were the force, F_{rupt}, as a function of the displacement, δy, imposed on the specimen. All specimens were measured before the test, namely lengthwise. Total length of the specimen (after cutting the conical base), l_0, the known contact areas $A_{contact}$, and the data of force an displacement were used to calculate the engineering strain and stress, according to Equations 4.2 and 4.3.

$$\varepsilon = \frac{\delta y}{l_0} \tag{4.2}$$

$$\sigma = \frac{F}{A_{contact}} \tag{4.3}$$

After this step, the stress-strain curve was also plotted for all specimens. The complete results including all curves, are compiled in Appendix D. One example for one combination of the scanning parameter is shown in Figure 4.30. It is possible to notice that there is little to no plastic deformation of the specimen. It is clear the the rupture of the teeth happens right after the yield limit (end of the linear behaviour) is reached, and this load corresponds to the maximum value. Taking into account the different supports' geometry (Table 3.9) and analysing Figure 4.30 it is noticeable that the specimens whose support had the same teeth width (ttl), (A and D: ttl=150 μm; B and C: ttl=400 μm), and, consequently, the same contact area, show a very similar slope of the elastic linear part of the curve. This leads to the consideration that the teeth penetration into the part (z-offset) had little effect on specimen stiffness. It was verified that on average, the specimens with the thinner teeth (A and D) showed approximately twice as much stiffness and almost half of the resilience (area under the curve) compared to specimens B and C.

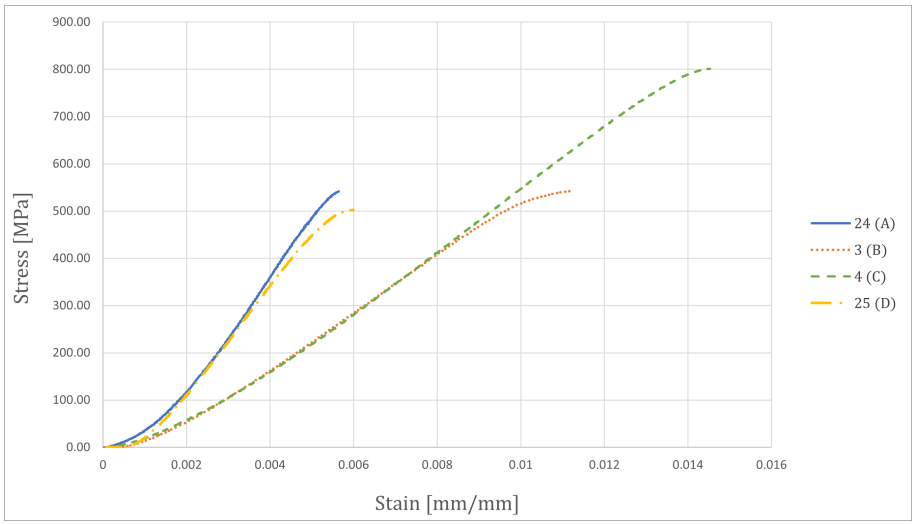

Figure 4.30: Stress strain curves of the 4 specimens manufactured at $v_s = 1150mm/s$ and $P_L = 300W$

This specimens' brittle behaviour caused the teeth to not be deformed significantly and the fracture to happen exactly at the interface between the teeth and the overhanging solid. In fact is is possible to detect that the support separation was as matter of interface. This is clearly visible in Figure 4.31, which represents the failure mode of all specimens except two (25 and 33) where some fragments of the teeth were deformed and remained attached to the downward overhanging body (Figure 4.32). Still, it is clear that the specimens ruptured due to the connection in that interface, as was expected.

Figure 4.31: Representative example of support separation

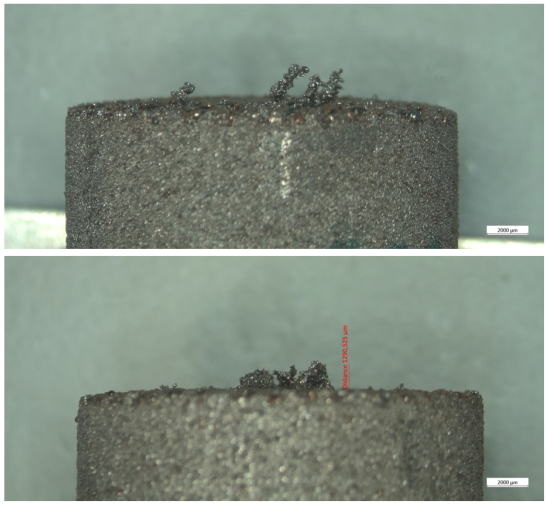

Figure 4.32: Only two specimens in which fragments of the teeth (1-2mm) remained attached to the upper body - IDs 25 and 33

A closer analysis of the interface surface after the fracture was conducted in an attempt to check for any visible differences in support performance. All the specimens showed similar visible aspect as the one represented in Figures 4.33a and 4.33b (full results attached in Appendix E). It is possible to see, both in the external walls of the solid body and in the support walls, that powders from the powder bed are sintered and become attached to these surfaces. This phenomenon is caused, in part, by the increase of the meltpool viscosity when the layers solidify and temperature decreases. This causes high surface tension and powder particles close to the the meltpood get attached and sintered into those surfaces. Another important aspect is that when the first few layers after the support structure are being processed the meltpool flows into the previous powder layers causing dross in the overhanging feature [59].This is especially noticeable in Specimen 4 (Appendix E), where the dross formed arround the teeth connection points. This surface roughness is aggravated by the absence of optimized parameters for contour during this build (the parameters were the same at the hatch and contour).

(a) Downward facing surface (b) Support structure

Figure 4.33: Interface of specimen 11

(a) 24 (b) 28

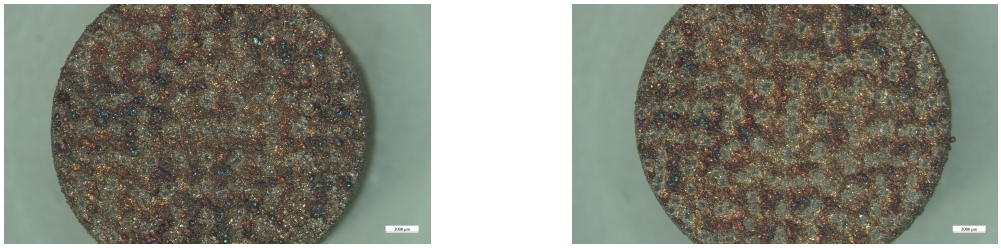

(c) 32 (d) 36

Figure 4.34: Darkest overhanging surfaces out of all the specimens

Besides the surface roughness, another detail was noticed. In samples 24, 28, 32 and 36, the interface surface presented a darker coloration than was expected. Initially, it was pondered that this could be be a consequence of low efficiency of the supports, leading to a poor heat conduction and overheating of these overhanging surfaces. There was an attempt to relate this observation with the processing parameters of these samples, however, as is detailed in Table 3.8, these specimens don't have enough parameters in common. For example, three of them were processed at 300 W, but so were many others, for example, specimen 1, which showed a completely different aspect. Scanning speed, and the support geometry (z-offset and tooth top length) were also inconsistent between these four specimens. Energy density was also varied among these specimens, as well as the estimated relative density - there was no data for samples 28 and 32, which corresponded to density sample 44, which was removed. However, using specimen 28, the relative density was estimated by observing areas of the support walls, in the same way that is described in Subsection 4.2. Although the geometry is different, the section is perpendicular to the build direction, the average result obtained was 98.35%. Since for specimens 24 and 36, the estimated relative density was of 95.03% and 95.46%, and other specimens with both lower and higher values don't show the same type of surface, this parameter also doesn't provide an explanation for this phenomenon. An additional factor that impacts the surface quality is the extraction of the condensate fumes and oxygen concentration in the process head, which should be less than 2000 ppm. It was observed, that the only aspect that the four specimens in Figure 4.34 had in common was their placement on the build platform. This layout is shown in Figure 4.35, where the powder deposition and the process head movement are also schematized. The powder is deposited from right to left and then spread from the front to the back of the powder bed. This often leads to an irregular distribution of the powder after the build area, when the small substrates are used. This is sketched in Figure 4.35 and is also visible in Figure 3.8.

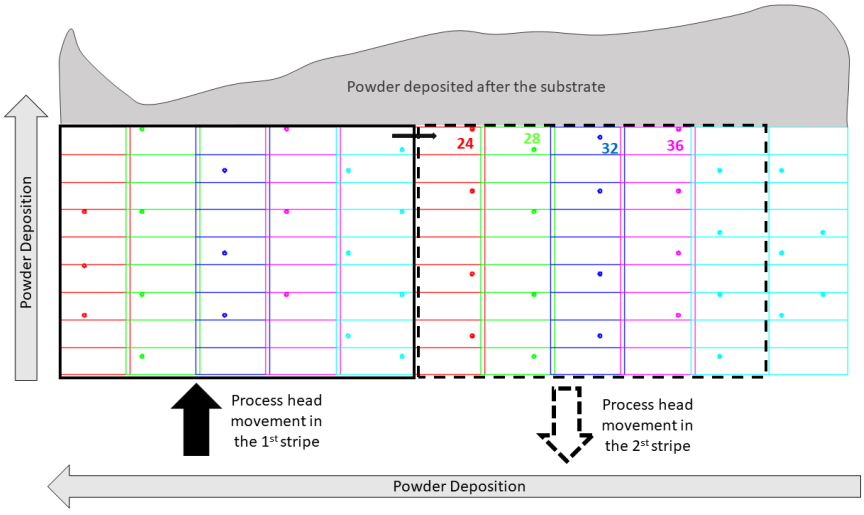

Figure 4.35: Layout of the specimens in the build platform, process head movement and powder distribution

This area of the powder bed is important because even though it situated after the substrate, when there are parts close to the edge of the plate, as is the case for specimens, 24, 28, 32 and 36, the process head approaches the end of the powder bed, and if there is no powder in that region, oxygen may enter into the process chamber, hindering the inertization conditions. When the laser is processing the last samples of the first stripe, the chamber is stopped close to the region where there is less powder and it would be possible that that oxygen contaminates the chamber volume and once it moves to the right to process specimens 24, 28, 42 and 36, that increase in oxygen could cause the oxidation of there specimens, conferring the darker surfaces detected. Furthermore, the lateral movement of the process head occurs in the perpendicular direction to the gas flow direction, which can cause turbulence in the desired laminar flow. The information from the O_2 sensors is displayed in Figure 4.36. The interface layer of the specimens is layer 931, and it is visible that there had been an increase in oxygen content up to that layer when the supports end, so there could be some oxidation at the the solid interface layer. Furthermore, it is also noticeable that the oxygen content always increases at the beginning of the second stripe, where those specimens were found. However this increase of approximately 200 ppm may not be large enough to explain this phenomenon, especially because the oxygen content remains under the threshold of 2000 ppm. Still, allied with the absence of the by-pass flow during the build job, this could be a cause for the poor surface quality found.

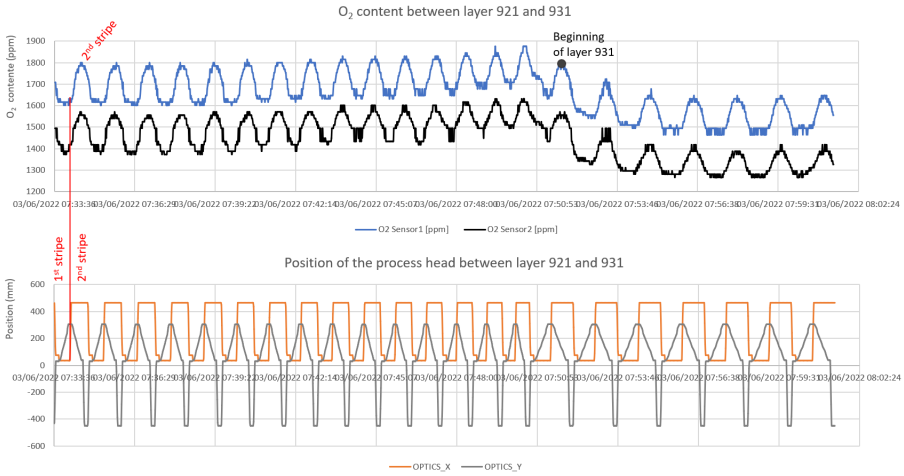

Figure 4.36: Oxygen evolution leading up to the interface layer

This surface quality also showed no correlation with the performance of the supports in terms of strength, since, samples 32 and 36 were able to withstand relatively high values of load, close to the expected theoretical.

From the strain-stress curves, the specimens' ability to store energy in the elastic domain was evaluated through the calculation of the modulus of resilience, U_R, given by the area under the tensile strength curve, according to Equation 4.4. The results are presented in Table 4.9.

$$U_R = \int_0^{\varepsilon_y} \sigma d\varepsilon \tag{4.4}$$

Table 4.9: Resilience moduli of specimens

Specimen ID	U_R [MPa]	Specimen ID	U_R [MPa]
1	2.82	19	1.61
2	0.64	20	1.18
3	2.95	21	1.14
4	5.46	22	2.42
5	2.82	23	2.95
6	1.22	24	1.31
7	1.99	25	1.39
8	0.69	26	1.41
9	1.42	27	1.66
10	2.29	28	1.27
11	0.96	29	2.77
12	0.71	30	2.42
13	4.10	31	2.75
14	2.50	32	2.09
15	0.27	33	1.65
16	1.35	34	0.83
17	-	35	1.28
18	2.11	36	8.65

As was already mention, and is visible in Appendix E, some supports did not manage to fully prevent distortions in the solid probe, causing it to detach slightly from the teeth in some regions. On average, it was found that, for the same ttl, the specimens that remained fully attached to the supports were built on the support structures with higher (almost double) capacity to absorb energy without suffering permanent deformation (U_R) than those which showed some detachment before testing. For example, Table 4.10 shows the average values of this modulus for the 2 types of support with 0 z-offset, where it's noticeable that specimens that remained fully connected tend to have been built on more resilient teeth. Another relevant observation was that on average, U_R tended to decrease with increasing scan speed and tented to increase with higher laser power, as is shown by the trendlines in Figure 4.37. This leads to the conclusion that the most resilient supports would be found at the highest energy density value and, in fact, observing the specimens built in these conditions (23,29,31,36), none of them show loss of connection of the interface between the part and the supports. Another energy density value that ensured an adequate connection was 57.78 J/mm^3 - 900 mm/s; 260 W. More specifically, the best results were found for 900 mm/s, since at this level of scan speed, only one specimen out of twelve specimens showed some detachment and it was Specimen 15, whose detachment seemed to be a result of a localized deformation, but the rest of the perimeter was well attached. However, from a productivity standpoint, this level of

scan speed would be the least favorable. A good compromise could be to adopt 42.86 J/mm^3 (1400 mm/s; 300 W) or 59.13 J/mm^3 (1150 mm/s; 340 W), which resulted in one detached specimen.

Table 4.10: Comparison of resilience of detached and attached supports (before testing)

Specimen type	Avarege UR of detached specimens [MPa]	Avarege UR of atached specimens [MPa]
A	1.20	1.90
B	1.70	2.01

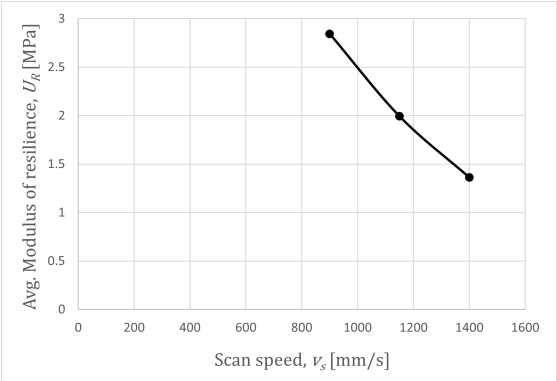

(a) Average modulus of resilience for each level of scan speed (considering all specimen types)

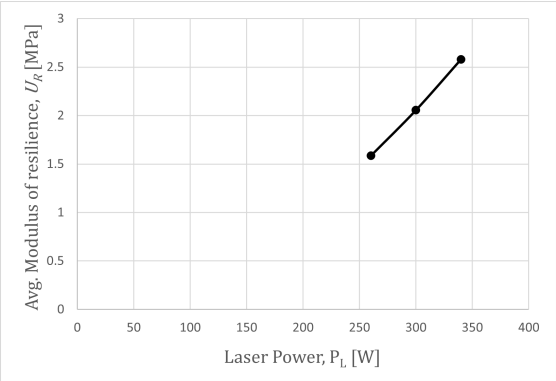

(b) Average modulus of resilience for each level of laser power (considering all specimen types)

Figure 4.37: Influence of scanning parameters on the resilience of support structures

4.3.2 Connection efficiency

As it was described in Section 3.3.4, the specimens were modeled and the tensile load was simulated in a Stactic Structural analysis in Ansys Workbench 2020.

While designing the studs, an estimate of 20 kN was calculated for the supports with wider teeth (Specimen B), according to Equation 3.2. Considering the equivalent estimation for the thinner supports, multiplying the reference ultimate tensile strength by the contact area, which is 13.92 mm^2, a rupture force of 8.2 kN was estimated for Specimen A.

In a first iteration, the element size was the same as the supports' width, ttl, that is 150 μm and 400 μm for specimens A and B, respectively. For specimen B, ttl=400 μm, two more simulations were ran, refining the mesh to an element size of 200 μm and 100 μm. However, in the simulation of 0.2 mm of element size, the number of nodes surpasses 700 000. Thereby, in the finer mesh, parts of the material on each side of the support was partitioned in order to eliminate the necessity of creating a mesh in the ends of the specimen, which were secured by the studs, in the experiment. Still, for the finer mesh, 2 241 780 nodes were analysed, making this simulation very time-consuming. For this reason, this brief sensitivity analysis was only performed for the specimen with larger teeth. For the specimen with smaller support teeth size, only one

mesh was simulated, of the same size as the tooth top length. The simulation resulted in a force-displacement curve and the maximum force in the axis direction of the specimen was compared with the maximum force obtain experimentally.

The results of these simulations are shown in Figures 4.38 and 4.39. The results of the brief sensitivity analysis are shown in Figure 4.40 which shows that the simulation line is almost perfectly approximated by an exponential function (R^2=0.999).

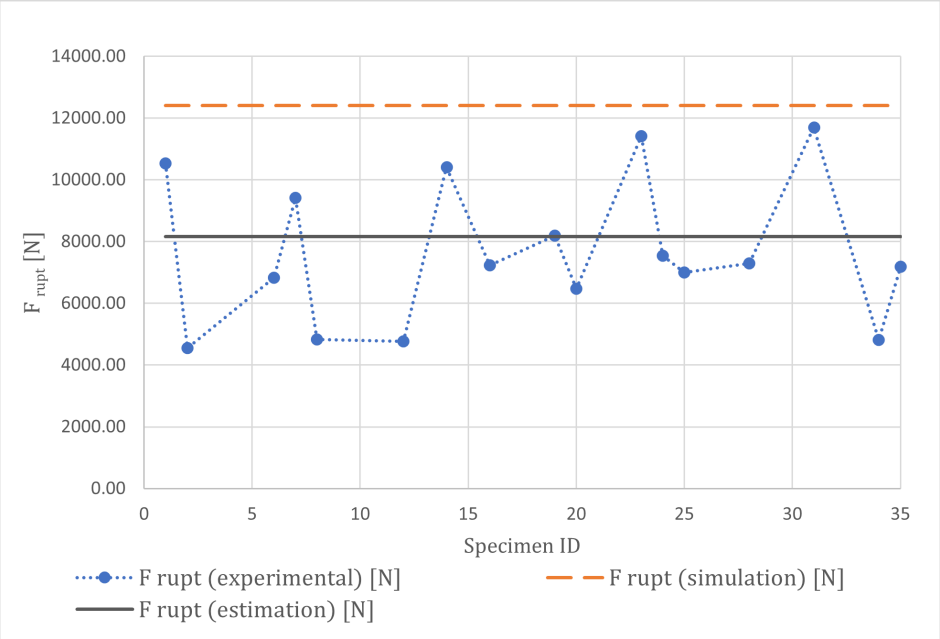

Figure 4.38: Comparison between experimental, estimated and simulation values of rupture force of specimens with teeth top length of 150 μm (A and D)

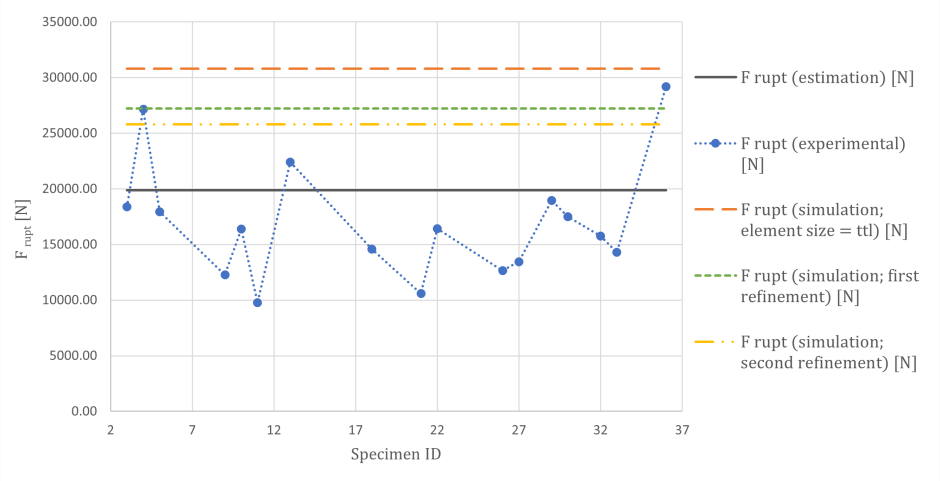

Figure 4.39: Comparison between experimental, estimated and simulation values of rupture force of specimens with teeth top length of 400 μm (B and C)

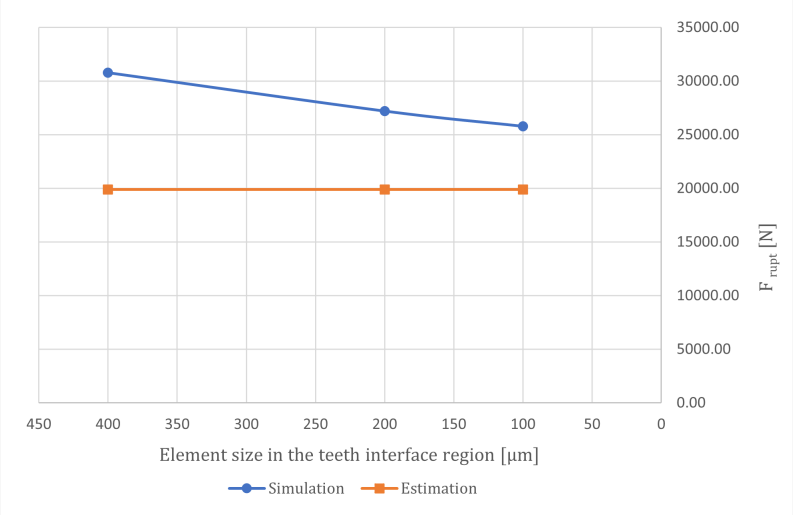

Figure 4.40: Sensitivity analysis of specimen B

It was verified that the simulation values always provided a higher result than the estimated force. This is related to the assumption that the engineering σ_{uts} is the highest stress applied to the specimen, in the estimation. In reality, the true stress felt by the specimen may be higher. This was taken into account in the simulation, by the input of the true strain-stress values, although they were adapted from the literature [76].

It was found (Figures 4.38 and 4.39) that in total, 9 specimens had a F_{rupt} higher than the estimation and 2 of them (ID 4 and 36), also higher than the simulation. Specimens 23 and 31 (Figure 4.38), only showed an error of 8% and 6%, respectively for the first and only simulation obtained for their geometry. If more mesh refinements had been perform in the simulation of specimen A, it is likely that the error would decrease even further.

The simulations resulted in a force-displacement curve of each specimen, considering an ideal material and a perfect connection between the teeth and the solid body. This curve displayed plastic deformation unlike the experimental case. In fact it was expected that the simulation results would mostly be higher that the real scenario because it is known that the specimens manufactured by AM would, almost inevitably, show some porosity. These pores act as stress concentration points and lead to defect propagation resulting in lower strength than the assumed perfect material. Another aspect that contributes to this is the dimensional accuracy of the supports. The grid of the block support is quite fine (400 μm walls, separated by 2 mm) and the teeth of the supports are quite small, especially in the case of specimens A and D are only 150 μm wide. Although the dimensional accuracy of the PBF process is relatively high, especially in comparison to other AM techniques, this small dimensions aren't perfectly respected in all areas of the support. Figure 4.41 shows the ideal section if the support teeth, in a layer between the base and the top of the teeth.

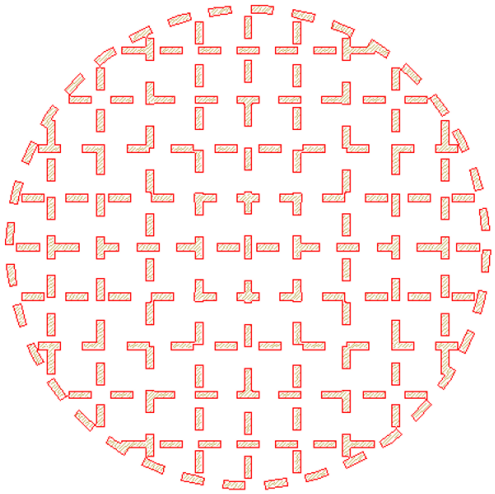

Figure 4.41: Ideal section of support grid (layer between the start teeth and the interface)

Figure 4.42 shows a comparable section of a real support with some dimensional deviations along the support walls, as well as some sintered powders that become attached to the surface of the walls due the the large residual heat in the small volumes of un-melted power in the grid. This small imperfections show the impossibility of having perfect rectangles in the interface of the support with the part which leads to the conclusion that there are small area deviations compared to the perfect prismatic supports modeled in the simulation.

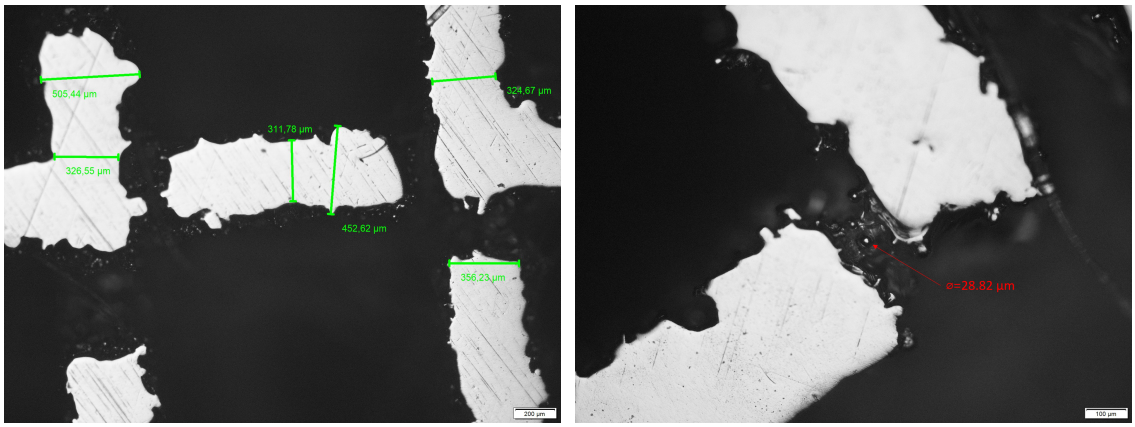

(a) Dimensional deviations in the grid (b) Sintered powders at block support's walls

Figure 4.42: Imperfections of the real supports (Specimen 28)

From these observations, a efficiency of the connection was computed, comparing all specimens of ttl=150 μm with the simulation of specimen A and all specimens of ttl=400 μm with the simulation of specimen B, according to Equation 4.5. The results are summarized in Figure 4.43.

$$\eta_{connection} = \frac{F_{rupture}}{F_{simulation}(\text{A or B})} \tag{4.5}$$

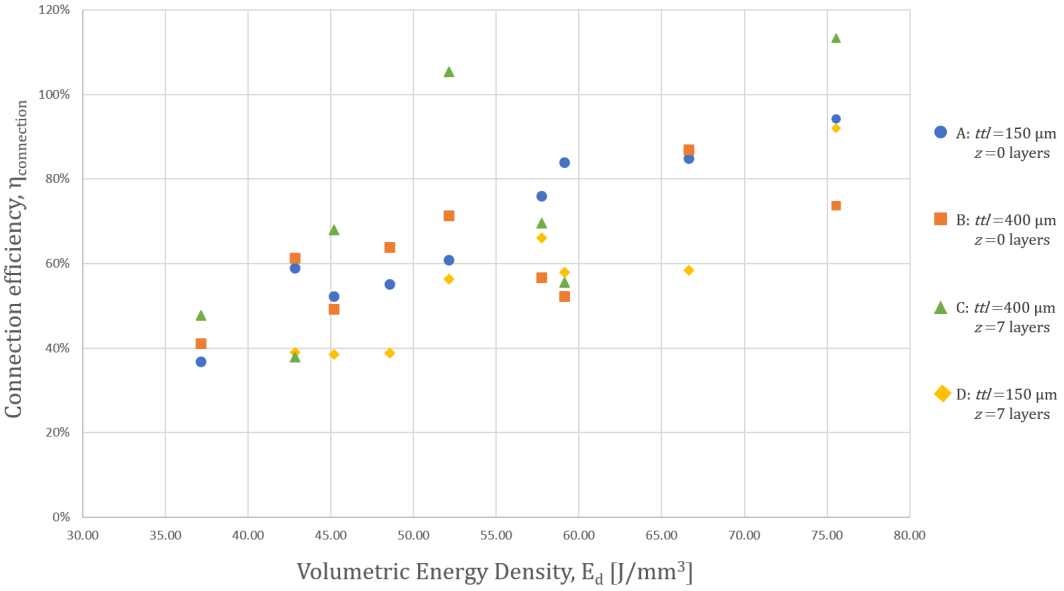

Figure 4.43: Connection efficiency for each combination of scan speed and laser power (energy density)

It can be concluded, as was expected from the previously analysed results of maximum load, the penetration of the teeth (z-offset) causes the efficiency to increase in the case of Support B and to decrease in Suppport A (Table 4.11). I is also possible to verify a trendline considering each type of support structure - increase of the energy density tens to result in support structure with better performance in terms of strength. Support C was the only one that was able to withstand higher force than predicted by the numerical simulation (efficiency over 100%).

Table 4.11: Efficiency of the supports according to teeth width and penetration

$\eta_{connection}$	z-offset = 0	z-offset = 7
ttl = 150 μm	66.90%	55.80%
ttl= 400 μmm	55.50%	68.10%

It is also noticeable that the efficiency of the connection of the support tends to increase with laser power and to decrease with higher scan speed - Figure 4.44. This shows, once again that the strongest supports are found at the higher levels of energy density. As expected, the supports that become detached present a lower efficiency (average $\eta_{connection} = 50\%$) when compared to the ones that were able to anchor the part properly (average $\eta_{connection} = 67\%$).

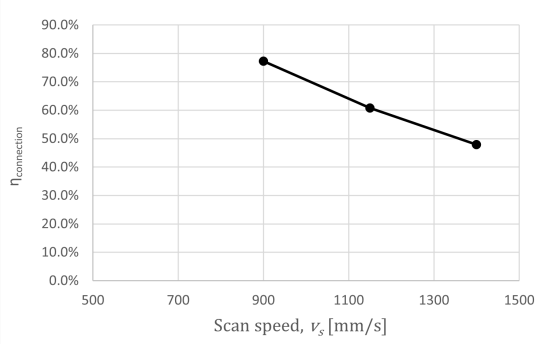

(a) Average connection efficiency for each level of scan speed

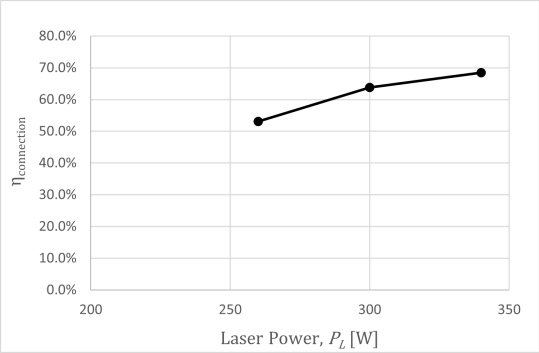

(b) Average connection efficiency for each level of laser power

Figure 4.44: Influence of scanning parameters on the connection efficiency

4.3.3 Relative density and its influence on support strength

Analysing the relative density of the sections, it was possible to detect different types of defects and classify them. A defect is considered a crack when its aspect ratio, given by Equation 4.6, is larger than 5, which is the case for one defect in sample 40 (Figure 4.45a). Gas pores are identified by their roundness - circularity, give by Equation 4.7, should be over 95% (Figure 4.45b). An example of this type of defect was found in sample 43, with a circularity of 99%. Finally it was also possible to verify unmelted particles as inclusions within a defect and defects caused by lack of fusion. This was the most common type of defects found in the samples of this build job. Examples of these defects are shown in Figures 4.45c - 4.45d.

$$AR = \frac{r_{major}}{r_{minor}} \tag{4.6}$$

$$C = \frac{4\pi * A_D}{P^2} \tag{4.7}$$

Figure 4.46 shows the average value of relative density for each level of energy input. Apart from the most extreme values of energy density, there is a trend that higher power combined with lower speed result in samples with less porosity defects. As for the influence of relative density on the strength of the supports, it was verified that out of all the specimens of estimate relative density of the support higher than 98%, only one out of eight specimens showed some separation between the solid body and teeth (specimen 15, that suffered a localized deformation). On the other hand, for relative density under 91%, 7/12 specimens exhibited some interface failure.

(a) Crack (ID 40). Aspect ratio is 34.

(b) Gas pore (ID 43). Circularity is 99%

(c) Unmelted inclusions within the a lack of fusion defect (ID 37)

(d) Lack of fusion (ID 45)

Figure 4.45: Examples of defects found on density specimens

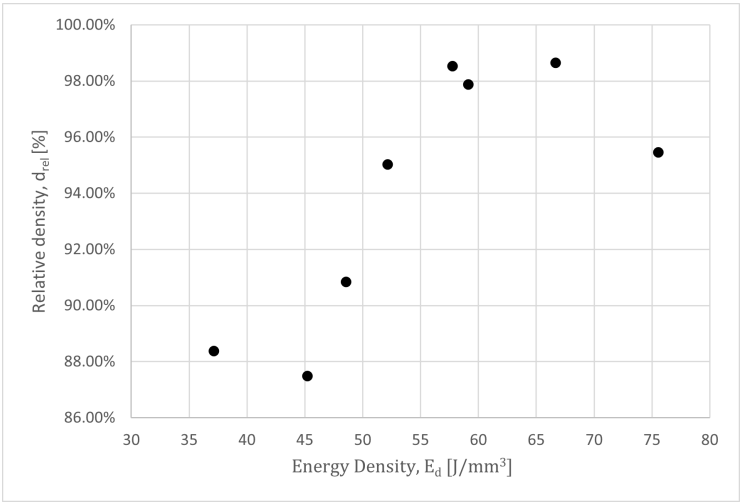

Figure 4.46: Relative density resulting from each level of energy density

Oliveira et al. [34] point to a scan trajectory that can induce porosity: "L" shaped turns. This laser path forces the laser to temporarily reduce its speed to change direction, thus increasing the scanning time and, consequently energy density input of a specific location. In the thinner supports, of 150 μm, the laser, which has a beam diameter of 95 μm is forced to perform two right angles right next to each other, which may cause an undesired increase in energy input an locally increase porosity. However, in AddCreator-AC210, this behaviour would only be a possibility in the teeth that are not aligned with either of the axis and due to the low inertia of the systems this

effect is, most likely, mitigated.

From the reference ultimate tensile strength, the expected theoretical rupture force has been estimated for each level of support width. The experimental error in F_{rupt} was determined for each specimen (theoretical estimation was used due to low refinement in the simulation of support B). It was verified that the reduction of porosity in the supports seemed to have an influence on the reduction of this experimental error. For supports with thinner teeth, an average error of 31% (absolute value) was obtained until 95.5% relative density. This error was then reduced to 8%, for the three lowest porosity values (relative density over 97.9%) - Figure 4.47. Furthermore, up untill 95.5% relative density, the rupture force is smaller than the expected theoretical calculation to increase with relative density, which leads to the conclusion that the increase of relative density provides higher strength of supports.

For larger ttl, the experimental error was more evenly distributed, which could indicate a higher sensitivity to porosity in the interface with the smallest contact area.

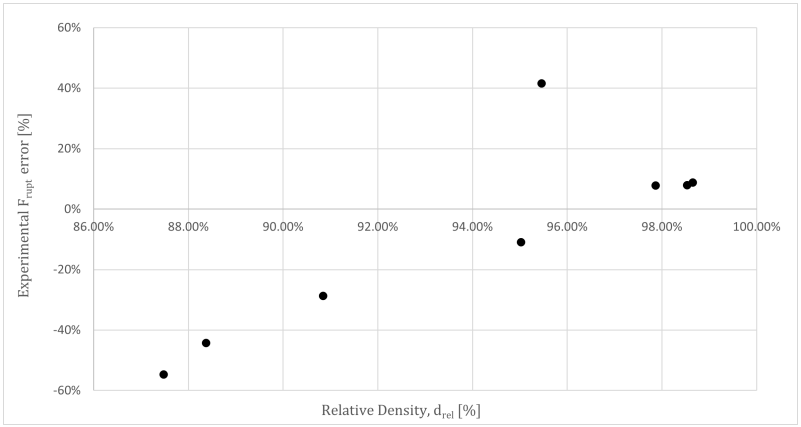

Figure 4.47: Experimental error in rupture force according to estimated relative density of the supports (for ttl=150 μm)

A summary of the relative density results is found in Figure 4.48, where for combination of P_L and v_s the microscopic image represents the fraction that was the closest to the average density value shown. It is possible to verify that the higher values of scan speed tend to decrease the resulting density, while the optimal laser power was, on average, of 300 W (although this is based on only two samples). It is also observed, as expected based on the literature, that for the lowest levels of energy density (high v_s and low P_L) the most common defect is lack of fusion porosity, which is characterized by large dimensions of pores (in, this case, over 200 μm) and irregular shape.

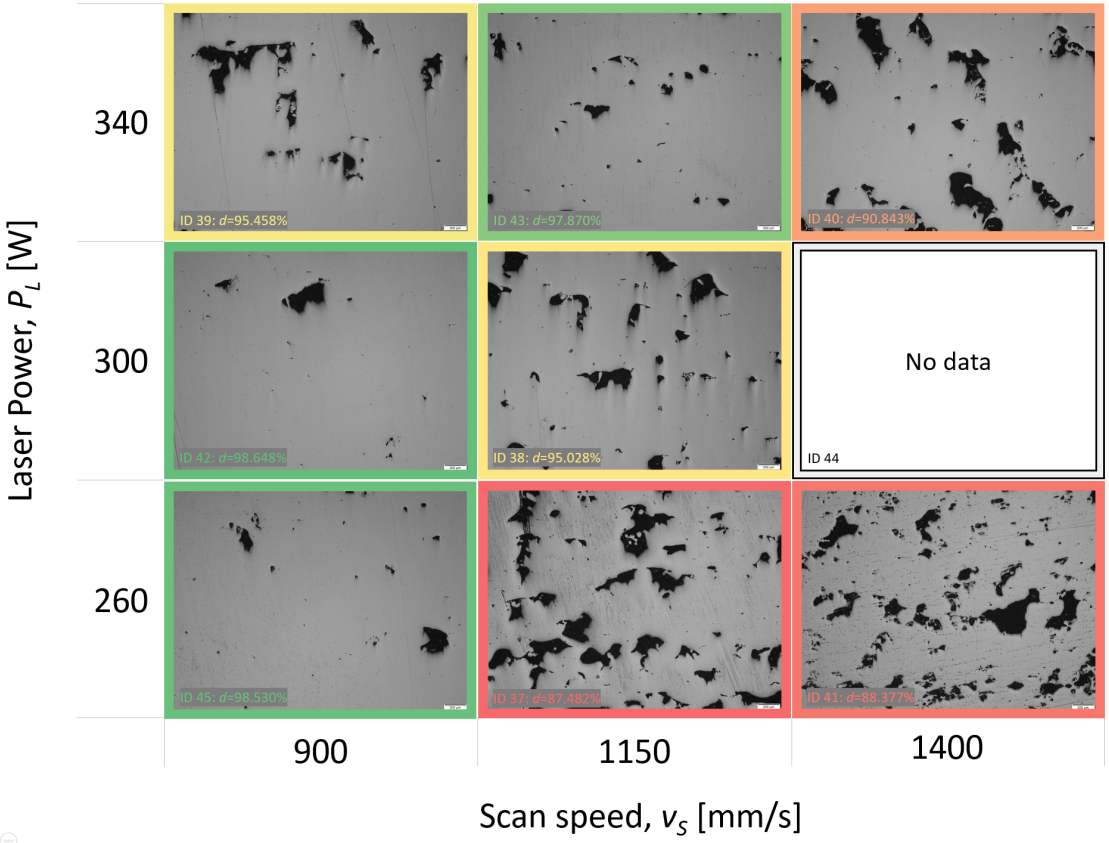

Figure 4.48: Summary of relative density with laser power and scan speed

4.4 Final remarks and guidelines on the proposed method

There is large variety of parameters and geometries available for support optimization in LPBF. The method proposed to evaluate support strength proved to be effective, because the tensile testing methodology provided insight on the allowable stresses on each type of support. This method does not fully characterize the ease of support removal. Nevertheless it may be estimated that the thinner supports that presented high connection efficiency and no detachment would be good compromising options (Specimens 23 and 31). A qualitative study in the degree of difficulty of support removal would be an interesting follow up investigation. The numerical simulation was useful to validate experimental results and provide a reference for the comparison of the specimens. An optimization of these capabilities could include gathering and using knowledge of the induced stresses during the build to design the optimal support for each situation. The density study provided an estimation of the expected relative density within the support structure. However the method for relative density analysis was manual and, therefore, very time consuming. In future implementations, the Archimedes methods could also be used for this purpose to obtain results that are, by themselves, representative a the whole sample. Since it is a non-destructive test optical microscopy analysis would still be possible afterward.

Chapter 5

Conclusions and Future Work

5.1 Conclusions

With the aim of optimizing process parameters in the manufacturing of support structures in Laser Powder Bed Fusion, an experimental an numerical methodology was proposed and executed. According to a full factorial design, 36 specimens were produced, using different values of scan speed, laser power, teeth top length and teeth penetration in the support region. Numerical simulations were conducted in order to set a reference for comparison with the experimental data. Density specimens were also produced, using the same levels of laser power and scan speed as in the supports.

With the work developed in the scope of this thesis it has been possible to draw the following conclusion:

- The width of the support teeth, ttl, is the most influential parameter on the rupture strength of the support. This parameter is followed by scan speed, v_S, as the second most crucial variable.
- The penetration of support teeth into the solid part's geometry caused the opposite effect of what was expected, for the most narrow teeth. A positive $z-offset$ in the 150 μm wide supports resulted in partial detachment of 67% of those specimens, making them fail under lower loads than expected. On the other hand, for the widest teeth, $z-offset$ of 7 layers generally increased support strength.
- Specimens with supports where the contact area with the part was smaller (low ttl) displayed more sensitivity to low relative density, that is, the relative density value had a larger influence on their strength. For this geometry, the relative experimental error was higher and the rupture force was lower for supports of relative density under 97%.
- The combination of scanning parameters leading to the highest energy density ($57.8 J/mm^3$), $v_S = 900 mm/s$ and $P_L = 340 W$ resulted in overall stronger supports. This was verified in

terms of higher values of rupture force, tensile strength and resilience. These parameters lead to the least detachments and distortion of the supported parts.

- Scanning speed of 900 mm/s enabled the minimization of part detachment, hindering, however, productivity.
- For the wider teeth specimens, mesh refinement provided increasingly more approximate results to the experimental rupture force. However, using mesh elements with a size of 100 μm or smaller, drastically increased computational time.
- The numerical simulation provided more reliable reference results than a theoretical estimation, because using FEM it was possible to consider work hardening of the material during deformation.
- The average connection efficiency of the designed supports was approximately 62%. The efficiency of supports that prevented distortion of the part was 67% while the supports that didn't fully withstand this load showed an average of only 50% efficiency.
- Relative density tends to increase with energy density for the range in study.
- Lack of fusion defects were found in the samples were energy density was lowest, as expected.
- For the supports with thinner teeth, higher estimated relative density resulted in smaller experimental error in support strength.

5.2 Further Work

Due to the complexity of the thermal and mechanical effects in PBF, the wide variety of parameters and geometries available for support design there is still the need for research and development in this field. To expand the knowledge gained from the work developed within the scope of this dissertation, it would be interesting to perform the following tasks in future works:

- Manufacture specimens with a higher number of layers as the z-offset parameter and observe of the microstructure of the material in that region.
- Study the influence of other scanning parameters on thin teeth, such as the offset between the hatch and contour vectors.
- To create a testing set-up to that would allow for shorter specimens, reducing build height and, thereby, optimizing build time and cost.
- Manufacture more repetitions of all specimens, in order to confirm observed trends.

- Explore more of the many available geometric parameters of the block support. After finding the set of parameters that ensures the connection between the part and the supports, developed in this study, it would be interesting to study x-y offset, breakpoints in the teeth and fragmentation at crossing. Optimizing these parameters could provide the optimal support where not only does the part remain attached without distortion, but also the support structures are, then, easy to remove.
- After this quantitative analysis of support strength, it would be important to perform a qualitative analysis on the ease of removing each of the supports.
- Explore other types of supports. For example, optimizing tree supports could facilitate the manufacturing of thin, overhanging channels, which is currently a difficulty.
- Perform tensile test on standard specimens to obtain the mechanical properties of the material in the as built condition and use this information as input into the numerical model to simulate non-standard geometries.
- Optimize the calibration of the finite element analysis simulation, so that from the knowledge of the thermal induced stress, it would be possible to quickly design the support structure.
- Include a defect-related failure criteria, such as the Gurson model, to predict mechanical properties based on the predicted porosity of supports and to use CZM models for the interface decohesion modeling.

References

[1] Terry Wohlers et al. *Wohlers Report 2019: 3D Printing and Additive Manufacturing State of the Industry*. Report. Wohlers Associates Inc., 2019.

[2] Prof. Dr.-Ing. Steffen Ritter. *formnext AM Field Guide Compact*. Report. Reutlingen University, 2021.

[3] Anton Wiberg. *Towards Design Automation for Additive Manufacturing : A Multidisciplinary Optimization approach*. Linköping University Electronic Press, Oct. 2019. ISBN: 9789179299859. DOI: 10.3384/lic.diva-160888.

[4] Roland Berger. *Additive Manufacturing – next generation AMnx*. Report. Roland Berger GmbH, 2016.

[5] Dr.-Ing. Maximilian Munsch, Matthias Schmidt-Lehr, and Dr.-Ing. Eric Wycisk. *Additive-Manufacturing New metal technologies, Upcoming technology principles: Potential and outlook*. Report. AMPOWER GmbH, 2020.

[6] CECIMO. "Key Market Trends in the European Additive Manufacturing Sector". In: *INTERNATIONAL CONFERENCE ON ADDITIVE MANUFACTURING – ICAM*. 2021.

[7] Dr. Maximilian Munsch et al. *Additive Manufacturing Management Summary*. Report. AMPOWER GmbH & Co. KG, 2021.

[8] Matthias Schmidt-Lehr and Timo Führer. *Design guideline for sinter-based Additive Manufacturing*. Report. AMPOWER GmbH & Co. KG, 2021.

[9] Carlo Burkhardt. "Beginner's Guide to 3 Leading Sinter-based Metal Additive Manufacturing Technologies". In: *International Journal of Powder Metallurgy* 14 (Sept. 2020), pp. 69–79.

[10] Dr.-Ing. Maximilian Munsch, Matthias Schmidt-Lehr, and Dr.-Ing. Eric Wycisk. *Metal Additive Manufacturing with sinter-based technologies: A deep dive into the emerging AM technologies*. Report. AMPOWER GmbH, 2020.

[11] *Stratasys is Pioneering a New Era in 3D Printed Production Metal Parts*. Online Multimedia, Accessed 07-04-2022. 2020. URL: https://youtu.be/tqU0U6-sAM4.

[12] Stephanie Hendrixson. *"Stereolithography for Metals" Produces Detailed Parts*. Web Page, Accessed 14-03-2022. 2019. URL: https://www.additivemanufacturing.media/articles/stereolithography-for-metals-produces-detailed-parts.

[13] S Singh, VS Sharma, and A Sachdeva. "Progress in selective laser sintering using metallic powders: a review". In: *Materials Science and Technology* 32.8 (2016), pp. 760–772. ISSN: 0267-0836.

[14] *MoldJet Technology*. Online Multimedia, Accessed 07-04-2022. 2019. URL: https://youtu.be/oiii7G7klMw.

[15] 3dpbm. *Metal AM Exploring the fastest growing area of industrial additive manufacturing*. Report. 3D Printing Business Media Ltd, 2020.

[16] Dr.-Ing. Maximilian Munsch, Matthias Schmidt-Lehr, and Dr.-Ing. Eric Wycisk. *Additive Manufacturing Material performance optimization*. Report. AMPOWER GmbH, 2020.

[17] Web Page, Accessed 09-04-2022. 2021. URL: https://commons.wikimedia.org/wiki/File:Selective_laser_melting_system_schematic.jpg.

[18] Ana Reis, Rui Amaral, and Jorge Gil. Generic. 2022.

[19] Torsten Petrat et al. "Microstructure of Inconel 718 parts with constant mass energy input manufactured with direct energy deposition". In: *Procedia Manufacturing* 36 (2019), pp. 256–266. ISSN: 2351-9789.

[20] Web Page, Accessed 09-04-2022. 2021. URL: https://www.youtube.com/watch?v=onrLbdb05z8.

[21] Michael A Gibson et al. "3D printing metals like thermoplastics: Fused filament fabrication of metallic glasses". In: *Materials Today* 21.7 (2018), pp. 697–702. ISSN: 1369-7021.

[22] J John Samuel Dilip, H Kalid Rafi, and GD Janaki Ram. "A new additive manufacturing process based on friction deposition". In: *Transactions of the Indian Institute of Metals* 64.1 (2011), pp. 27–30. ISSN: 0975-1645.

[23] MB Williams et al. "Elucidating the Effect of Additive Friction Stir Deposition on the Resulting Microstructure and Mechanical Properties of Magnesium Alloy WE43". In: *Metals* 11.11 (2021), p. 1739.

[24] Troy Y Ansell. "Current status of liquid metal printing". In: *Journal of Manufacturing and Materials Processing* 5.2 (2021), p. 31.

[25] V Sukhotskiy et al. "Magnetohydrodynamic drop-on-demand liquid metal 3D printing". In: *2017 International Solid Freeform Fabrication Symposium*. University of Texas at Austin.

[26] William J Sames et al. "The metallurgy and processing science of metal additive manufacturing". In: *International materials reviews* 61.5 (2016), pp. 315–360. ISSN: 0950-6608.

[27] Dr.-Ing. Maximilian Munsch, Matthias Schmidt-Lehr, and Dr.-Ing. Eric Wycisk. *Additive Manufacturing Make or Buy?: An overview of today's supplier market and cost structure for metal AM parts.* Report. AMPOWER GmbH, 2017.

[28] Web Page, Accessed 06-04-2022. 2021. URL: https://additive-manufacturing-report.com/technology/metal/laser-beam-powder-bed-fusion/#technology-variation-2.

[29] Dr. Maximilian Munsch et al. *Additive Manufacturing Management Summary*. Report. 2022.

[30] John Barnes. *A Technical Economic Perspective on Multi-Laser Powder Bed Fusion 3D Printers*. Web Page, Accessed 11-04-2022. 2020. URL: https://www.additivemanufacturing.media.

[31] Lindsay Luminoso. *Get more with multi laser additive manufacturing*. Web Page, Accessed 11-04-2022. 2021. URL: https://www.canadianmetalworking.com.

[32] Lindsay Luminoso. *Multi laser additive manufacturing*. Web Page, Accessed 11-04-2022. 2019. URL: https://www.canadianmetalworking.com.

[33] Ohio State University. *Developed multiple scan and build strategies to achieve advances in productivity and end part quality*. Report. Ohio State University, 2019.

[34] João Pedro Oliveira et al. "Processing parameters in laser powder bed fusion metal additive manufacturing". In: 193 (2020), p. 108762. ISSN: 0264-1275.

[35] Bi Zhang, Yongtao Li, and Qian %J Chinese Journal of Mechanical Engineering Bai. "Defect formation mechanisms in selective laser melting: a review". In: 30.3 (2017), pp. 515–527. ISSN: 2192-8258.

[36] "Lasers in additive manufacturing". English. In: *Optics and Laser Technology* 78.Part A (Apr. 2016), pp. 25–32. ISSN: 0030-3992. DOI: 10.1016/j.optlastec.2015.09.025.

[37] M.C. Sow et al. "Influence of beam diameter on Laser Powder Bed Fusion (L-PBF) process". In: *Additive Manufacturing* 36 (2020), p. 101532. ISSN: 2214-8604. DOI: https://doi.org/10.1016/j.addma.2020.101532. URL: https://www.sciencedirect.com/science/article/pii/S2214860420309040.

[38] Thomas G Spears and Scott A Gold. "In-process sensing in selective laser melting (SLM) additive manufacturing". In: *Integrating Materials and Manufacturing Innovation* 5.1 (2016), pp. 16–40.

[39] Tiago Carvalho Leça. "Efeito dos Parâmetros do Processo de TLM no Aço Inoxidável 316L". Thesis. 2018.

[40] Nils Ellendt, Fabian Fabricius, and Anastasiya Toenjes. "PoreAnalyzer—An Open-Source Framework for the Analysis and Classification of Defects in Additive Manufacturing". In: *Applied Sciences* 11.13 (2021), p. 6086. ISSN: 2076-3417.

[41] Fabrizia Caiazzo et al. “Laser powder-bed fusion of Inconel 718 to manufacture turbine blades”. In: 93.9 (2017), pp. 4023–4031. ISSN: 1433-3015.

[42] Ruidi Li et al. “Balling behavior of stainless steel and nickel powder during selective laser melting process”. In: *The International Journal of Advanced Manufacturing Technology* 59.9 (2012), pp. 1025–1035.

[43] Chor Yen Yap et al. “Review of selective laser melting: Materials and applications”. In: 2.4 (2015), p. 041101. ISSN: 1931-9401.

[44] Dr.-Ing. Maximilian Munsch, Matthias Schmidt-Lehr, and Dr.-Ing. Eric Wycisk. *Additive Manufacturing Material performance optimization*. Report. AMPOWER GmbH, 2020.

[45] Tatiana Mishurova et al. “The influence of the support structure on residual stress and distortion in SLM Inconel 718 parts”. In: 49.7 (2018), pp. 3038–3046. ISSN: 1543-1940.

[46] Omar Mireles, William Tilson, and Owen Hildreth. “Feasibility Study to Dissolve Additively Manufactured Inconel 718 Support Structures”. In: *AIAA Propulsion and Energy 2020 Forum*, p. 3501.

[47] Wessel W. Wits et al. “Porosity testing methods for the quality assessment of selective laser melted parts”. In: *CIRP Annals* 65.1 (2016), pp. 201–204. ISSN: 00078506. DOI: 10.1016/j.cirp.2016.04.054.

[48] A. B. Spierings, M. Schneider, and R. Eggenberger. “Comparison of density measurement techniques for additive manufactured metallic parts”. In: *Rapid Prototyping Journal* 17.5 (2011), pp. 380–386. ISSN: 1355-2546. DOI: 10.1108/13552541111156504.

[49] Thibaut de Terris et al. “Optimization and comparison of porosity rate measurement methods of Selective Laser Melted metallic parts”. In: *Additive Manufacturing* 28 (2019), pp. 802–813. ISSN: 22148604. DOI: 10.1016/j.addma.2019.05.035.

[50] Jean-Pierre Kruth et al. “Assessing and comparing influencing factors of residual stresses in selective laser melting using a novel analysis method”. In: 226.6 (2012), pp. 980–991. ISSN: 0954-4054.

[51] Damien Buchbinder et al. “Investigation on reducing distortion by preheating during manufacture of aluminum components using selective laser melting”. In: *Journal of Laser Applications* 26.1 (2014). ISSN: 1042-346X 1938-1387. DOI: 10.2351/1.4828755.

[52] Ahmed Hussein et al. “Advanced lattice support structures for metal additive manufacturing”. In: *Journal of Materials Processing Technology* 213.7 (2013), pp. 1019–1026. ISSN: 09240136. DOI: 10.1016/j.jmatprotec.2013.01.020.

[53] Renkai Huang et al. “Topology optimization of lattice support structures for heat conduction in selective laser melting”. In: *The International Journal of Advanced Manufacturing Technology* 109.7 (2020), pp. 1841–1851. ISSN: 1433-3015.

[54] S. Weber et al. “Parameters on Support Structure Design for Metal Additive Manufacturing”. In: *Proceedings of the Design Society: DESIGN Conference* 1 (2020), pp. 1145–1154. ISSN: 2633-7762. DOI: 10.1017/dsd.2020.14.

[55] Jamasp Jhabvala et al. “An innovative method to build support structures with a pulsed laser in the selective laser melting process”. In: *The International Journal of Advanced Manufacturing Technology* 59.1-4 (2011), pp. 137–142. ISSN: 0268-3768 1433-3015. DOI: 10.1007/s00170-011-3470-8.

[56] Katharina Bartsch, Joost Ohrenberg, and Claus Emmelmann. “Benchmark parts for the evaluation of optimized support structures in Laser Powder Bed Fusion of metals”. In: *Procedia CIRP* 94 (2020), pp. 254–259. ISSN: 22128271. DOI: 10.1016/j.procir.2020.09.048.

[57] F. Calignano. “Design optimization of supports for overhanging structures in aluminum and titanium alloys by selective laser melting”. In: *Materials & Design* 64 (2014), pp. 203–213. ISSN: 02613069. DOI: 10.1016/j.matdes.2014.07.043.

[58] Kaifei Zhang et al. “Study on the Geometric Design of Supports for Overhanging Structures Fabricated by Selective Laser Melting”. In: 12.1 (2019), p. 27. ISSN: 1996-1944. URL: https://www.mdpi.com/1996-1944/12/1/27.

[59] Peter Nils Johannes Lindecke et al. “Optimization of support structures for the laser additive manufacturing of TiAl6V4 parts”. In: 74 (2018), pp. 53–58. ISSN: 2212-8271.

[60] S. Catchpole-Smith et al. “Thermal conductivity of TPMS lattice structures manufactured via laser powder bed fusion”. In: *Additive Manufacturing* 30 (2019). ISSN: 22148604. DOI: 10.1016/j.addma.2019.100846.

[61] Naresh Nadammal et al. “Influence of Support Configurations on the Characteristics of Selective Laser-Melted Inconel 718”. In: *Jom* 70.3 (2017), pp. 343–348. ISSN: 1047-4838 1543-1851. DOI: 10.1007/s11837-017-2703-1.

[62] M. X. Gan and C. H. Wong. “Practical support structures for selective laser melting”. In: *Journal of Materials Processing Technology* 238 (2016), pp. 474–484. ISSN: 09240136. DOI: 10.1016/j.jmatprotec.2016.08.006.

[63] Kenneth Cooper et al. “Contact-Free Support Structures for Part Overhangs in Powder-Bed Metal Additive Manufacturing”. In: *Inventions* 3.1 (2017). ISSN: 2411-5134. DOI: 10.3390/inventions3010002.

[64] Kai Zeng et al. “Evaluations of effective thermal conductivity of support structures in selective laser melting”. In: *Additive Manufacturing* 6 (2015), pp. 67–73. ISSN: 22148604. DOI: 10.1016/j.addma.2015.03.004.

[65] Richard Andreotta, Leila Ladani, and William Brindley. “Finite element simulation of laser additive melting and solidification of Inconel 718 with experimentally tested thermal properties”. In: *Finite Elements in Analysis and Design* 135 (2017), pp. 36–43. ISSN: 0168-874X.

[66] Materialise Software. *Magics Simulation Manual*. Pamphlet. Leuven, Belgium.

[67] MSC Software Company. *Simufact Additive Tutorial*.

[68] Qiukai Lu, Erwan Beauchesne, and Tadeusz Liszka. "Enhancements to the inherent strain method for Additive Manufacturing analysis". In: *International Journal for Multiscale Computational Engineering* 17.1 (2019).

[69] Noha Peter et al. "Benchmarking build simulation software for laser powder bed fusion of metals". In: *Additive Manufacturing* 36 (2020), p. 101531.

[70] Marek Pagac et al. "Prediction of model distortion by fem in 3d printing via the selective laser melting of stainless steel aisi 316l". In: *Applied Sciences* 11.4 (2021), p. 1656.

[71] Web Page, Accessed 15-05-2022. 2022. URL: https://www.ramada.pt/pt/produtos/acos/aa-os-de-construa-ao-ligados/pm300-.html.

[72] J Simões Morais. *Desenho Técnico Básico*. Desenho de Construções Mecânicas. Porto, Portugal: Porto Editora, 2006.

[73] Peter Nils Johannes Lindecke et al. "Optimization of support structures for the laser additive manufacturing of TiAl6V4 parts". In: *Procedia CIRP* 74 (2018), pp. 53–58.

[74] Materialise Magics 24.01.

[75] Hyeong Do Kweon et al. "Determination of true stress-strain curve of type 304 and 316 stainless steels using a typical tensile test and finite element analysis". In: *Nuclear Engineering and Technology* 53.2 (2021), pp. 647–656. ISSN: 17385733. DOI: 10.1016/j.net.2020.07.014.

[76] Blandford RK et al. *Tensile Stress-Strain Results for 304L and 316L Stainless-Steel Plate at Temperature*. Report. Idaho National Laboratory (United States). Funding organisation: DOE-EM, 2007.

Appendix A

SS316L technical data sheet

METALS FOR PRINTING

m4p 316l

Stainless steel powder for laser-based powder bed fusion

Description and properties

m4p™ 316l is a corrosion-resistant austenitic alloy. The common abbreviation 316l comes from the AISI standard. In the European standardization the material 1.4404 has the highest possible conformity to the AISI standard of the 316l. Carbon contents <0.03% limit the tendency for intergranular corrosion effectively. The alloying element molybdenum contributes to further improvement of pitting corrosion resistance. As austenitic material, it has good deformation properties even at low temperatures.

Powder characteristics

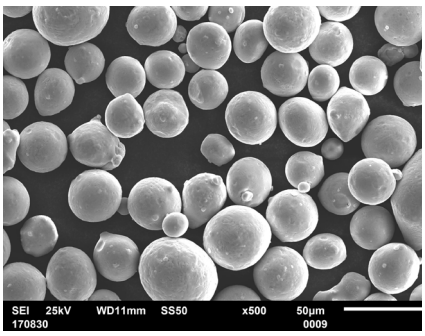

Chemical analysis [wt%]		
Element	Min	Max
C	<0,03	
Si	<1,0	
Mn	<2,0	
Cr	16,0	18,0
Ni	11,0	14,0
Mo	2,0	3,0
Fe	Base	

Particle size Laser PBF

Additive Fertigung und Festigkeitseigenschaften

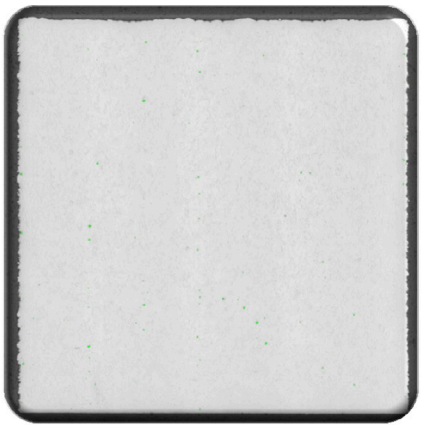

Typical characteristics of the tensile test (Parameter=99,95% rel. Density, as-built)		
Tensile strength	R_m =	574 N/mm²
Yield strength	R_e =	428 N/mm²
Elongation at break	A =	52%

Test cube:
10x10x10mm,
metallographically
determined density:
99,95%

www.metals4printing.com

INTERNATIONAL
m4p material solutions GmbH · Austria
Gewerbestraße 4, 9181 Feistritz i. R.
T +43 4228 93053-0
E sales@metals4printing.com

GERMANY
m4p material solutions GmbH · Deutschland
Mittelweg 13, 39130 Magdeburg
T +49 391 72149-40
E sales@metals4printing.com

The information and data contained in this data sheet have been compiled with care and the best of our knowledge, but are not to be considered as binding. We always recommend the user to test our products on his own responsibility. Extensive research and development is ongoing, which is why m4p reserves the right to change the information, specifications and data without notice.

Appendix B

Parameters of the failed build job

Table B.1: Full DoE combinations of support specimens' parameters

Specimen ID	ttl [μm]	z [nr of layers]	v [mm/s]	P_L[W]	P[%]	Volumetric energy density [J/mm^3]
1	150	0	700	300	75	85.71
2	150	0	1300	260	65	40.00
3	400	0	1000	300	75	60.00
4	400	7	1000	300	75	60.00
5	400	7	700	260	65	74.29
6	150	0	1300	340	85	52.31
7	150	0	700	260	65	74.29
8	150	7	1300	300	75	46.15
9	400	7	1300	260	65	40.00
10	400	7	1300	340	85	52.31
11	400	7	1300	300	75	46.15
12	150	7	1000	260	65	52.00
13	400	7	700	300	75	85.71
14	150	0	1000	340	85	68.00
15	400	0	700	300	75	85.71
16	150	7	700	300	75	85.71
17	150	7	1300	260	65	40.00
18	400	0	700	260	65	74.29
19	150	7	700	260	65	74.29
20	150	0	1000	260	65	52.00
21	400	0	1300	260	65	40.00
22	400	0	1300	340	85	52.31
23	150	7	700	340	85	97.14
24	150	0	1000	300	75	60.00
25	150	7	1000	300	75	60.00
26	400	0	1000	260	65	52.00
27	400	0	1000	340	85	68.00
28	150	0	1300	300	75	46.15
29	400	0	700	340	85	97.14

30	400	7	1000	260	65	52.00
31	150	0	700	340	85	97.14
32	400	0	1300	300	75	46.15
33	400	7	1000	340	85	68.00
34	150	7	1300	340	85	52.31
35	150	7	1000	340	85	68.00
36	400	7	700	340	85	97.14

Table B.2: Full DoE combinations of density specimens

Specimen ID	v [mm/s]	P_L[W]	P_L[%]	Volumetric energy density [J/mm^3]
37	1000	260	65	52.00
38	1000	300	75	60.00
39	700	340	85	97.14
40	1300	340	85	52.31
41	1300	260	65	40.00
42	700	300	75	85.71
43	1000	340	85	68.00
44	1300	300	75	46.15
45	700	260	65	74.29

Appendix C

Microscopic images of the 9 areas of the section of each density specimen

Specimen 37: v_s=1150 mm/s; P_L=260 W

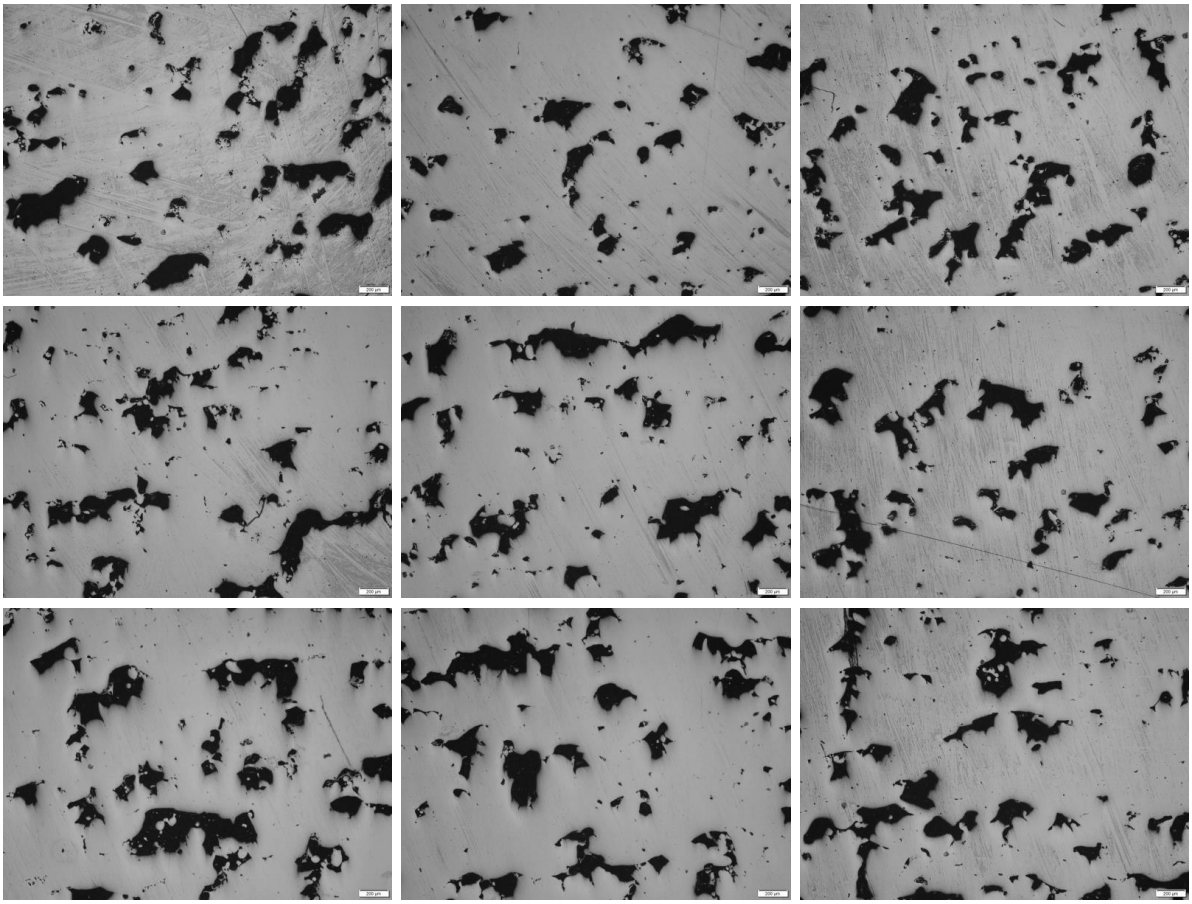

Specimen 38: v_s=1150 mm/s; P_L=300 W

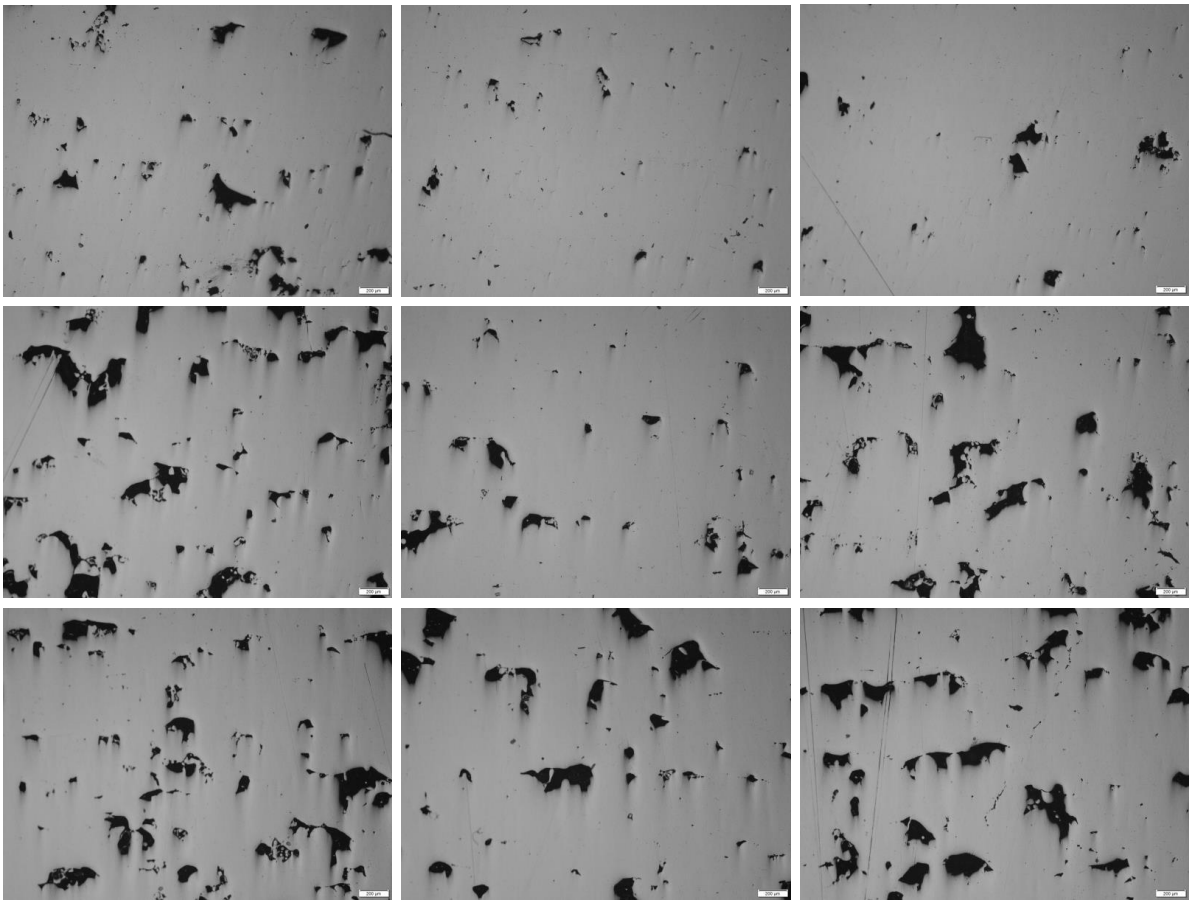

Specimen 39: v_s=900 mm/s; P_L=340 W

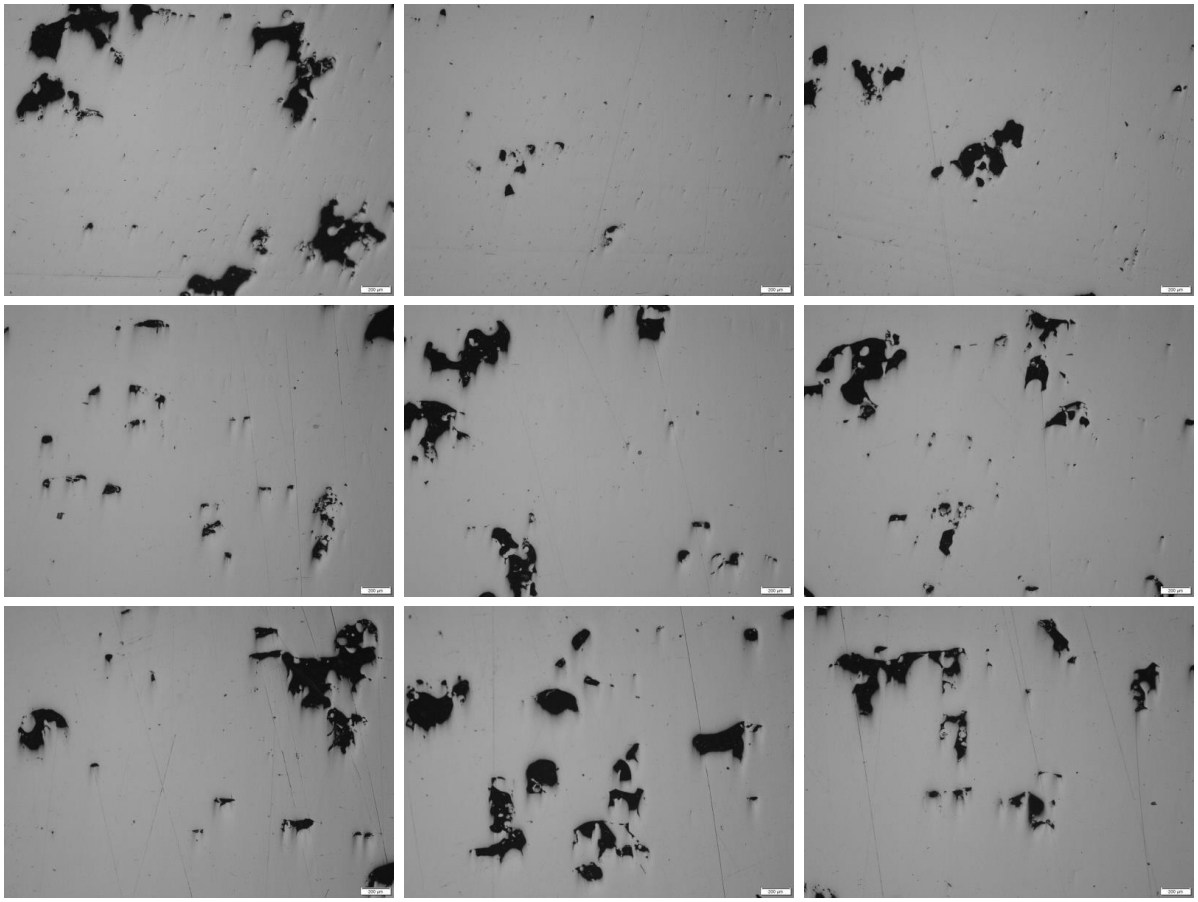

Specimen 40: v_s=1400 mm/s; P_L=340 W

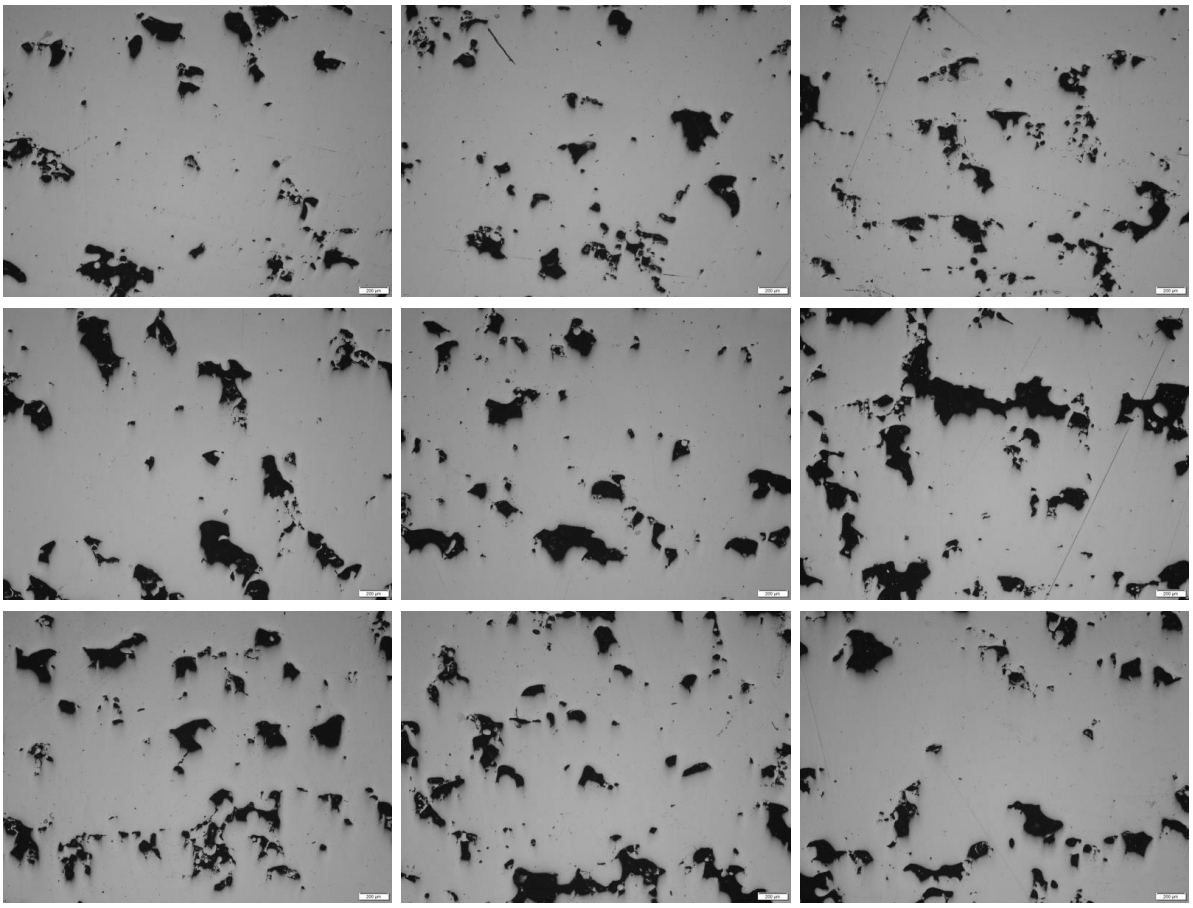

Specimen 41: v_s=1400 mm/s; P_L=260 W

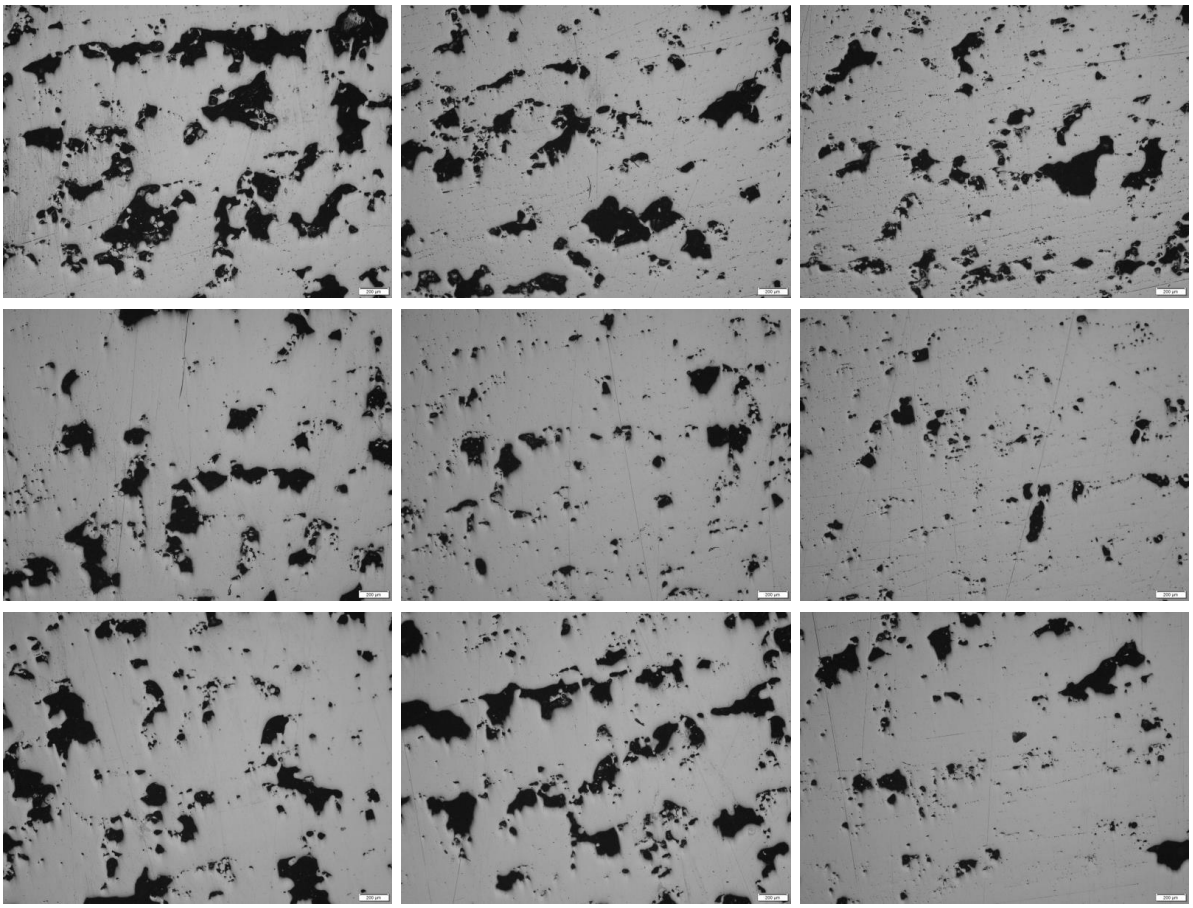

Specimen 42: v_s=900 mm/s; P_L=300 W

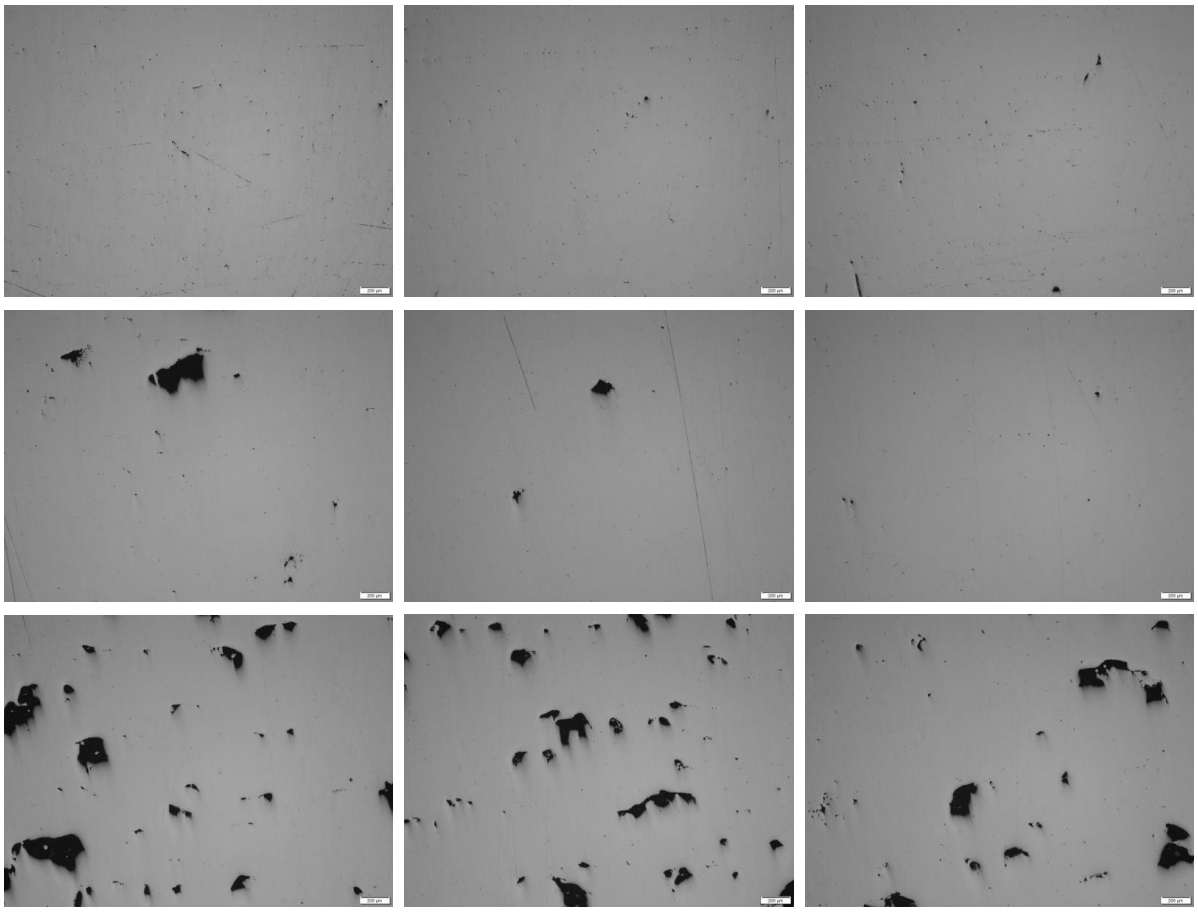

Specimen 43: v_s=1150 mm/s; P_L=340 W

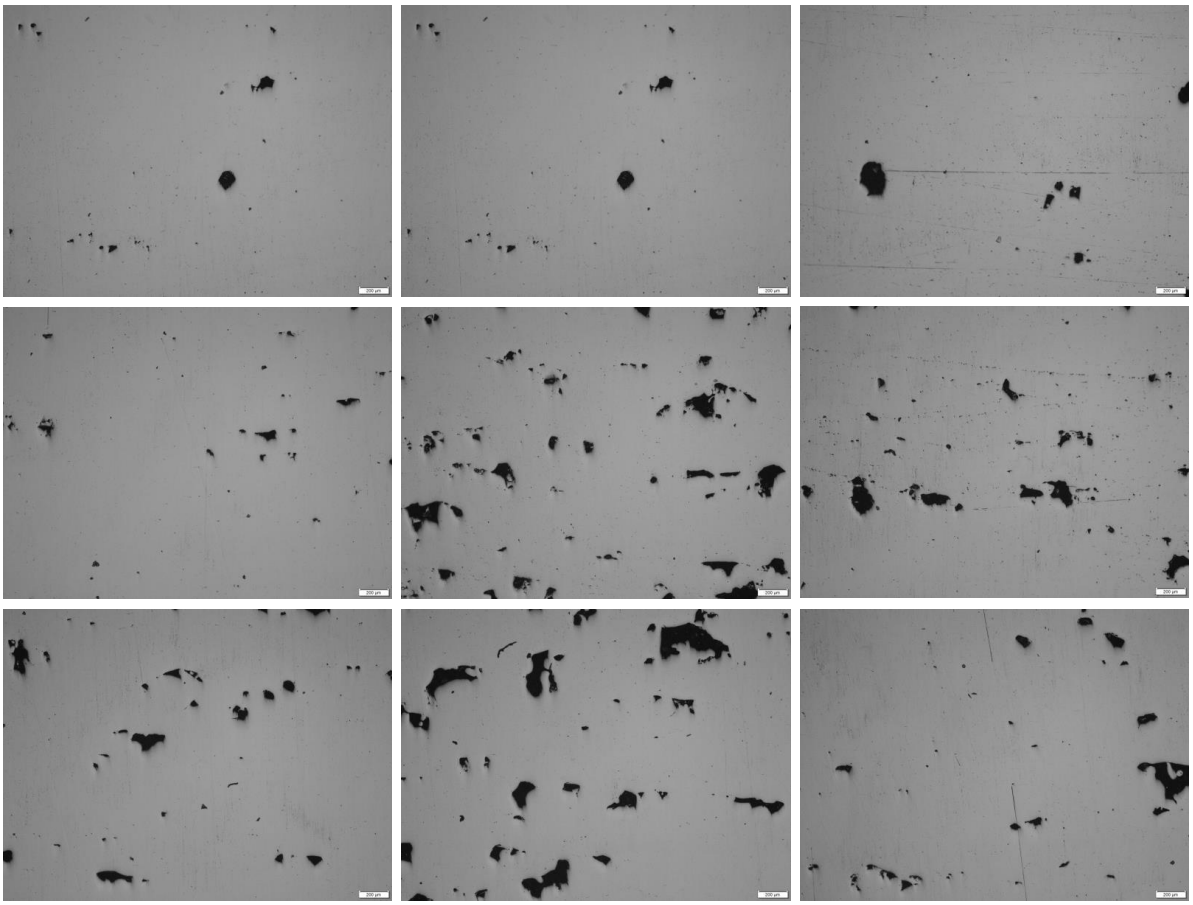

Specimen 45: v_s=900 mm/s; P_L=260 W

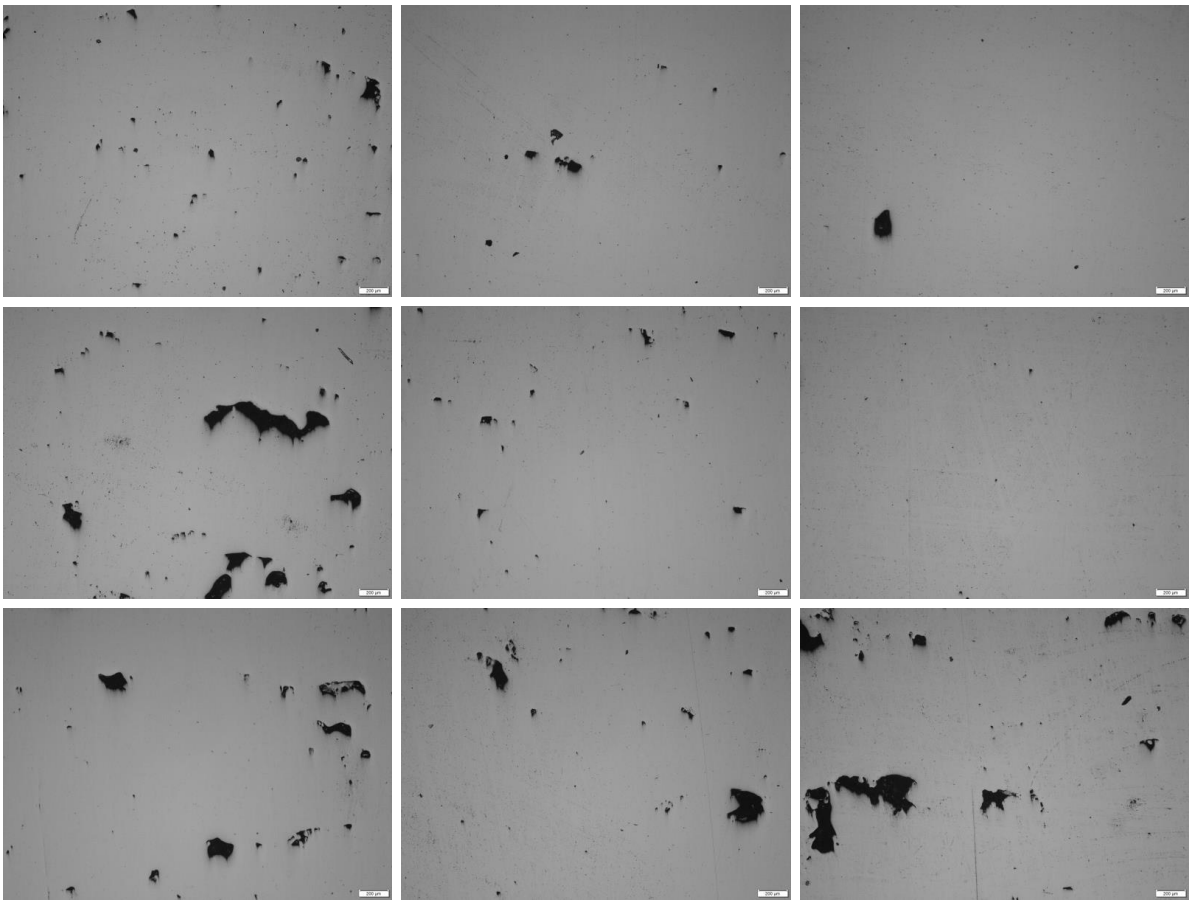

Appendix D

Stress-Strain curves obtained for each specimen, from the tensile tests

Table D.1: Classification of specimens according to the support geometry and chart labeling

Support Geometry	ttl [μm]	z-offset [nr. layers]	Legend
A	150	0	
B	400	0	
C	400	7	
D	150	7	

Legend: Specimen ID (Support Geometry)

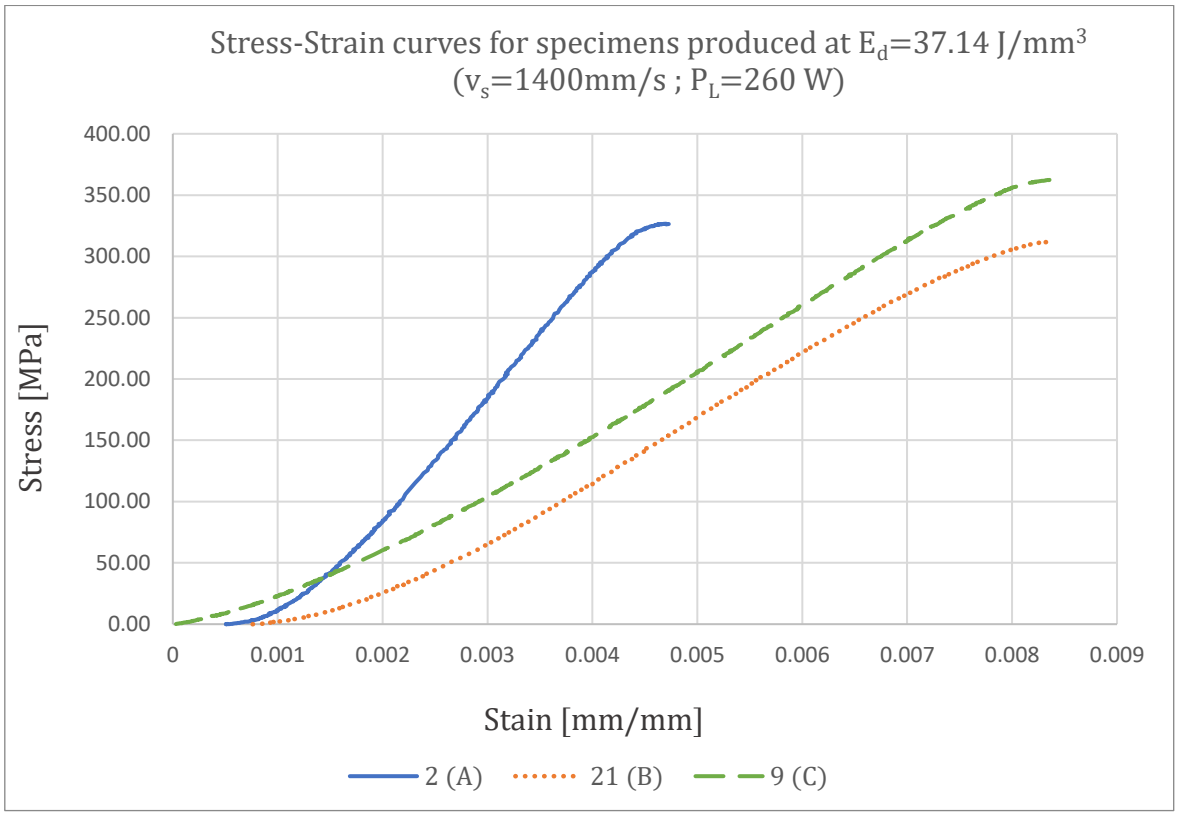

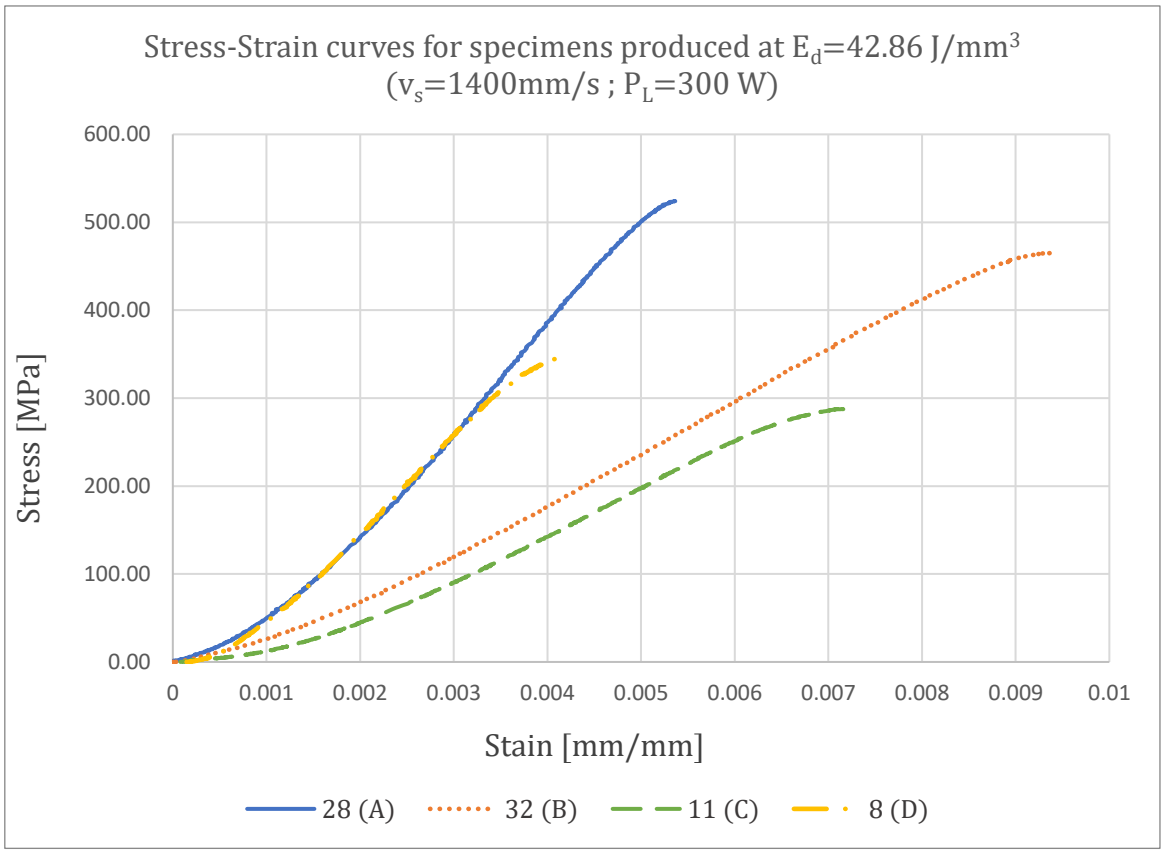

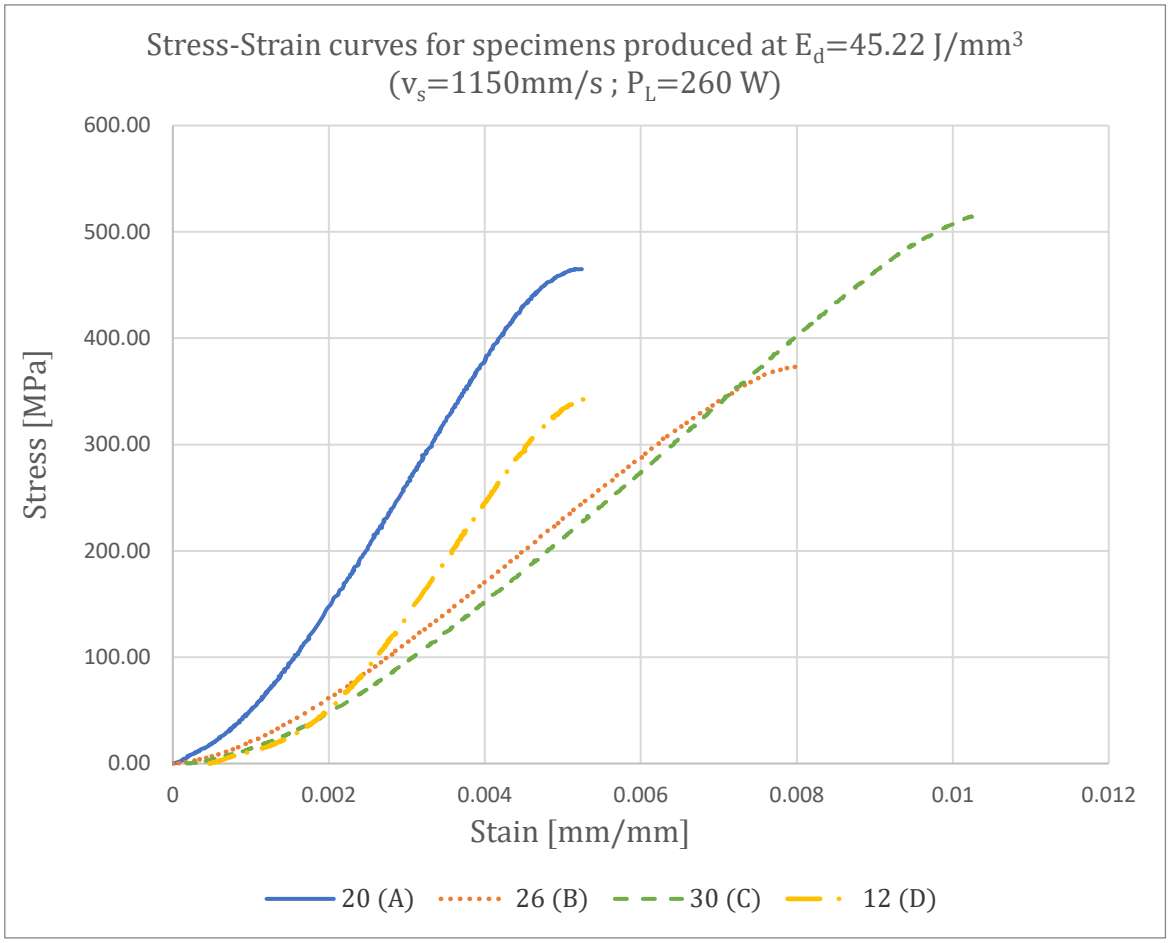
Stress-Strain curves for specimens produced at E_d=45.22 J/mm^3
(v_s=1150mm/s ; P_L=260 W)
Stress [MPa]
600.00
500.00
400.00
300.00
200.00
100.00
0.00
0
0.002
0.004
0.006
0.008
0.01
0.012
Stain [mm/mm]
20 (A)
26 (B)
30 (C)
12 (D)

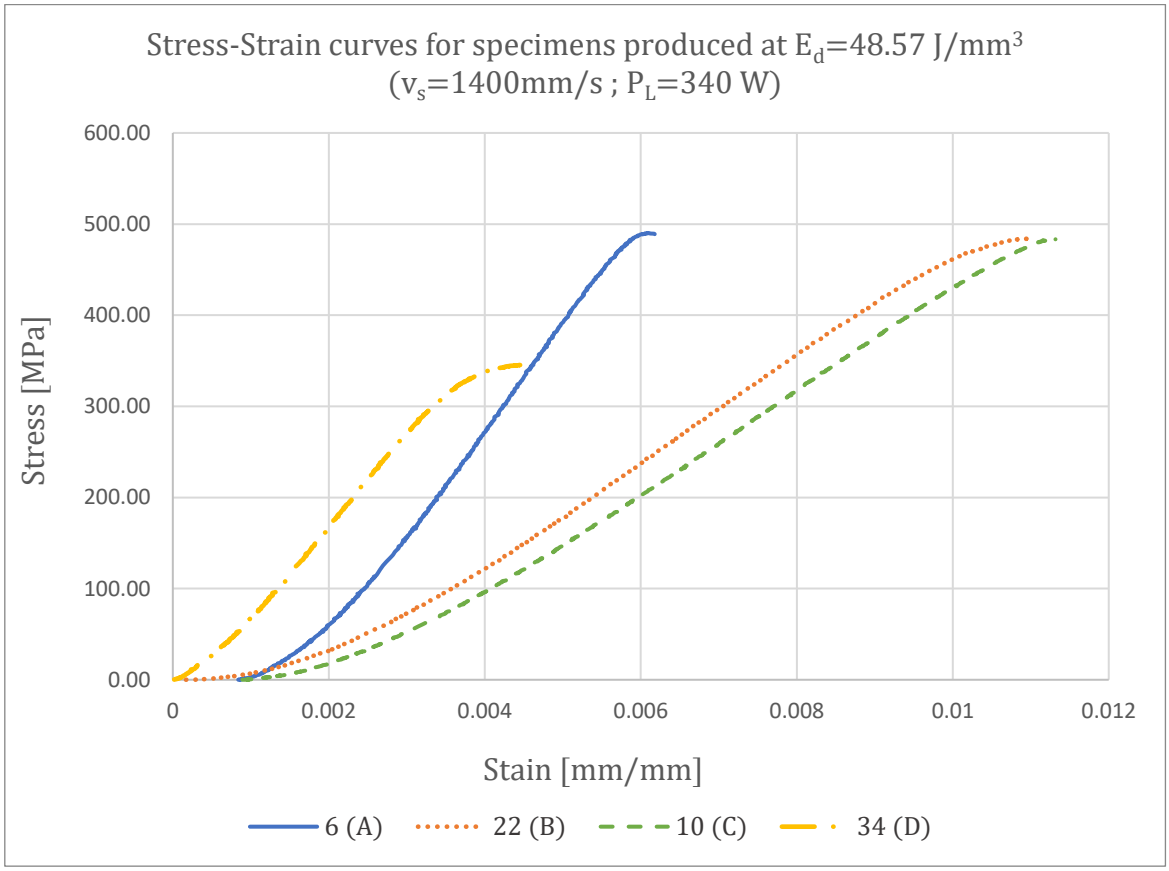
Stress-Strain curves for specimens produced at E_d=48.57 J/mm^3
(v_s=1400mm/s ; P_L=340 W)
Stress [MPa]
600.00
500.00
400.00
300.00
200.00
100.00
0.00
0
0.002
0.004
0.006
0.008
0.01
0.012
Stain [mm/mm]
6 (A)
22 (B)
10 (C)
34 (D)

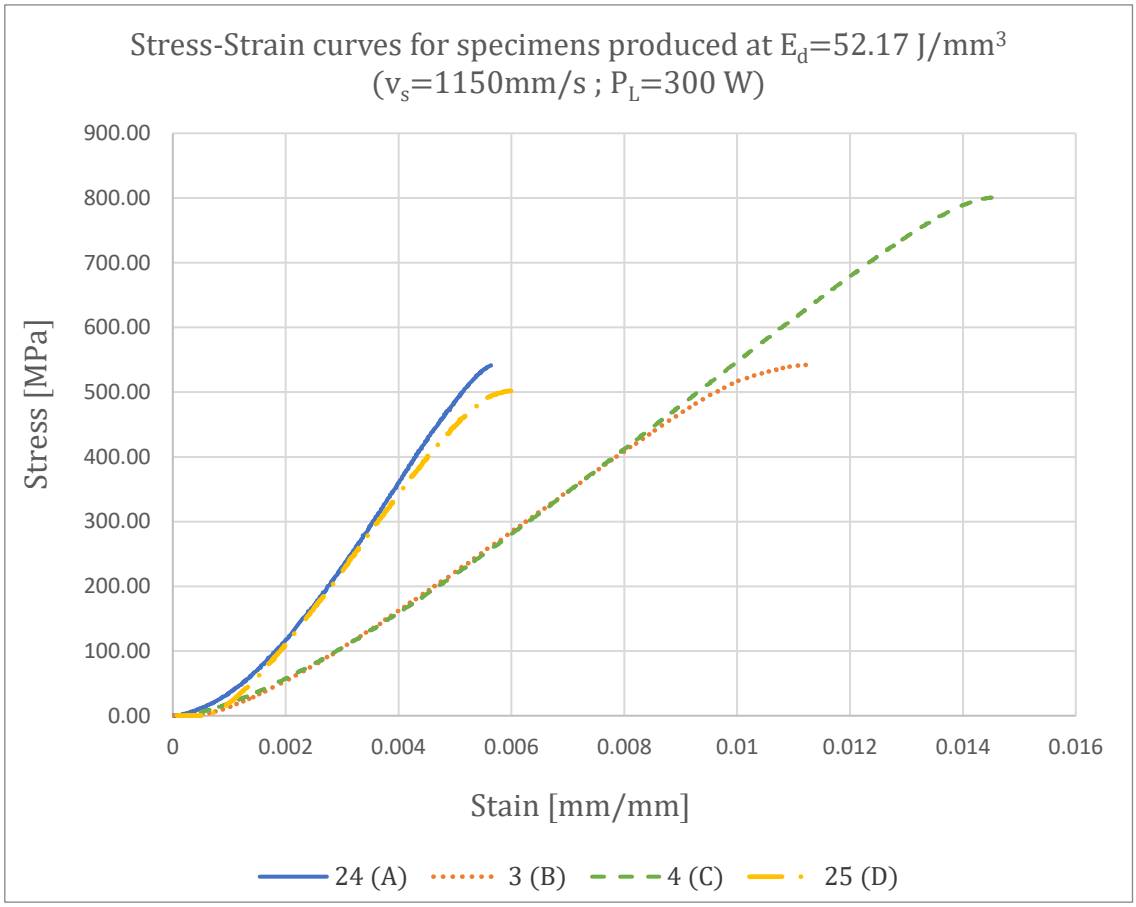
Stress-Strain curves for specimens produced at E_d=52.17 J/mm^3
(v_s=1150mm/s ; P_L=300 W)
Stress [MPa]
900.00
800.00
700.00
600.00
500.00
400.00
300.00
200.00
100.00
0.00
0
0.002
0.004
0.006
0.008
0.01
0.012
0.014
0.016
Stain [mm/mm]
24 (A)
3 (B)
4 (C)
25 (D)

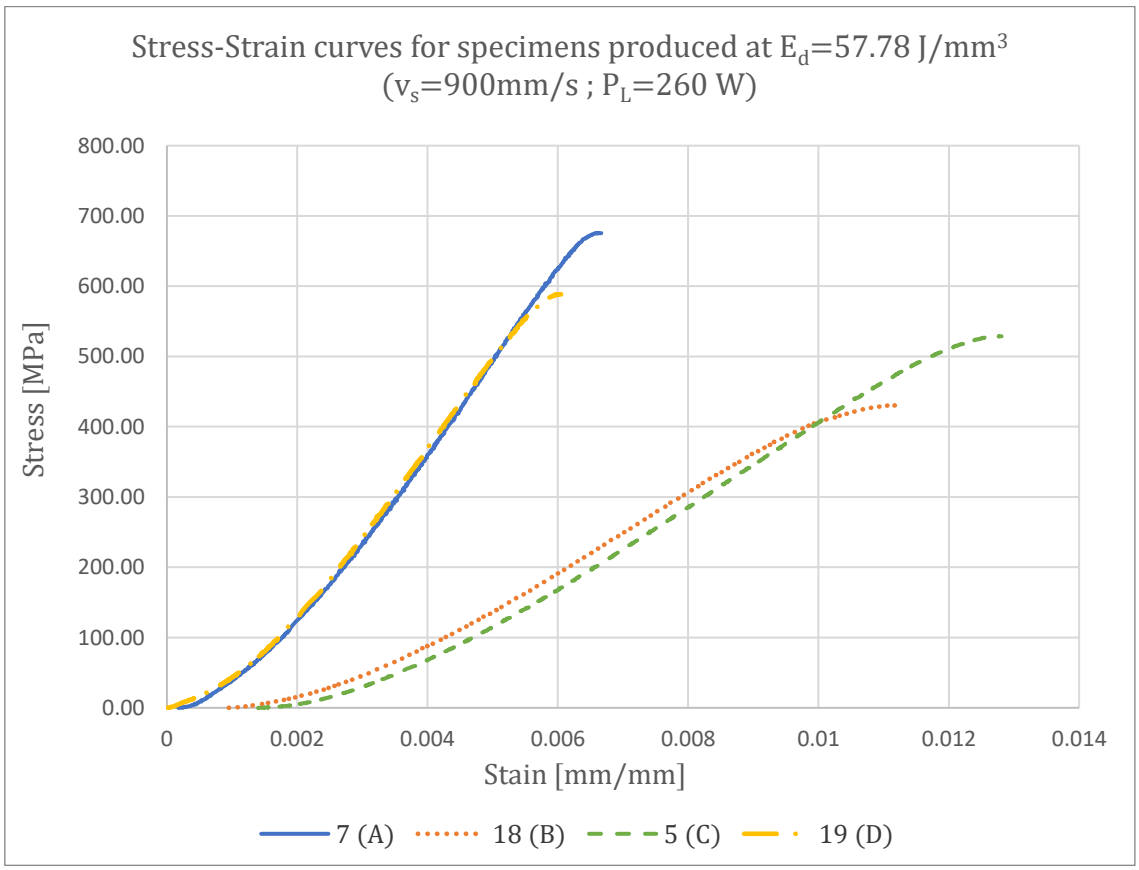
Stress-Strain curves for specimens produced at E_d=57.78 J/mm^3
(v_s=900mm/s ; P_L=260 W)
Stress [MPa]
800.00
700.00
600.00
500.00
400.00
300.00
200.00
100.00
0.00
0
0.002
0.004
0.006
0.008
0.01
0.012
0.014
Stain [mm/mm]
7 (A)
18 (B)
5 (C)
19 (D)

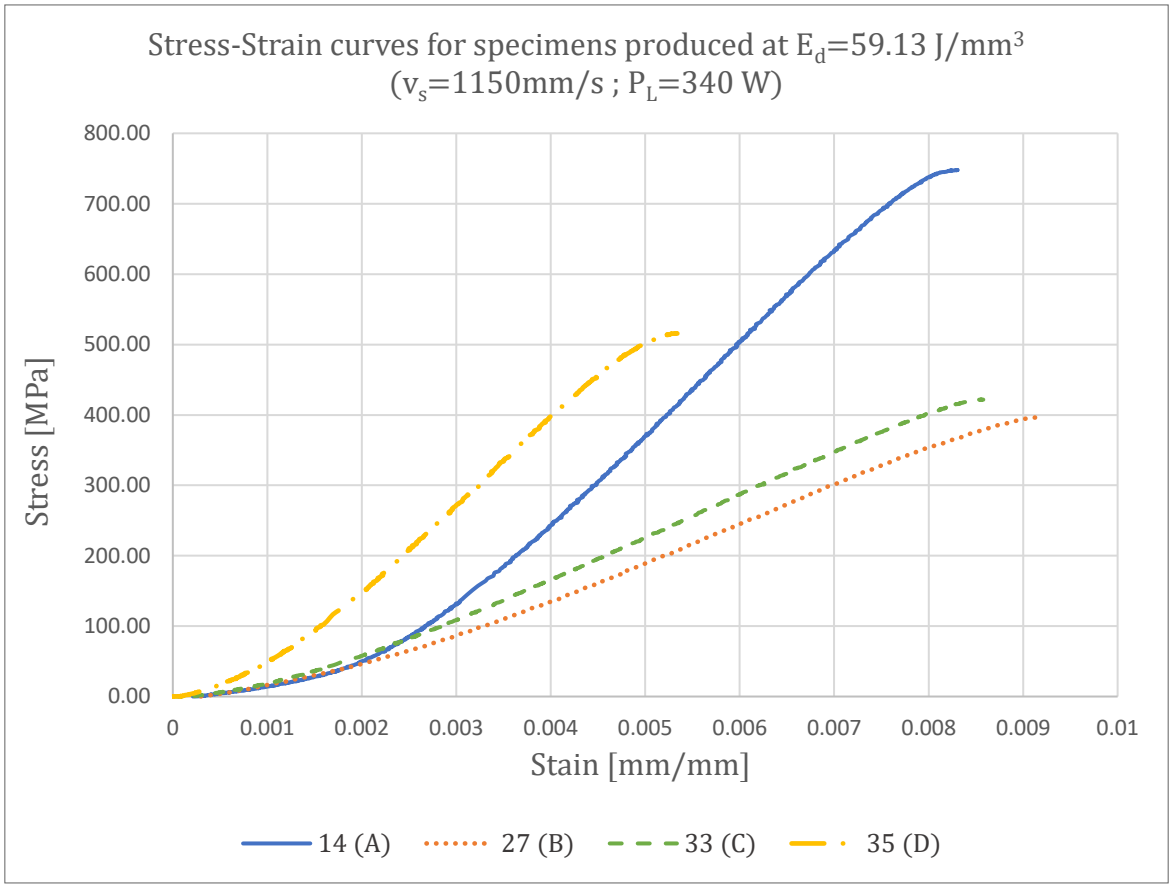
Stress-Strain curves for specimens produced at E_d=59.13 J/mm^3
(v_s=1150mm/s ; P_L=340 W)
Stress [MPa]
800.00
700.00
600.00
500.00
400.00
300.00
200.00
100.00
0.00
0
0.001
0.002
0.003
0.004
0.005
0.006
0.007
0.008
0.009
0.01
Stain [mm/mm]
14 (A)
27 (B)
33 (C)
35 (D)

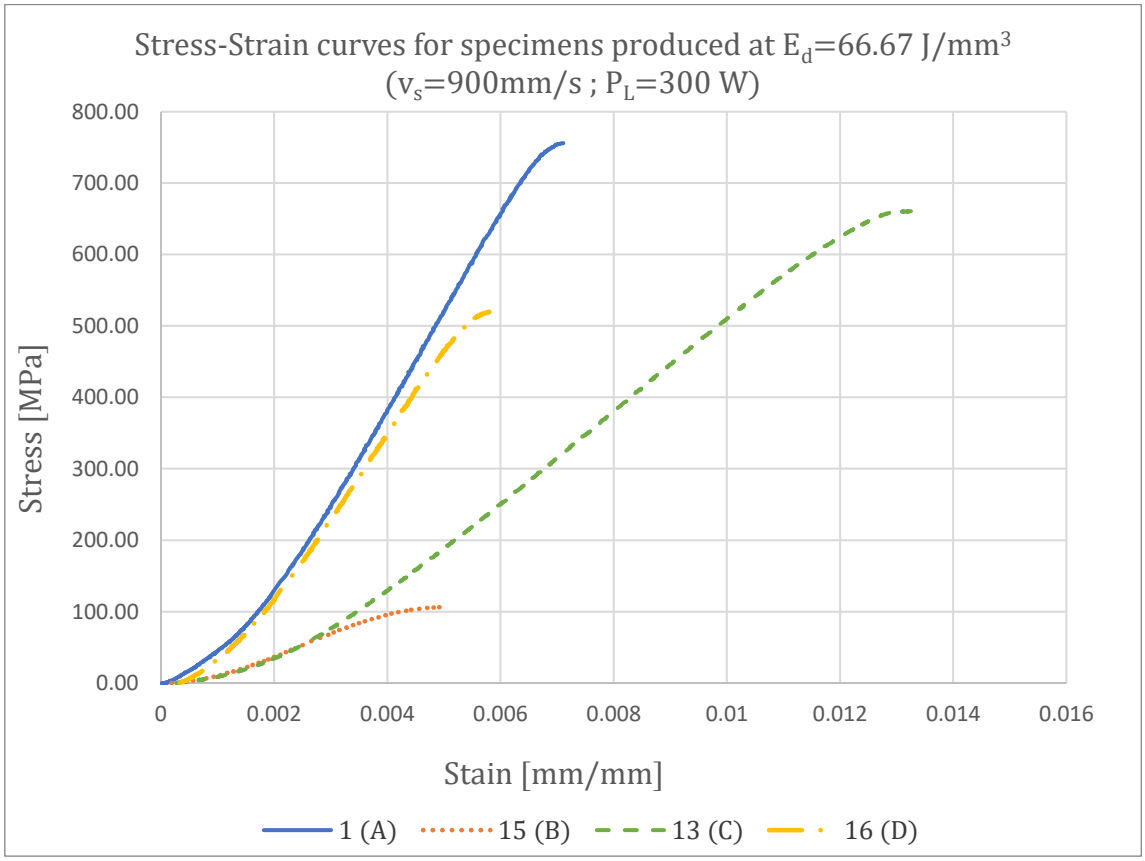
Stress-Strain curves for specimens produced at E_d=66.67 J/mm^3
(v_s=900mm/s ; P_L=300 W)
Stress [MPa]
800.00
700.00
600.00
500.00
400.00
300.00
200.00
100.00
0.00
0
0.002
0.004
0.006
0.008
0.01
0.012
0.014
0.016
Stain [mm/mm]
1 (A)
15 (B)
13 (C)
16 (D)

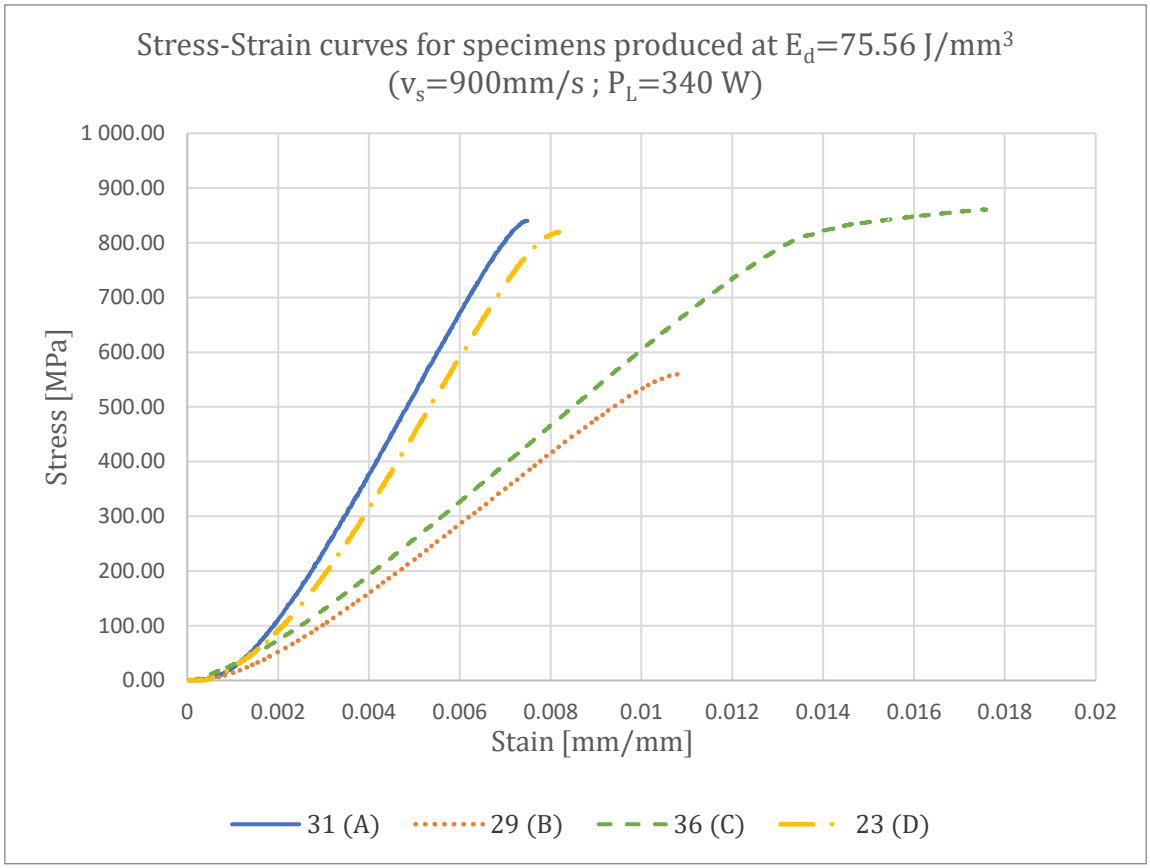
Stress-Strain curves for specimens produced at E_d=75.56 J/mm^3
(v_s=900mm/s ; P_L=340 W)
Stress [MPa]
1 000.00
900.00
800.00
700.00
600.00
500.00
400.00
300.00
200.00
100.00
0.00
0
0.002
0.004
0.006
0.008
0.01
0.012
0.014
0.016
0.018
0.02
Stain [mm/mm]
31 (A)
29 (B)
36 (C)
23 (D)

Appendix E

Microscopic pictures of the interface of the specimens before and after the tensile test

SPECIMEN	BEFORE TENSILE TEST	AFTER TENSILE TEST
1	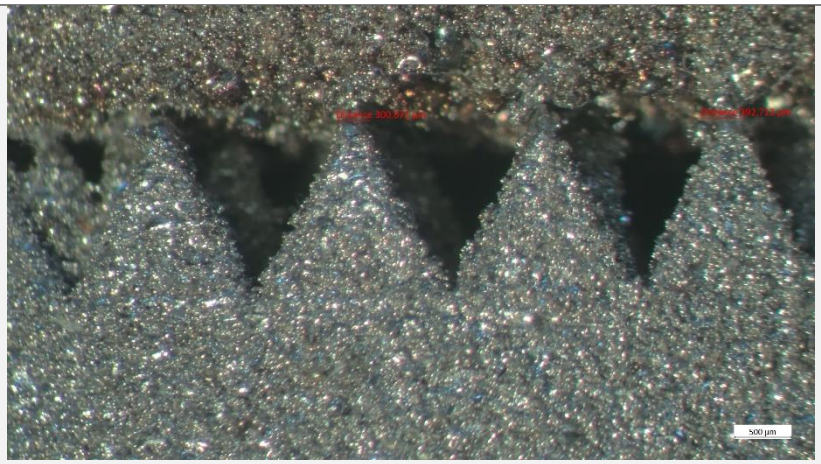	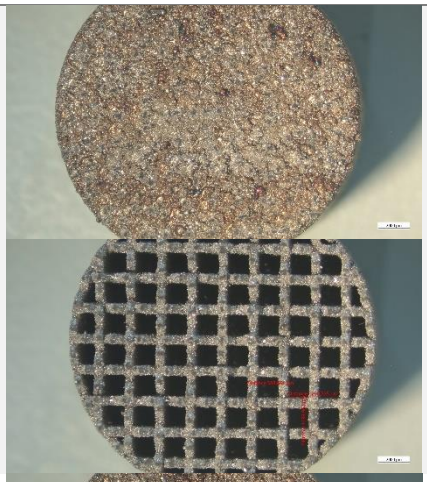
2	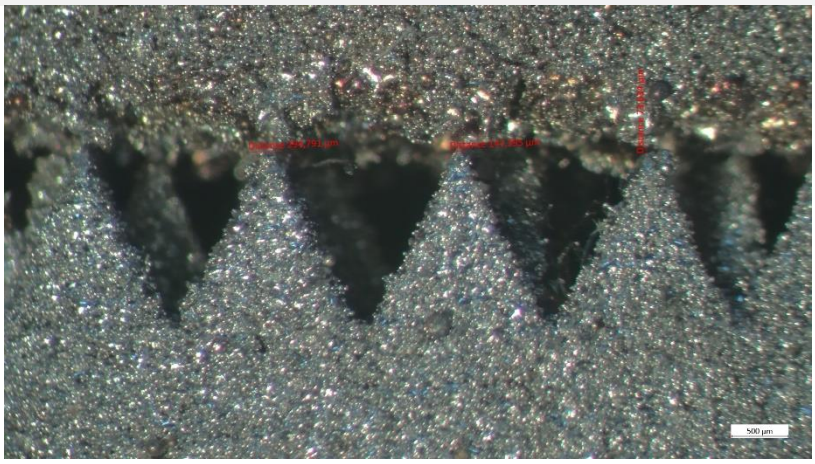	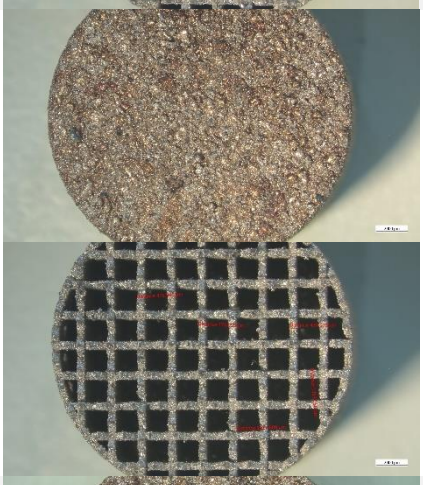
3	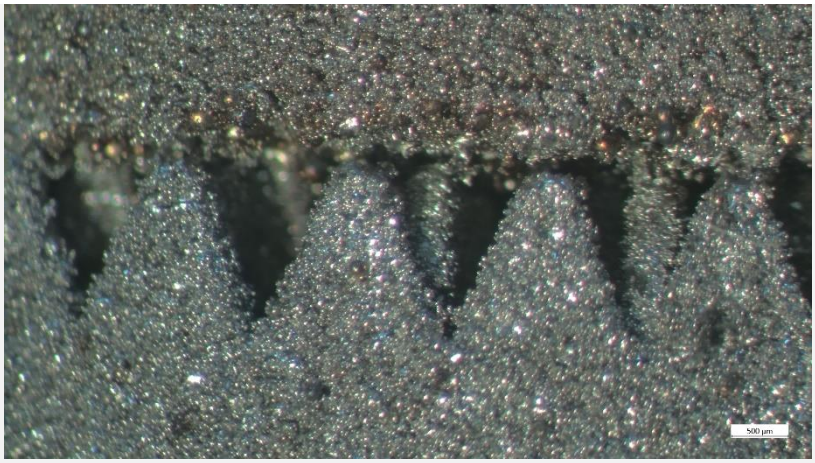	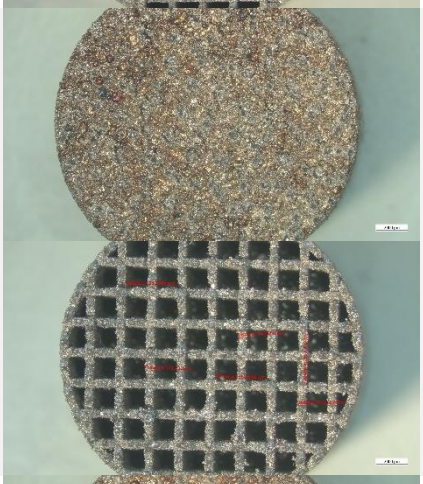
4	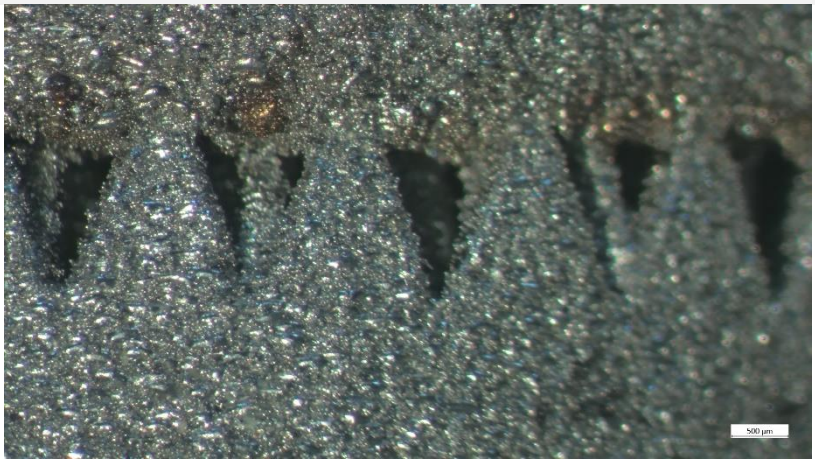	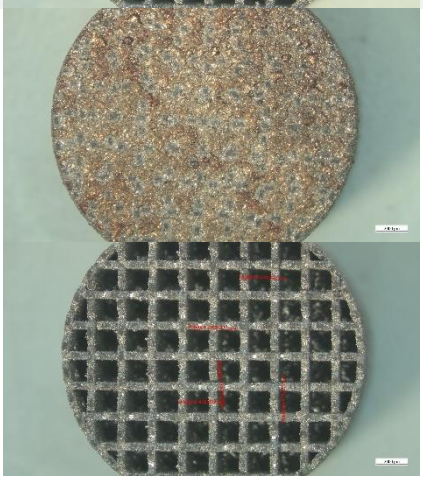

5		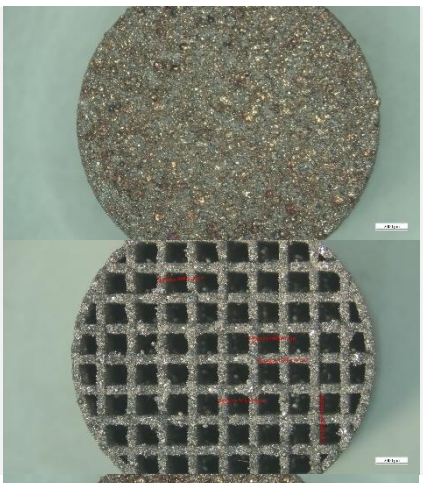
6	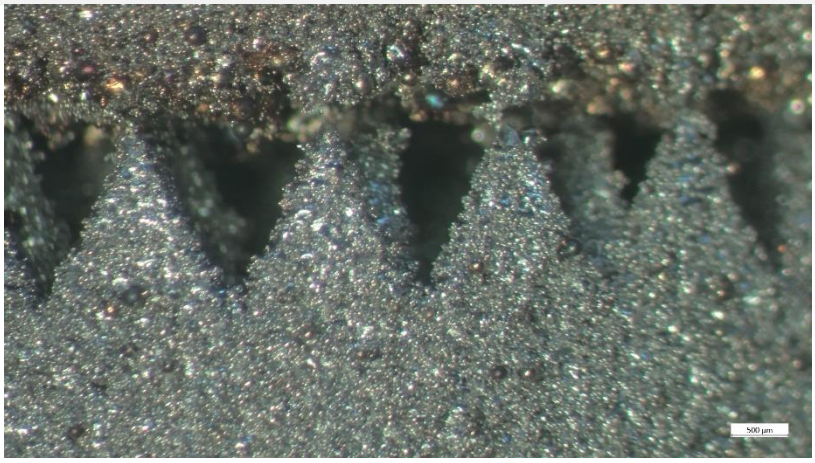	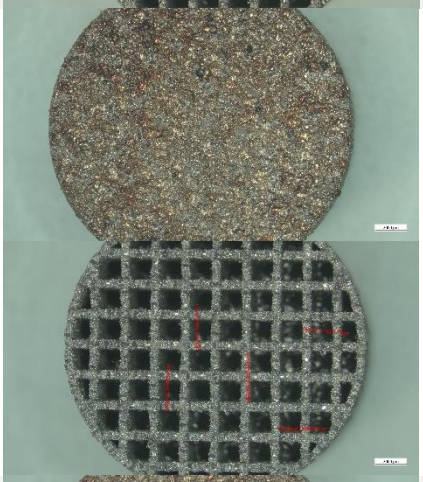
7		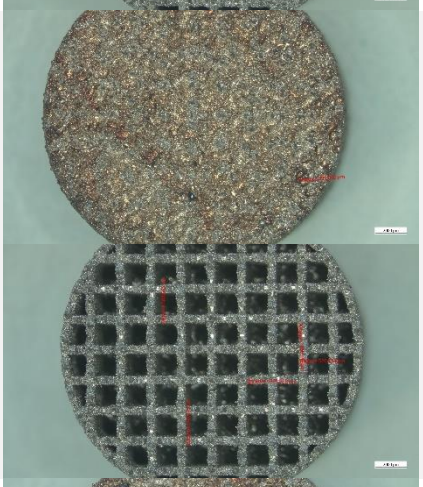
8	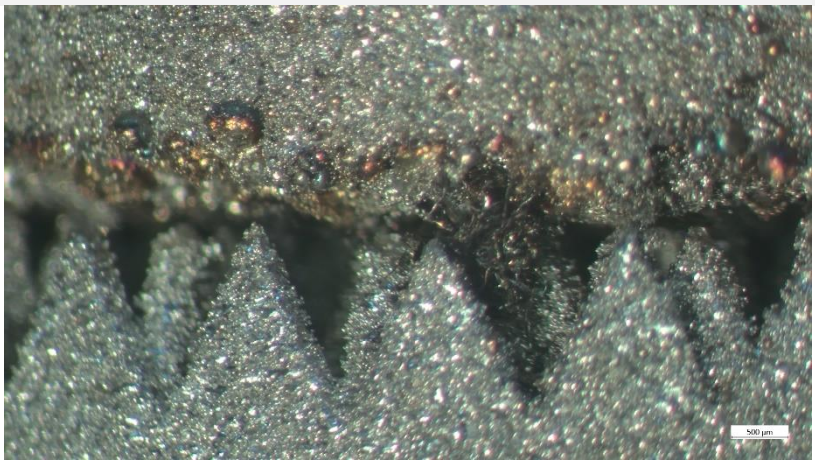	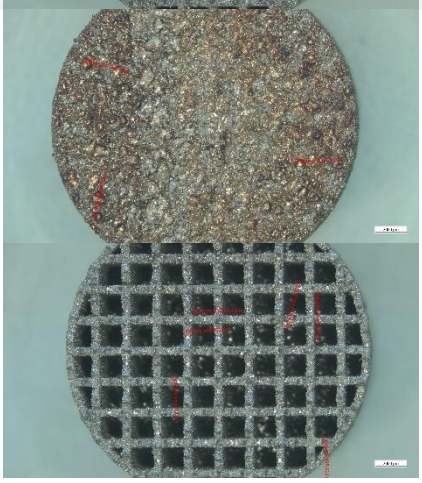

9	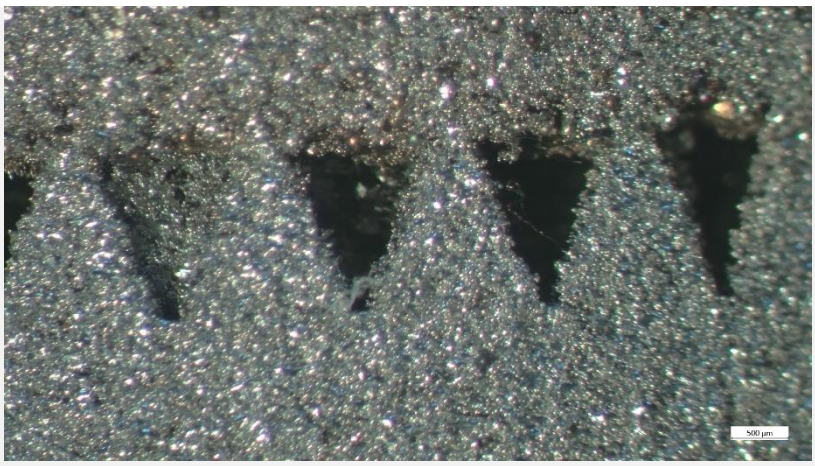	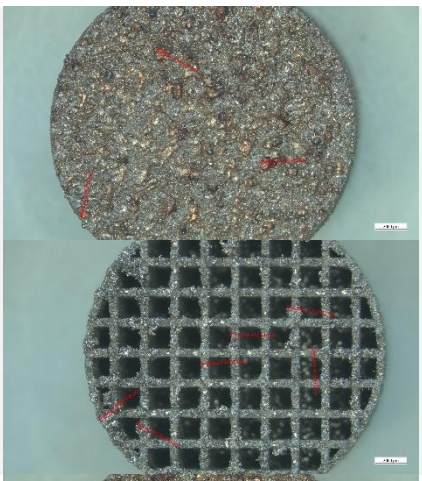
10	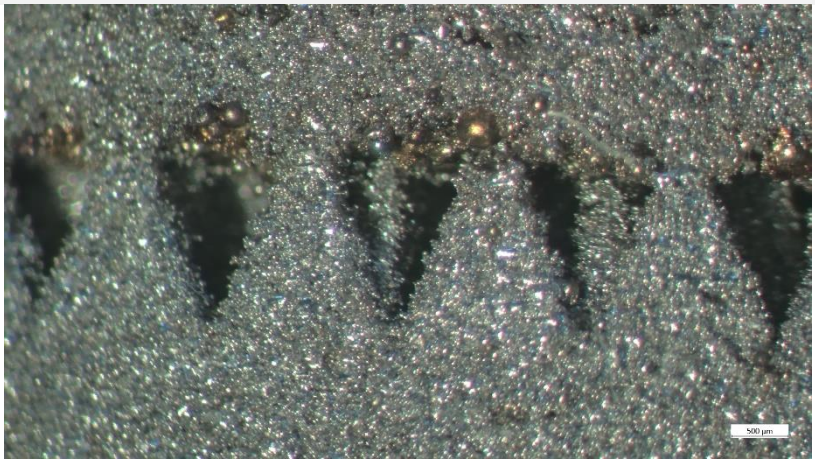	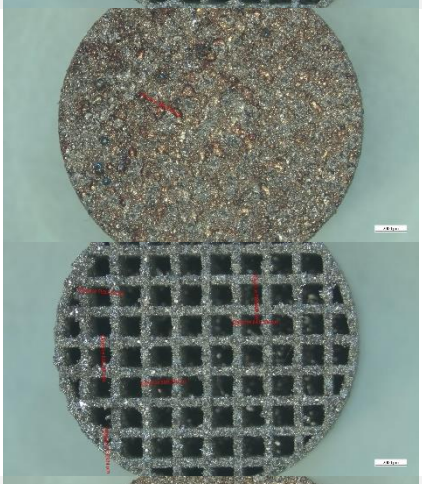
11	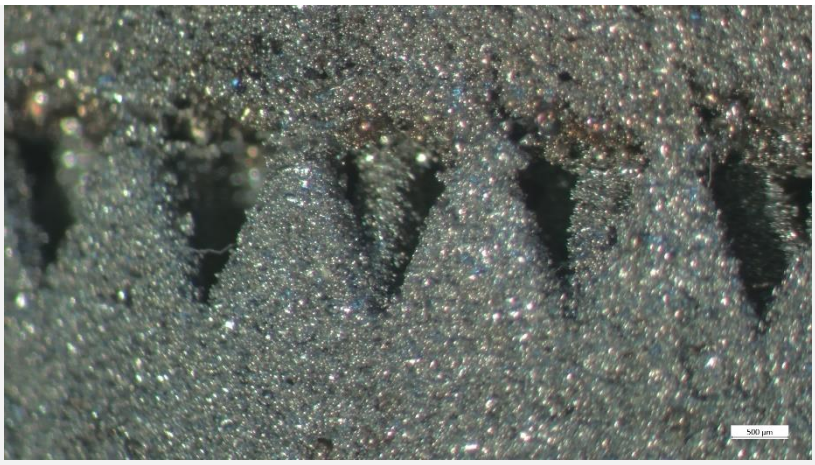	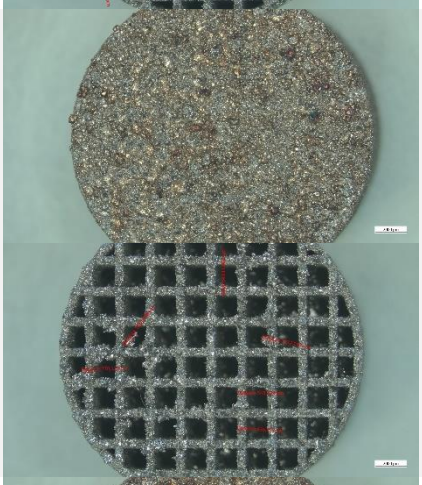
12	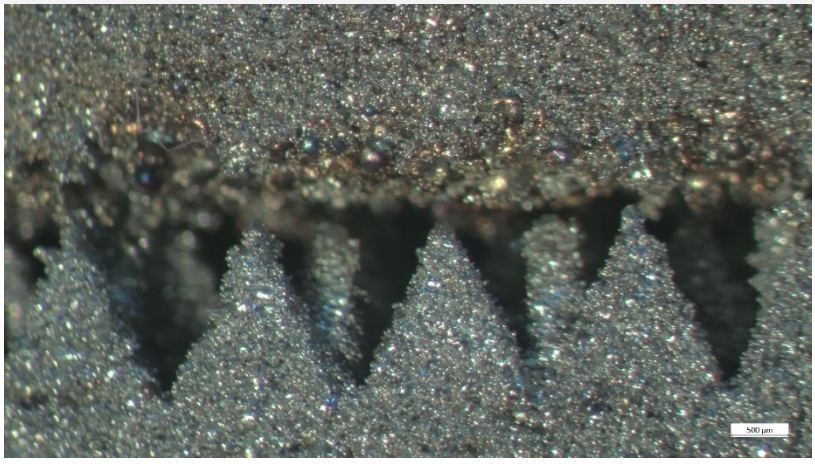	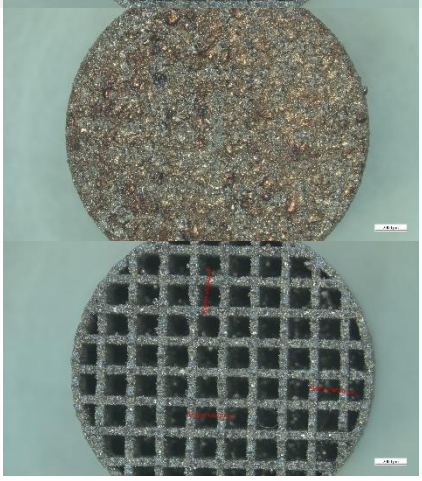

13

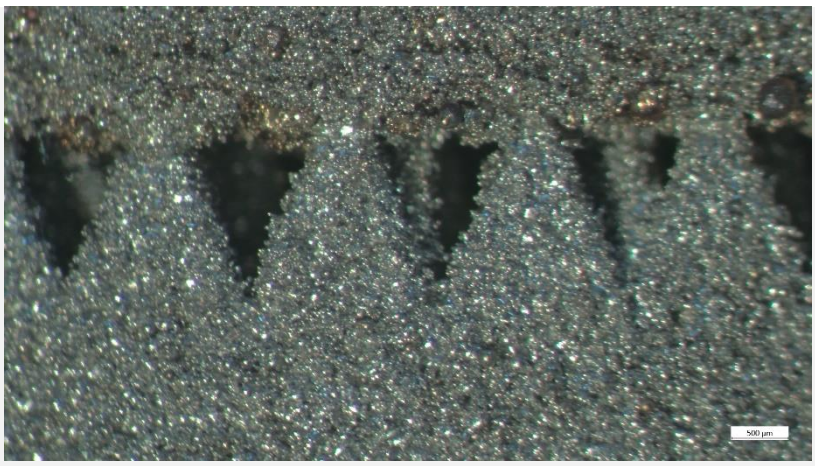

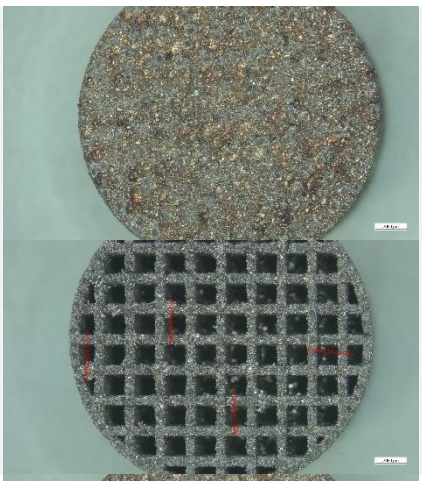

14

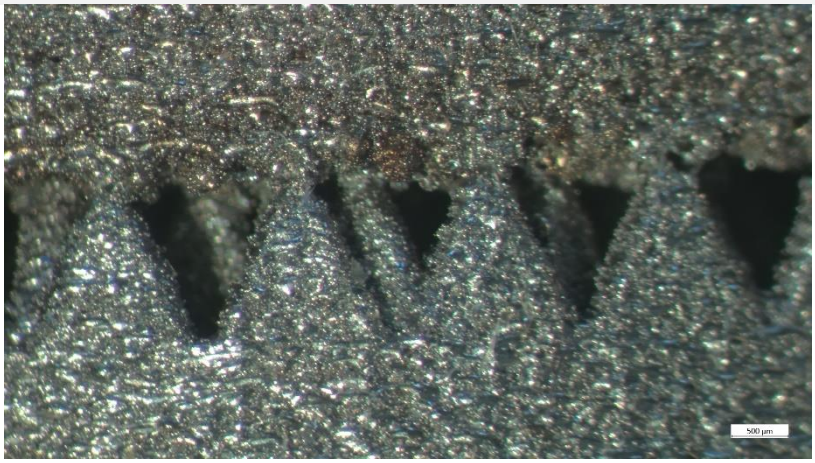

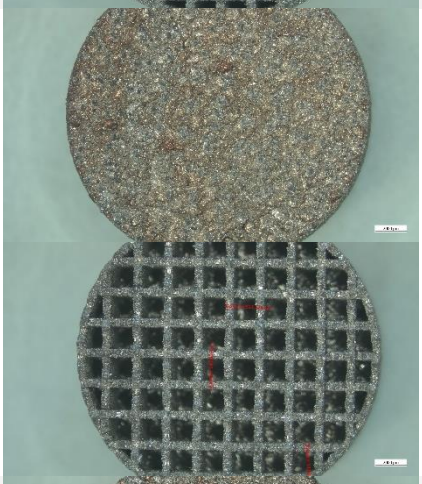

15

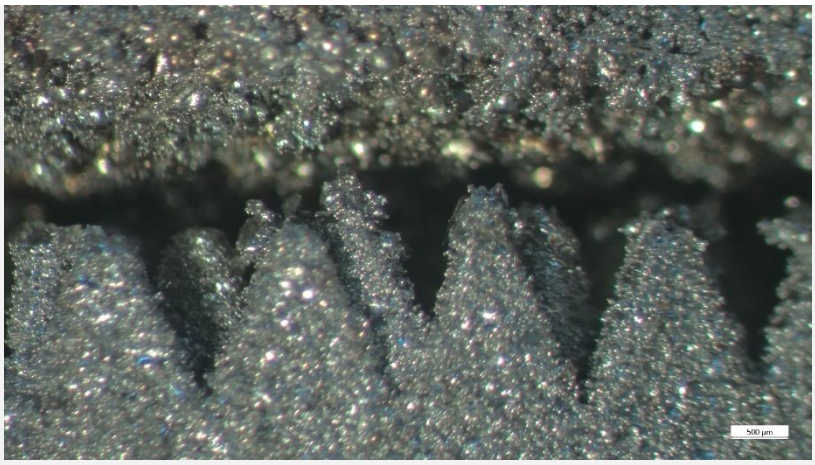

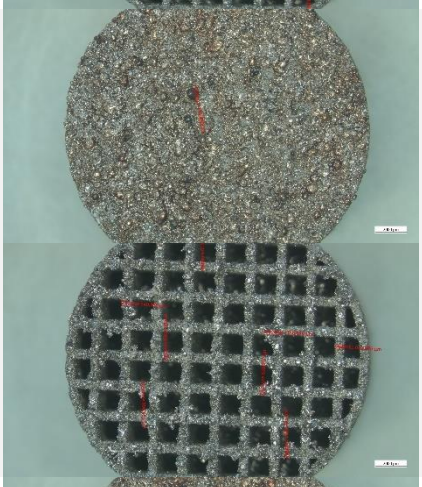

16

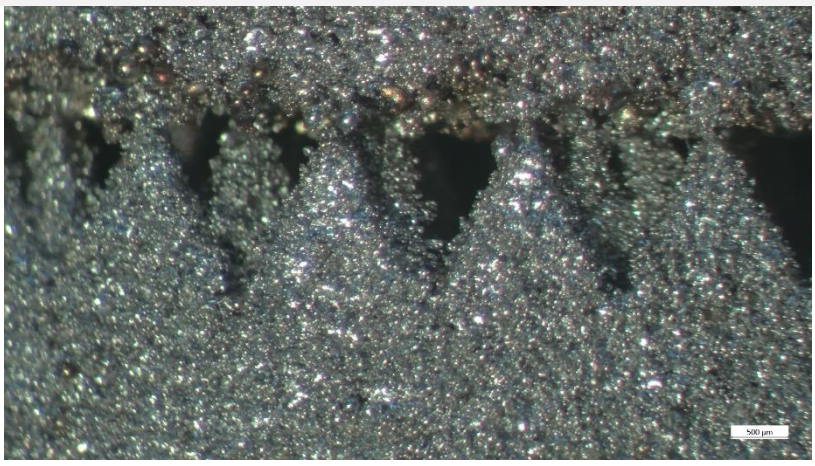

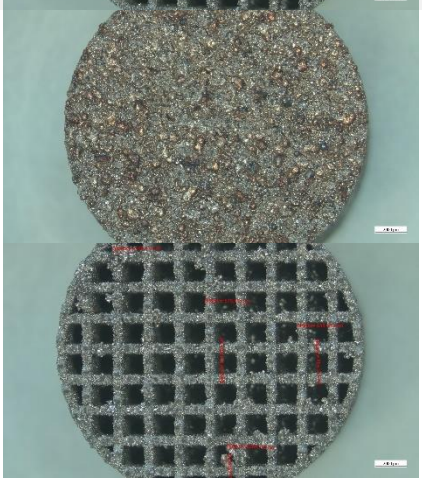

17

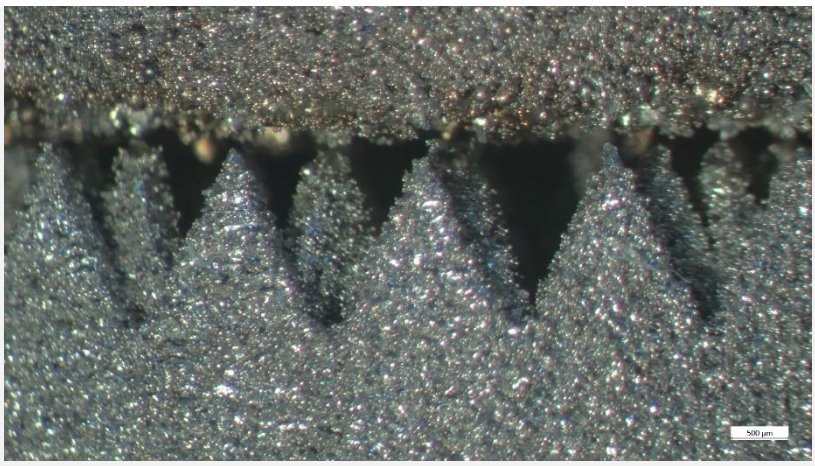

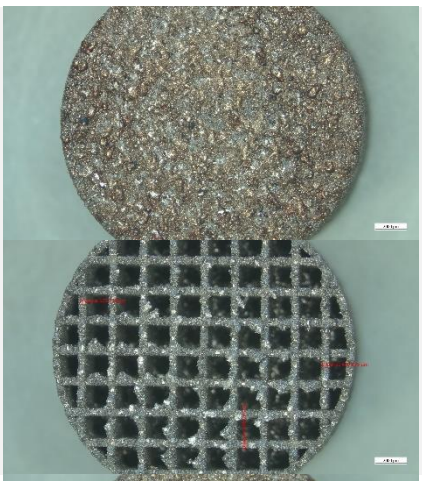

18

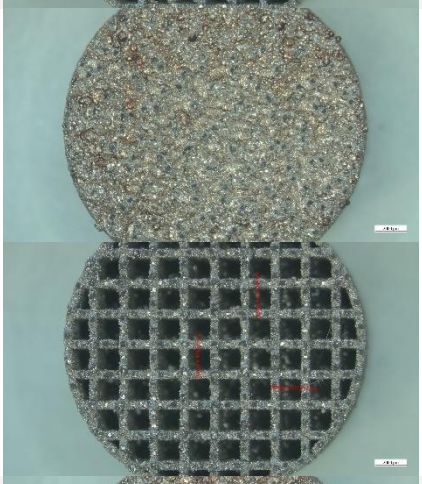

19

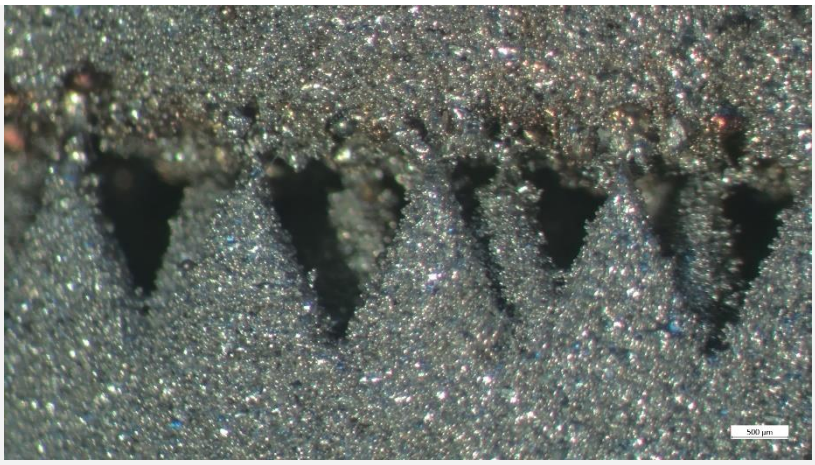

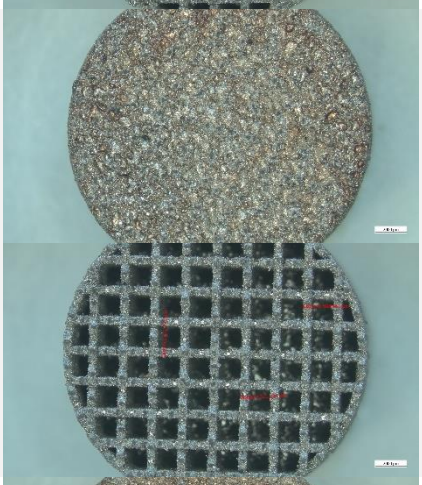

20

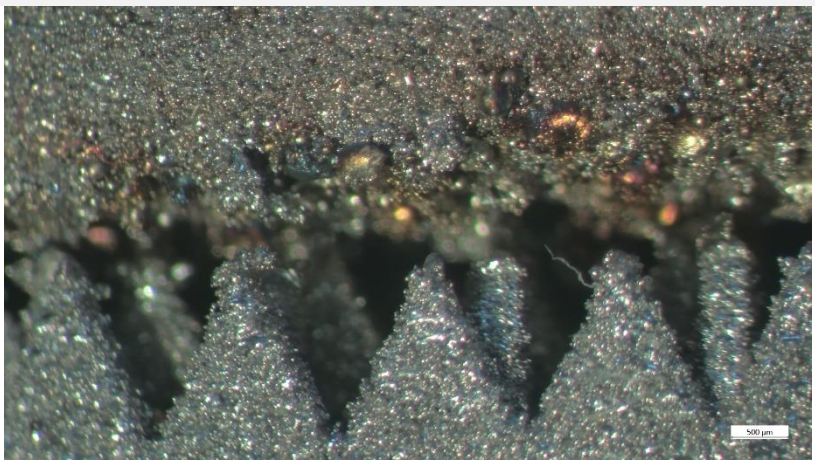

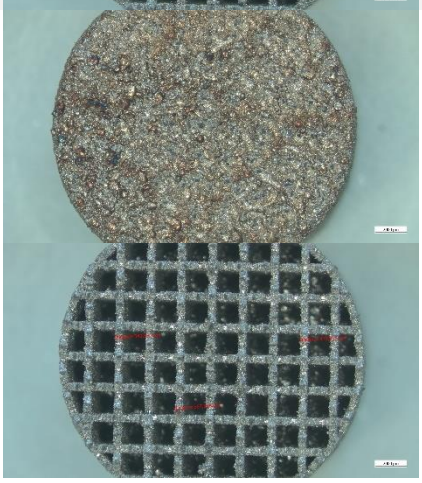

21

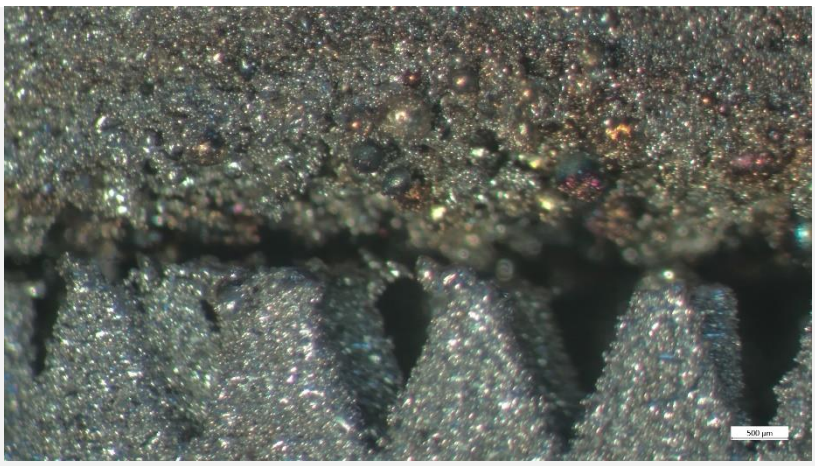

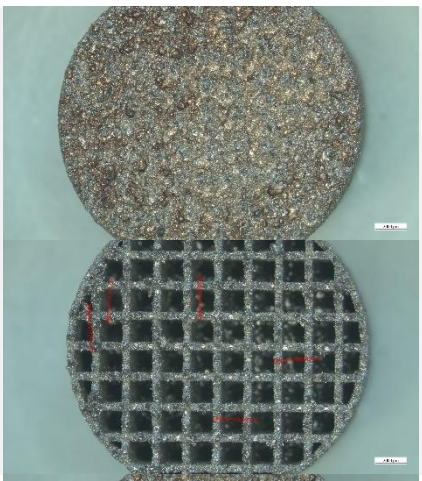

22

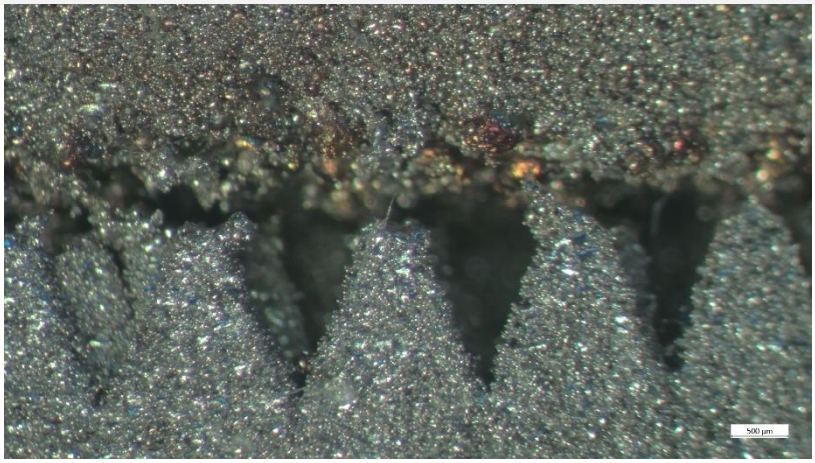

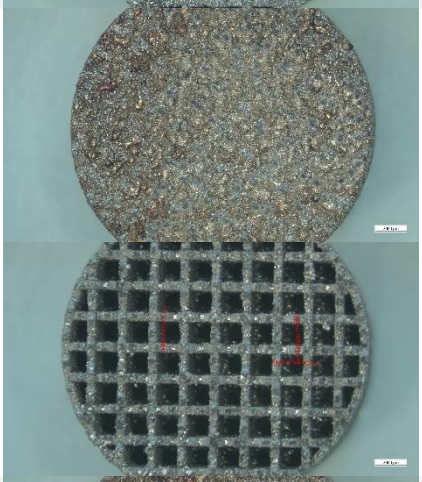

23

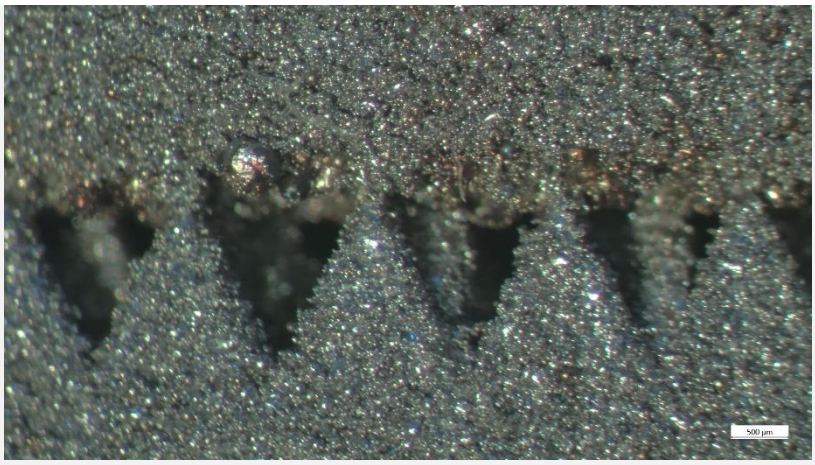

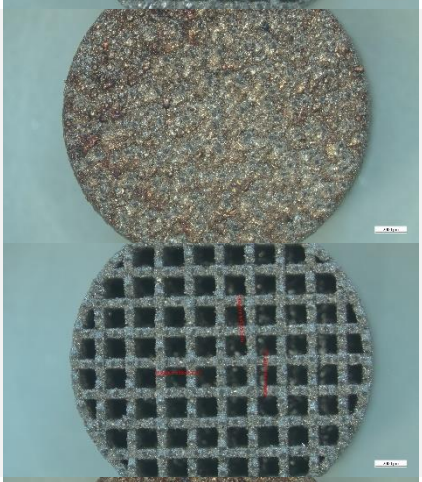

24

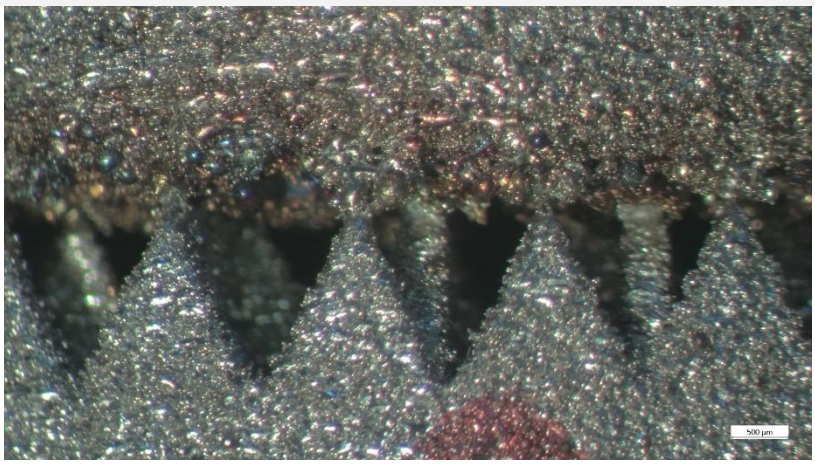

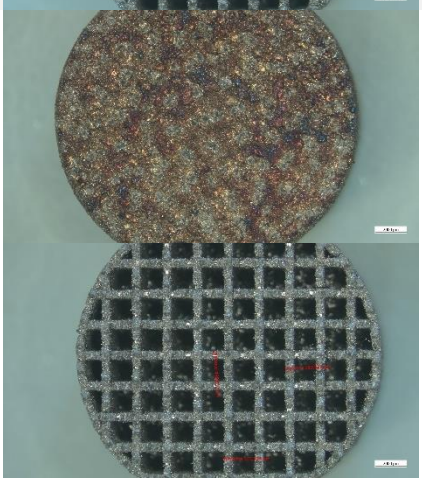

25

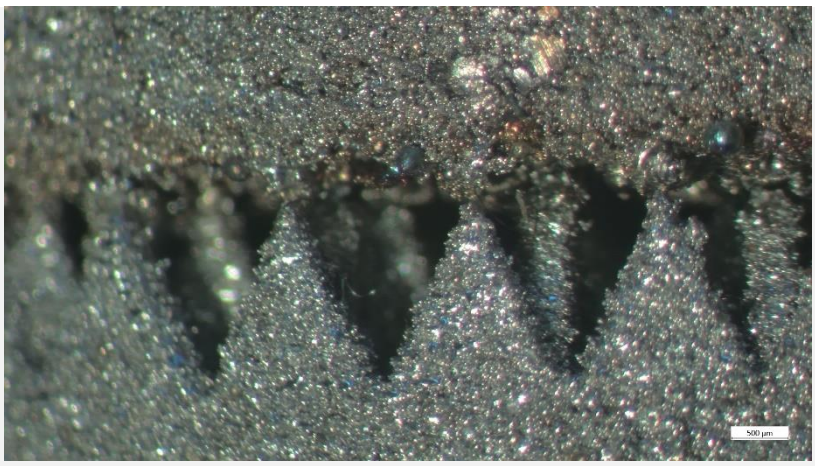

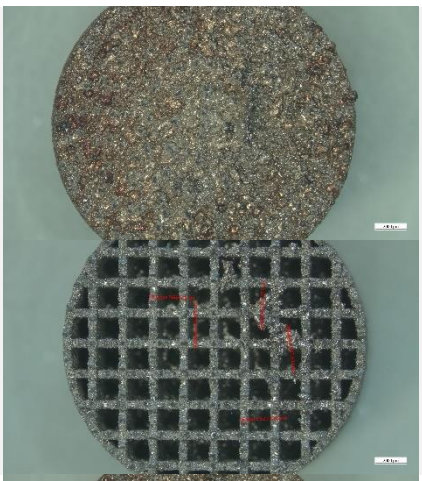

26

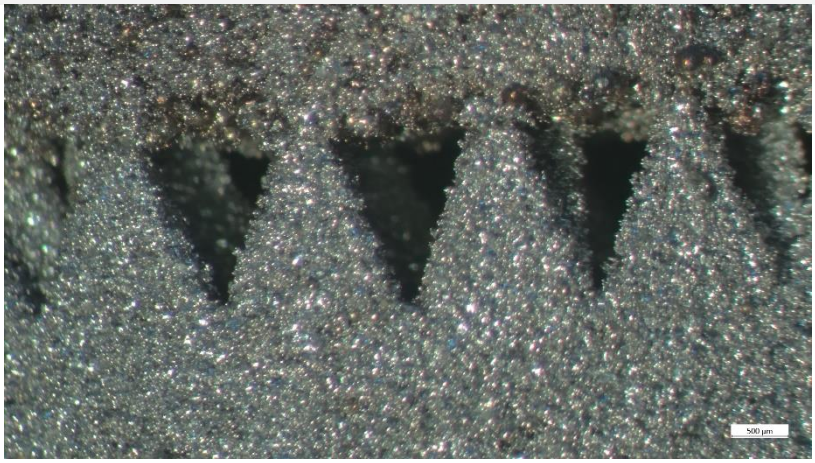

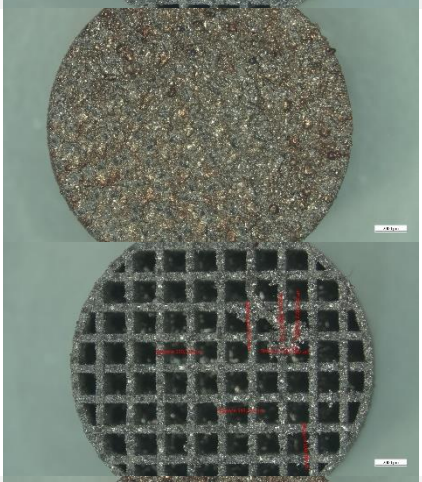

27

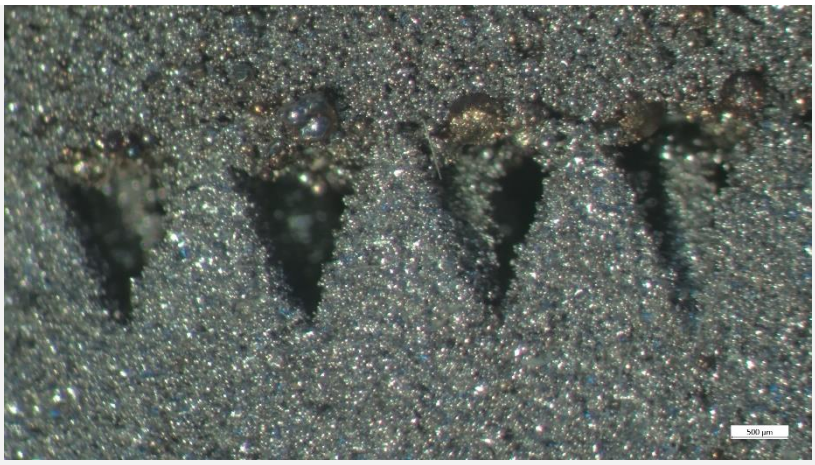

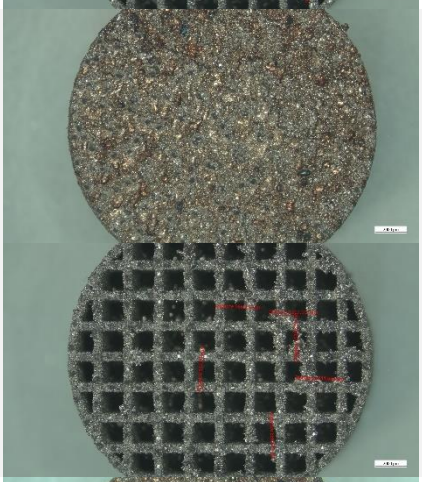

28

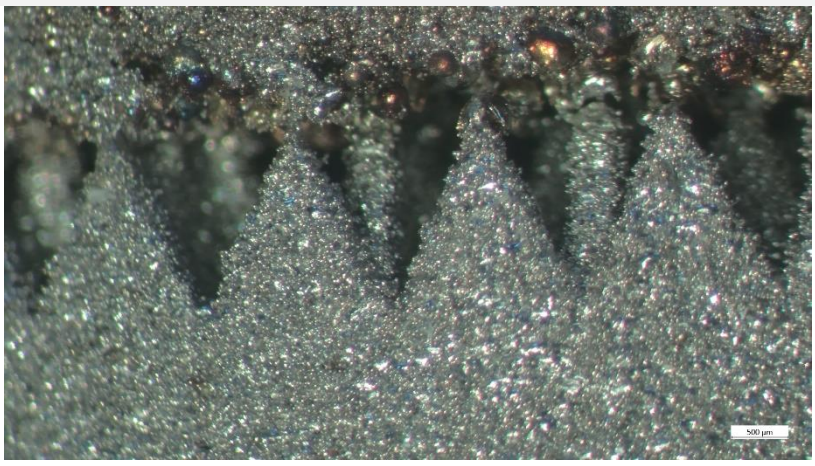

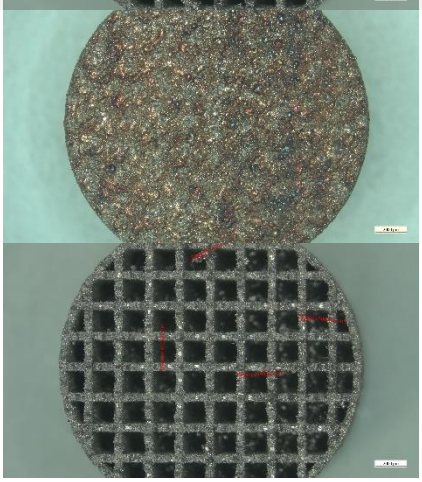

29

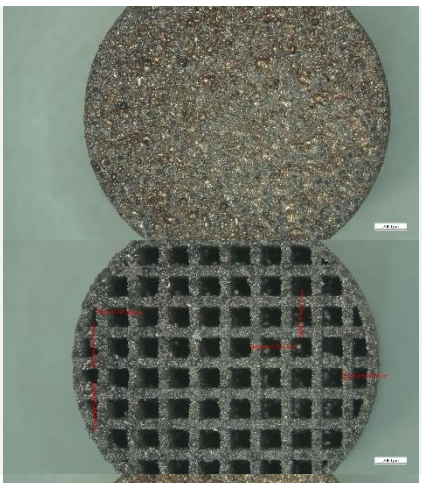

30

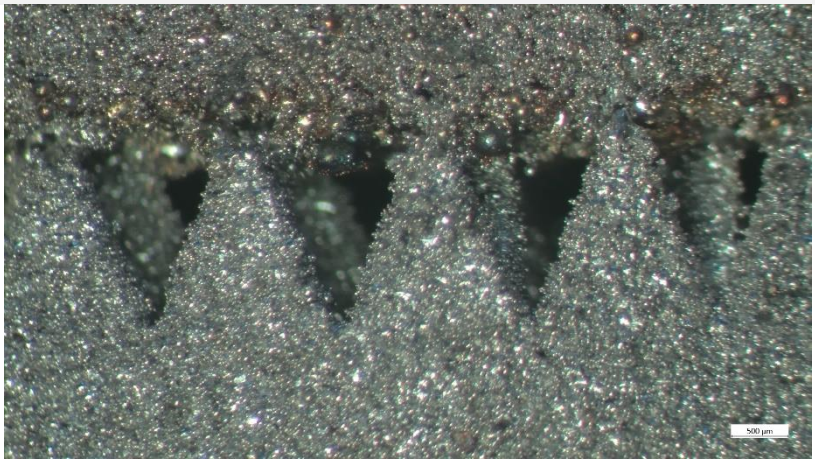

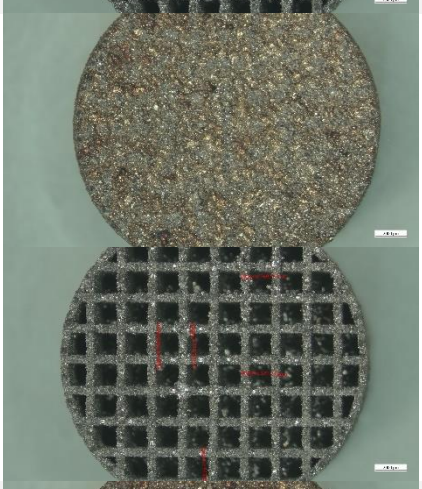

31

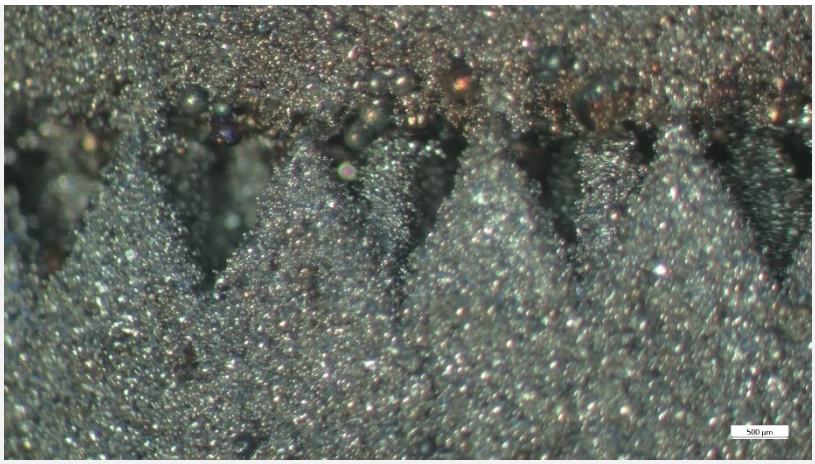

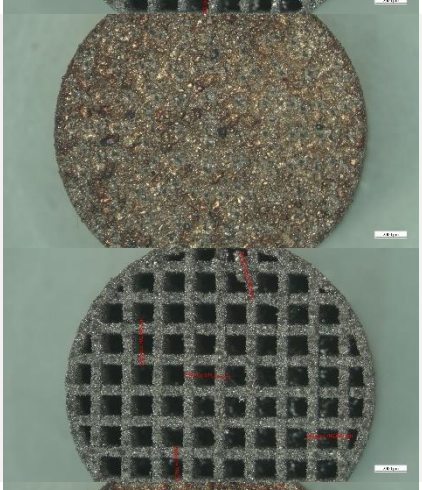

32

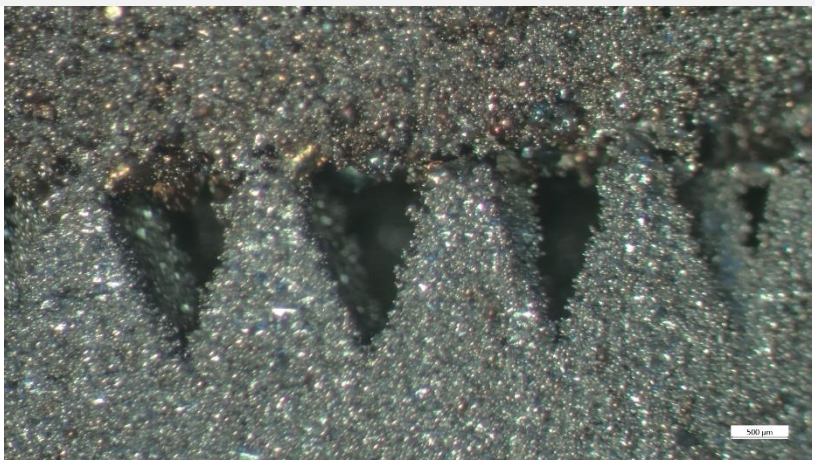

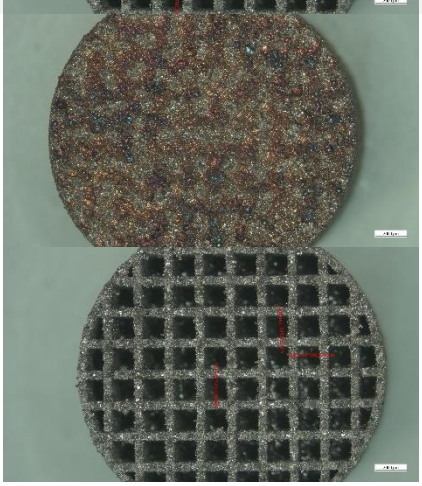

33

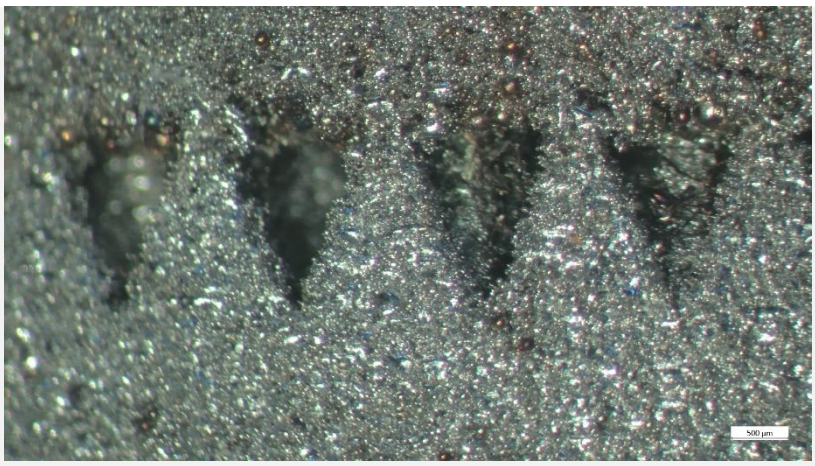

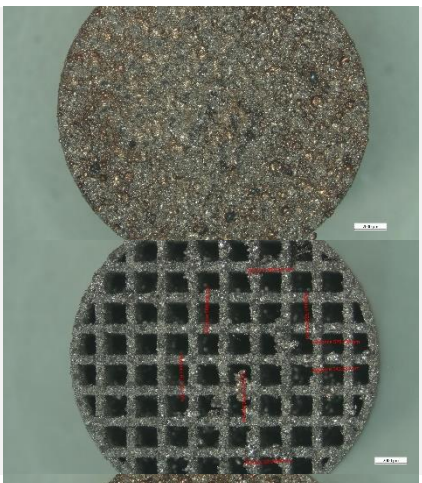

34

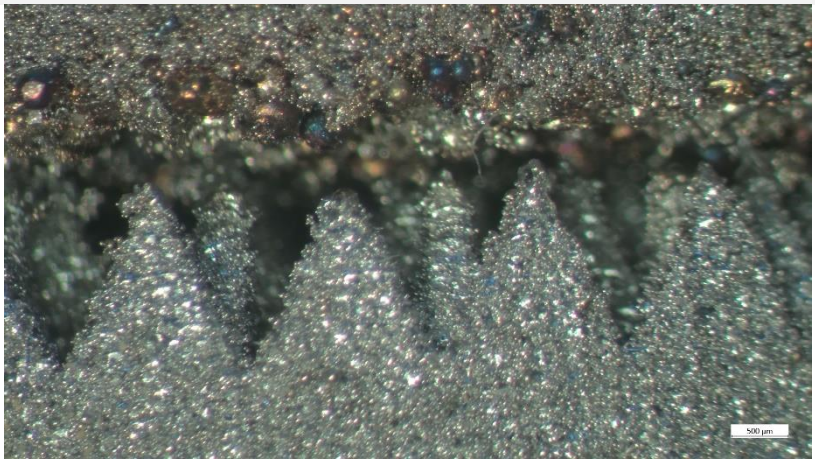

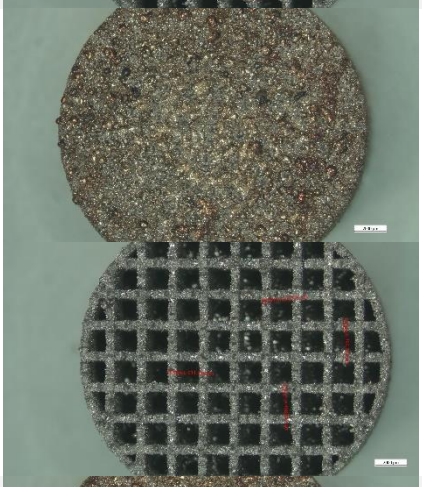

35

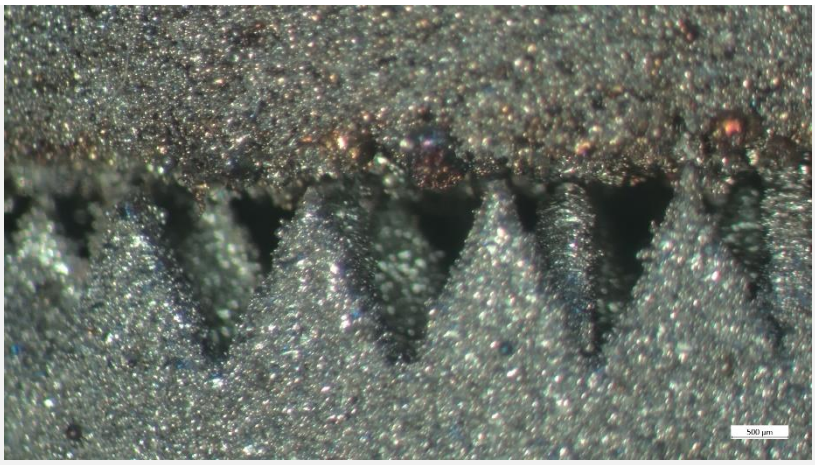

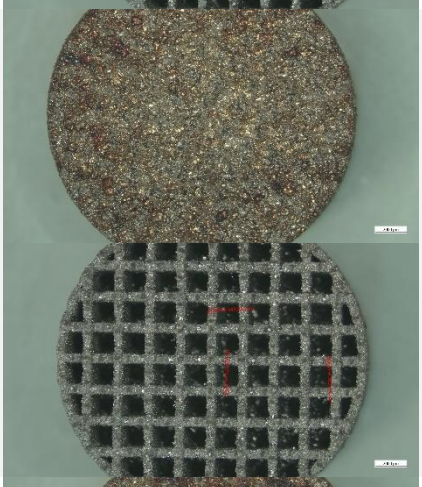

36